

Copyright

by

Omar Rene Espinoza

2007

**MEASUREMENTS OF DEFORMATIONS AND STRESSES DUE TO  
PLATE OUT-OF-FLATNESS IN A STEEL TWIN BOX GIRDER  
BRIDGE SYSTEM**

**by**

**OMAR RENE ESPINOZA, B.S.C.E.**

**THESIS**

Presented to the Faculty of the Graduate School of

The University of Texas at Austin

in Partial Fulfillment

of the Requirements

for the Degree of

**MASTER OF SCIENCE IN ENGINEERING**

**THE UNIVERSITY OF TEXAS AT AUSTIN**

**MAY 2007**

**MEASUREMENTS OF DEFORMATIONS AND STRESSES DUE TO  
PLATE OUT-OF-FLATNESS IN A STEEL TWIN BOX GIRDER  
BRIDGE SYSTEM**

**Approved by  
Supervising Committee:**

---

**Todd Helwig**

---

**Karl Frank**

## **Dedication**

I would like to dedicate this thesis to my family, whose love, support, attitude and perseverance made me the individual I am today.

## **Acknowledgements**

I would like to express my appreciation and thanks to Dr. Todd Helwig for all his guidance, support, advice, understanding, and friendship throughout this project. I would also like to thank Dr. Karl Frank for his guidance and support on the project. None of this would have been possible without their insight and collaboration.

I want to thank the technical staff and my colleagues at the Ferguson Structural Engineering Laboratory. Much of the success in the field is due to my fellow graduate students, as well as the Structural Engineering Department graduate students attending The University of Houston that provided assistance in many ways.

I would like to express a very special appreciation and thank you to Mr. Ken Stevens of Campbell Scientific, Inc. for the many hours of assistance. The numerous emails and phone calls were exceedingly welcomed and appreciated.

The research and writing of this thesis were made possible by funding from the Texas Department of Transportation, and I gratefully acknowledge them.

Thank you to God for giving me the strength and wisdom to complete this endeavor. Finally, I would like to thank my mother and father, and my brother, for all their support and friendship throughout my studies and my entire life. And most importantly, to my girlfriend, Ashleigh, for all her patience and understanding these past 2 years, I thank you.

## **Abstract**

# **MEASUREMENTS OF DEFORMATIONS AND STRESSES DUE TO PLATE OUT-OF-FLATNESS IN A STEEL TWIN BOX GIRDER BRIDGE SYSTEM**

Omar Rene Espinoza, M.S.E.

The University of Texas at Austin, 2007

Supervisor: Todd Helwig

Trapezoidal box girders are frequently used in curved bridge interchanges due to advantages in aesthetics, maintenance, and structural performance compared to comparable I-shaped girders. The smooth shape provides an aesthetic system and also results in fewer regions where corrosion causing agents such as moisture and debris collect thereby leading to decreased maintenance issues. The improved structural performance is due to the closed cross section that results in a large torsional stiffness which is important in curved bridge applications. Although there are several advantages to box girder system, the background and knowledge of the behavior of these systems is generally less than that of standard I-girders. One of the key elements of current studies, as well as the nature of this thesis, is the behavior of the slender plate elements that make

up the box girder cross-section. Because of their wide and slender nature, the plate elements are susceptible to local instabilities. In addition, the formulation of excessive plate deformations due to construction processes, as well as loading, can have detrimental effects on the structural behavior of the plate elements. The objective of the research documented in this thesis is to document the impact of plate imperfections on the behavior of steel bridge box girders. Measurements of the stresses and deformations in the plate elements of a twin box girder bridge constructed at Ferguson Structural Engineering Laboratory were carried out during construction and subsequent simulated live loading. Stress patterns are compared with imperfection measurements to document the impact on the girder behavior. This study is part of a larger project sponsored by the Texas Department of Transportation regarding plate tolerances. The measurements from this study will be used to validate finite element modeling techniques for studies on the impact of plate imperfections on the girder behavior. Data presented in this thesis will be combined with field measurements and computational results to help establish fabrication tolerances for plate out-of-flatness in steel bridge girders.

## Table of Contents

List of Tables .....	xi
List of Figures .....	xii
CHAPTER 1 Introduction.....	1
1.1 Overview.....	1
1.2 Issues and Objectives.....	5
1.3 Scope.....	7
CHAPTER 2 Background Studies.....	9
2.1 Introduction.....	9
2.2 Local Stabilities of Steel Plates.....	10
2.2.1 Plate Buckling.....	11
2.2.2 Post-Buckling Behavior.....	15
2.3 Geometric Plate Imperfections .....	19
2.4 Tolerances .....	22
2.4.1 American Specifications .....	23
2.4.2 International Specifications .....	31
CHAPTER 3 Field Measuring Instrumentation and Techniques .....	35
3.1 Introduction.....	35
3.2 Instrumented Bridge.....	35
3.3 Data Acquisition System.....	38
3.3.1 CR5000 Datalogger .....	38
3.3.2 AM416 Relay Multiplexer.....	40
3.4 Sensor Measuring Devices.....	41
3.4.1 Resistive Strain Measurement Devices.....	42
3.4.2 Temperature Measurement Devices .....	49
3.4.3 Combined Measurement Devices .....	52
3.5 Sensor Locations on the Bridge .....	56



3.6	Datalogger Programming.....	62
3.7	Linear Potentiometer Displacement Gage .....	62
CHAPTER 4	Girder Stresses during Construction and Live Loading .....	69
4.1	Introduction.....	69
4.2	Steel Trapezoidal Box Girders.....	69
4.2.1	Stress Changes due to Concrete Deck Construction.....	70
4.2.2	Stress Changes due to Live Load Testing.....	85
4.3	Finite Element Analysis Comparison .....	105
CHAPTER 5	Measurements of Plate Imperfections and Deformations.....	117
5.1	Introduction.....	117
5.2	Deformation of Plate Elements.....	117
5.3	Plate Tolerances and Public Opinion.....	126
CHAPTER 6	Conclusions.....	134
6.1	Overview.....	134
6.2	Summary of Results.....	135
6.2.1	Stress Distributions and Changes.....	136
6.2.2	Plate Deformations.....	138
6.3	Future Work.....	140
APPENDIX A	CR5000 Field Monitoring Program .....	141
A.1	Complete Program .....	141
APPENDIX B	Stress Distribution during Construction and Live Loading.....	148
B.1	Stress versus Time – Casting of Rails.....	148
B.2	Stress versus Time – Live Load Testing.....	152
APPENDIX C	Strain Corrections due to Thermal Effects .....	156
C.1	Correction Example .....	156

APPENDIX D Plate Deformations.....	160
References.....	175
Vita .....	179

## **List of Tables**

Table 3-1 Temperature Ranges for Types of Thermocouples (Watlow, 2007).....	50
Table 3-2 Type T Thermocouple Voltage-Temperature (ISE, 2007).....	52
Table 3-3 Data Acquisition System and Components .....	61
Table 3-4 Usable Lengths of Different Main Channel Sections.....	65
Table 4-1 Flat Steel Plate Experiment 1 .....	93
Table 4-2 Flat Steel Plate Experiment 2 .....	94
Table 4-3 Flat Steel Plate Experiment 3 .....	94
Table 5-1 Public-Eye Plate Tolerance Survey Results .....	133
Table C-1 Example Given Data.....	156
Table C-2 Example Calculations .....	157

## List of Figures

Figure 1-1 Koblenz Bridge Failure 1971 (Grzebieta, 2007).....	2
Figure 1-2 Typical Cross-Section of Box Girder Bridge.....	3
Figure 1-3 Internal Bracing System.....	4
Figure 2-1 Typical Built-Up Plate Sections.....	9
Figure 2-2 Simply Supported Compressed Plate.....	11
Figure 2-3 Plate Aspect Ratios vs. Buckling Coefficients (Allen, 1980).....	14
Figure 2-4 Coefficients for Various Boundary Conditions (Galambos, 1988).....	15
Figure 2-5 Post-Buckled Stress Distribution (Allen, 1980).....	16
Figure 2-6 Effective Width Concept (Galambos, 1988).....	17
Figure 2-7 Effective Width Stress Distribution (Allen, 1980).....	18
Figure 2-8 Out-of-Plane Deviations (Korol & Thimmhardy, 1987).....	19
Figure 2-9 Deflection of Plates with Initial Deviation (Allen, 1980).....	21
Figure 2-10 Permitted Tolerances for Carbon Steel Plates (ASTM A6, 2006).....	25
Figure 2-11 Possible ASTM Measurement Variations.....	26
Figure 2-12 Common Method of Measuring ASTM Out-of-Flatness.....	26
Figure 2-13 Tolerances for I-Girder Webs (Bridge Welding Code, 2002).....	27
Figure 2-14 Girder-Web Dimensions (Bridge Welding Code, 2002).....	27
Figure 2-15 Imperfection Measuring Method Variance (Mercan, 2005).....	29
Figure 2-16 Flatness of Panels Specification (AASHTO Hwy Bridge, 2002).....	30
Figure 2-17 Typical Imperfection Measurement (Korol & Thimmhardy, 1987).....	32
Figure 2-18 Plate Tolerances in European Specifications (Mercan, 2005).....	32
Figure 2-19 Panel Imperfection Details (Eurocode 3, 2003).....	33

Figure 3-1 Bridge Location at Ferguson Laboratory (Microsoft, 2007).....	36
Figure 3-2 Cross-Section of Box Girder Bridge.....	37
Figure 3-3 Plan View of Instrumented Bridge.....	37
Figure 3-4 Data Acquisition System Components.....	38
Figure 3-5 Multiplexer Scenarios .....	41
Figure 3-6 Resistive Strain Gages.....	42
Figure 3-7 Wheatstone Bridge Circuit (National, 2007) .....	44
Figure 3-8 Strain Gage in Full Bridge (Campbell, 1996).....	47
Figure 3-9 Thermocouples.....	49
Figure 3-10 Geokon Model 4000 Vibrating Wire Strain Gage .....	53
Figure 3-11 Vibrating Wire Strain Gage Schematic (Geokon, 2005) .....	54
Figure 3-12 AVW1 Vibrating Wire Interface.....	55
Figure 3-13 Section Locations for Instrumentation.....	57
Figure 3-14 Section A Foil and Rosette Locations.....	58
Figure 3-15 Section A Thermocouple Locations.....	58
Figure 3-16 Section A Vibrating Wire Strain Gage Locations.....	59
Figure 3-17 Section B Rosette Strain Gage Locations .....	60
Figure 3-18 End Caps .....	64
Figure 3-19 Linear Potentiometer Displacement Gage (Mercan, 2005).....	64
Figure 3-20 Locations of Web Imperfection Measurements .....	66
Figure 3-21 Measuring Web Imperfections (Mercan, 2005).....	67
Figure 3-22 Measuring Bottom Flange Imperfections (Mercan, 2005).....	68
Figure 4-1 Strain Gage Locations and Labels.....	71

Figure 4-2 Stress Changes due to Casting of Deck (ksi) Section A .....	72
Figure 4-3 Validation of Foil Strain Gages (Arakan, 2005) .....	73
Figure 4-4 Average Stress Changes due to Casting of Deck (ksi) Section A.....	74
Figure 4-5 Stress Development during Deck Casting – Top of Web .....	76
Figure 4-6 Stress Development during Deck Casting – Mid-Height of Web.....	76
Figure 4-7 Stress Development during Deck Casting – Bottom of Web.....	77
Figure 4-8 Stress Changes due to Casting of Deck (ksi) Section B.....	77
Figure 4-9 Average Stress Changes due to Casting of Deck (ksi) Section B.....	79
Figure 4-10 Stress Changes due to West Rail (ksi) Section A .....	79
Figure 4-11 Average Stress Changes due to West Rail (ksi) Section A.....	81
Figure 4-12 Stress Changes due to West Rail (ksi) Section B.....	81
Figure 4-13 Average Stress Changes due to West Rail (ksi) Section B .....	82
Figure 4-14 Stress Changes due to East Rail (ksi) Section A.....	83
Figure 4-15 Average Stress Changes due to East Rail (ksi) Section A .....	83
Figure 4-16 Stress Changes due to East Rail (ksi) Section B.....	84
Figure 4-17 Average Stress Changes due to East Rail (ksi) Section B .....	85
Figure 4-18 Live Load Simulation - Front Axle.....	86
Figure 4-19 Live Load Simulation - Rear Axle .....	87
Figure 4-20 Live Load Simulation - Full View .....	87
Figure 4-21 Live Load Position 1 .....	88
Figure 4-22 Live Load Position 2 .....	89
Figure 4-23 Live Load Position 3 .....	89
Figure 4-24 Steel Plate Experiment Scenario .....	92

Figure 4-25 Stress Changes due to Live Load Position 1 (ksi) Section A.....	95
Figure 4-26 Avg. Stress Changes due to Live Load Position 1 (ksi) Sect. A.....	95
Figure 4-27 Stress Changes due to Live Load Position 1 (ksi) Section B.....	96
Figure 4-28 Avg. Stress Changes due to Live Load Position 1 (ksi) Sect. B.....	96
Figure 4-29 Stress Development of Live Load Position 1 – Top of Web .....	97
Figure 4-30 Stress Changes due to Live Load Position 2 (ksi) Section A.....	98
Figure 4-31 Avg. Stress Changes due to Live Load Position 2 (ksi) Sect. A.....	99
Figure 4-32 Stress Development of Live Load Position 2 – Top of Web .....	100
Figure 4-33 Stress Changes due to Live Load Position 2 (ksi) Section B.....	101
Figure 4-34 Avg. Stress Changes due to Live Load Position 2 (ksi) Sect. B.....	101
Figure 4-35 Stress Changes due to Live Load Position 3 (ksi) Section A.....	102
Figure 4-36 Avg. Stress Changes due to Live Load Position 3 (ksi) Sect. A.....	103
Figure 4-37 Stress Development of Live Load Position 3 – Top of Web .....	104
Figure 4-38 Stress Changes due to Live Load Position 3 (ksi) Section B.....	104
Figure 4-39 Avg. Stress Changes due to Live Load Position 3 (ksi) Sect. B.....	105
Figure 4-40 FEA Steel Box Girders Model .....	106
Figure 4-41 Field & FEA Results for Construction of Deck (ksi) Section A.....	107
Figure 4-42 Field & FEA Results for Construction of Deck (ksi) Section B.....	108
Figure 4-43 Field & FEA Results for West Rail (ksi) Section A .....	108
Figure 4-44 Field & FEA Results for West Rail (ksi) Section B.....	108
Figure 4-45 Field & FEA Results for East Rail (ksi) Section A.....	109
Figure 4-46 Field & FEA Results for East Rail (ksi) Section B.....	109
Figure 4-47 Stress Distribution due to Deck – Inner Web of Interior Girder.....	110

Figure 4-48 FEA Live Load Testing Model .....	111
Figure 4-49 FEA Live Load Testing Model with Applied Loads .....	112
Figure 4-50 Field & FEA Results for Live Load Position 1 (ksi) Section A.....	113
Figure 4-51 Field & FEA Results for Live Load Position 1 (ksi) Section B.....	113
Figure 4-52 Field & FEA Results for Live Load Position 2 (ksi) Section A.....	114
Figure 4-53 Field & FEA Results for Live Load Position 2 (ksi) Section B.....	114
Figure 4-54 Field & FEA Results for Live Load Position 3 (ksi) Section A.....	114
Figure 4-55 Field & FEA Results for Live Load Position 3 (ksi) Section B.....	115
Figure 4-56 Stress Distribution of Live Load Position 1 - Outer Web of Interior Girder .....	116
Figure 5-1 Ext. Girder Web Initial Imperfections .....	118
Figure 5-2 Ext. Girder Web Deformations due to Deck Casting.....	119
Figure 5-3 Ext. Girder Web Deformations due to Bracket Removal .....	119
Figure 5-4 Int. Girder Web Initial Imperfections.....	120
Figure 5-5 Int. Girder Web Deformations due to Deck Casting.....	121
Figure 5-6 Int. Girder Web Deformations due to Bracket Removal.....	121
Figure 5-7 Ext. Girder Bottom Flange Initial Imperfections .....	123
Figure 5-8 Ext. Girder Bottom Flange Deformations due to Casting of Deck....	124
Figure 5-9 Int. Girder Bottom Flange Initial Imperfections .....	125
Figure 5-10 Int. Girder Bottom Flange Deformations due to Casting of Deck ...	125
Figure 5-11 Dimensions and Plate Imperfections of Plate Elements .....	127
Figure 5-12 Maximum Bottom Flange Imperfections .....	128
Figure 5-13 Maximum Exterior Web Imperfections .....	130
Figure 5-14 Maximum Interior Web Imperfections .....	131



Figure B-1 Stress Development of West Rail Casting – Top of Web .....	149
Figure B-2 Stress Development of West Rail Casting – Middle of Web .....	149
Figure B-3 Stress Development of West Rail Casting – Bottom of Web.....	150
Figure B-4 Stress Development of East Rail Casting – Top of Web.....	150
Figure B-5 Stress Development of East Rail Casting – Middle of Web .....	151
Figure B-6 Stress Development of East Rail Casting - Bottom of Web.....	151
Figure B-7 Stress Development of Live Load Position 1 – Middle of Web.....	152
Figure B-8 Stress Development of Live Load Position 1 – Bottom of Web .....	153
Figure B-9 Stress Development of Live Load Position 2 – Middle of Web.....	153
Figure B-10 Stress Development of Live Load Position 2 – Bottom of Web .....	154
Figure B-11 Stress Development of Live Load Position 3 - Middle of Web .....	154
Figure B-12 Stress Development of Live Load Position 3 - Bottom of Web.....	155
Figure C-1 Temperature versus Time .....	158
Figure D-1 Exterior Girder Outer Web - Initial Imperfections.....	161
Figure D-2 Exterior Girder Outer Web - After Casting of Deck.....	162
Figure D-3 Exterior Girder Outer Web - After Bracket Removal .....	163
Figure D-4 Exterior Girder Inner Web - Initial Imperfections .....	164
Figure D-5 Exterior Girder Inner Web - After Casting of Deck.....	165
Figure D-6 Interior Girder Outer Web - Initial Imperfections.....	166
Figure D-7 Interior Girder Outer Web - After Casting of Deck.....	167
Figure D-8 Interior Girder Outer Web - After Bracket Removal .....	168
Figure D-9 Interior Girder Inner Web - Initial Imperfections .....	169
Figure D-10 Interior Girder Inner Web - After Casting of Deck.....	170

Figure D-11 Interior Girder Bottom Flange - Initial Imperfections .....	171
Figure D-12 Interior Girder Bottom Flange - After Casting of Deck.....	172
Figure D-13 Exterior Girder Bottom Flange - Initial Imperfections .....	173
Figure D-14 Exterior Girder Bottom Flange - After Casting of Deck.....	174

# **CHAPTER 1**

## **Introduction**

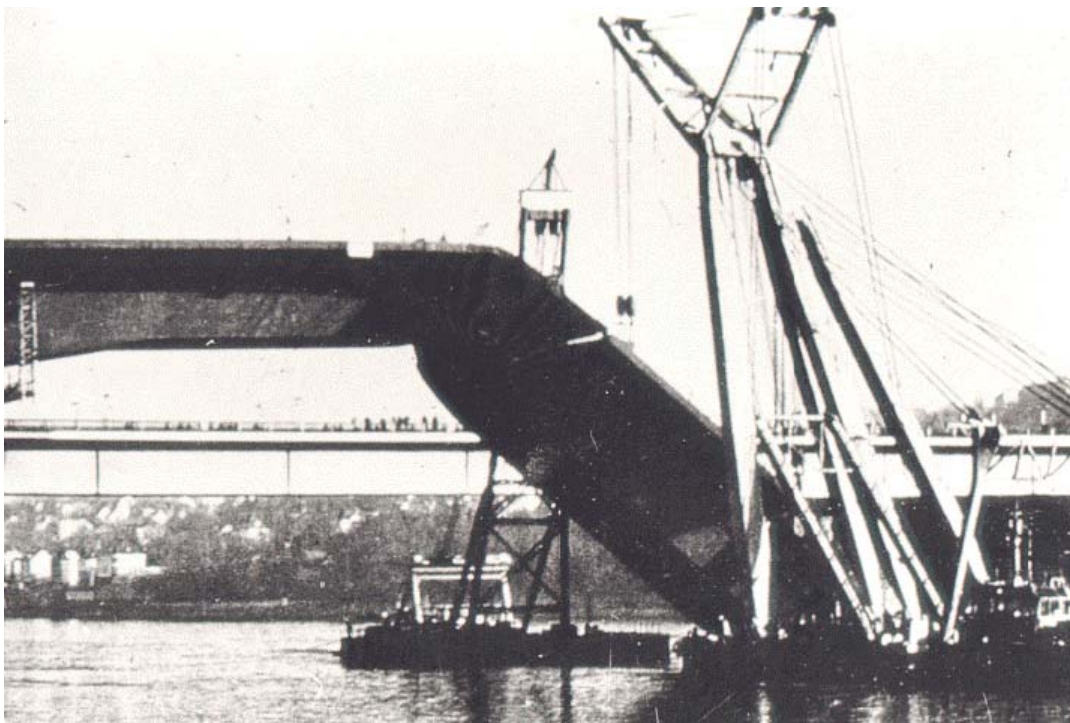
### **1.1 Overview**

The use of trapezoidal box girders in the state of Texas has significantly increased since the late 1980's. While there are a number of reasons for the appeal of the box girders, the three primary reasons are the aesthetical appeal, easy maintenance, and structural capabilities. Over the past decade, aesthetics has become an important factor in bridge design in the United States. The sleek closed box girder cross-sections provide a slender appearance and the steel box shape match the concrete U-beams that are often utilized on the approach spans to the steel girders. In addition, simplicity is visible since many bracing members and stiffeners are hidden inside the box girders.

The smooth contour of the box girders also provides maintenance advantages since there are not regions where corrosion agents such as moisture and debris. The inside of the box typical is protected from the elements and remains dry, reducing any corrosion problems.

Although box girders are sometimes used in straight girder systems, the primary application of the girders are on horizontally curved girders where the large torsional stiffness makes them an ideal structural form. Due to the nature of the closed box geometry, the system has a significantly high torsional stiffness. This leads to better load distribution throughout the system and can also produce more efficient designs. Because of these reasons, the number of box girders needed to support the bridge system is typically less than with standard I-girders.

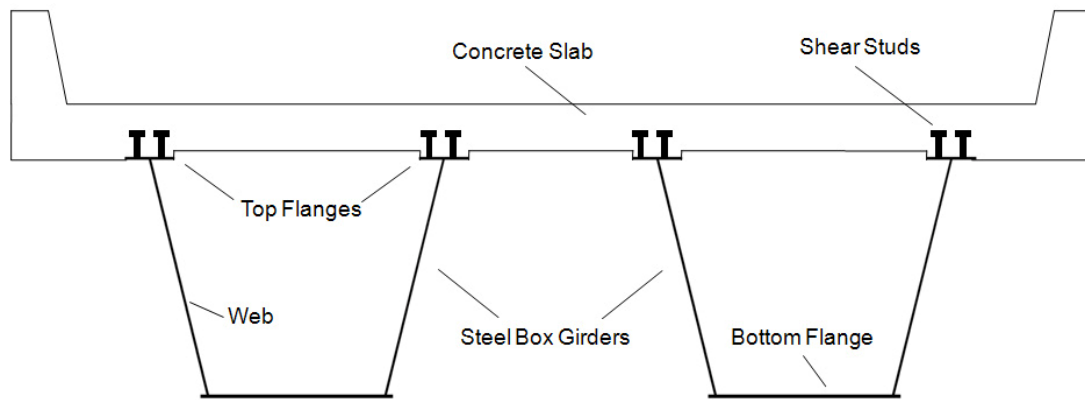
Although box girders have many aesthetic and structural advantages, the relatively wide plate elements in the cross-sections can lead to local instabilities that could influence the systems overall strength. Some box girder bridge failures in the 1970's have emphasized the importance of considering local buckling in the design process. Figure 2-1 shows the failure of the Koblenz Bridge that crossed over the Rhine in Germany in November of 1971.



**Figure 1-1 Koblenz Bridge Failure 1971 (Grzebieta, 2007)**

Single-cell composite box girder bridge systems usually consist of multiple girders. The girders have been successfully utilized in several flyover ramp interchanges between major highways that have typically consisted of two- and three-girder systems. The girders are typically trapezoidal shaped with two top flanges, two webs, and a single bottom flange. Shear studs attached to the top flanges provide the composite action with

the cast-in-place concrete deck. Figure 1-2 shows a typical cross-section of the box girder bridge system.



**Figure 1-2 Typical Cross-Section of Box Girder Bridge**

As previously stated, box girder bridges are known for their superior torsional stiffness. However, this stiffness is only achieved once the concrete deck is in place and gains sufficient strength. During transportation, erection, and construction, the girder is an open section with low stiffness due to its relatively thin elements. To help increase the overall stiffness of the girders themselves during these crucial events, internal bracing systems are often installed. Figure 1-3 presents some of the typical bracing systems, which include braces both internal and external to the boxes. The internal bracing system consists of vertical cross-frames that are evenly spaced along the length of the girders as well as a top flange lateral truss that consists of both diagonals and struts. The internal K-frames are typically positioned at a panel point of the top flange lateral truss so that the strut of the internal K-frame is also a strut in the top flange lateral truss. The main purpose of the top flange truss bracing system is to help increase the torsional stiffness of the system during erection and construction. In addition to the internal braces, box

girders also often have external braces that frame between adjacent girders. These braces may consist of solid plate diaphragms that are used at the supports of the girders or may also consist of external K-frames at intermediate locations along the length of the bridge. The solid plate diaphragms stay on the bridge throughout the service life, while intermediate K-frames are often removed after construction to avoid potential fatigue problems that might occur in the vicinity of the braces. While severity of the potential fatigue problems from the external braces have not been documented, the braces are removed based upon past problems that have occurred in I-girder systems – particularly those with heavily skewed supports.



**Figure 1-3 Internal Bracing System**

## 1.2 Issues and Objectives

Through the end of the 1960's, there was no detailed specification or code regarding the design of box girders in any country throughout the world. At the time it was generally adopted to simply use a factor of safety on the buckling stress, however, these safety factors varied from country to country. As stated in the previous section, some box girder bridge failures in the 1970's reinforced the need for improvements design rules. New design approaches were based on the ultimate strength of not only the girders themselves, but of their many components. In doing so, much attention was paid to the role of initial imperfections, both mechanical and geometrical, in regards to the girders overall strength (Galambos, 1988).

The plate elements in box girder bridges are susceptible to local instabilities in regions subjected to compressive stresses due to their wide and slender nature. Local buckling behavior is typically governed by the plate's width-to-thickness ratio, or slenderness ratio. The higher the slenderness ratio of a plate element, the more likely it is to buckle locally when exposed to load. Engineers and designers often control plate buckling by limiting the plate's deformations. Deformations in the plate elements are based on the plate's slenderness, as well as any imperfections the plate may have or experience.

Imperfections can generally be classified into one of two groups: mechanical or geometrical. Mechanical imperfections include residual stresses on the steel structures due to welding and fabrication processes. Geometrical imperfections are more related to the out-of-flatness or straightness of an element, and are the type of results provided in this thesis. Individual plate elements of which the girder cross-sections are comprised of are generally not flat to begin with, and must satisfy the American Society of Testing and Materials (ASTM) guidelines for plate stock. Imperfections arise and are increased when

plate elements are further subjected to fabrication, transportation, erection, and the various construction processes.

As previously noted, engineers try to limit the local buckling of plate members by limiting plate deformations. Steel fabricators have a difficult task of controlling the out-of-flatness of plate elements. However, methods of measuring and classifying these tolerances are not clear and in some instances, don't exist. Many specifications throughout the country (and the world) base their plate deformation tolerances on research performed individually for their specification. Thus, different specifications are based on a variety of results, all resulting in tolerance limits that vary from source to source. The lack of a constant derivation method and tolerance limit furthers the confusion fabricators, engineers, and inspectors experience when analyzing plate deformations.

The goal of this research study is to examine the impact of plate imperfections on the design and behavior of steel bridge box girders. Field studies have been performed to analyze stress distributions in the box girders during all phases of construction. Stress patterns will be compared with imperfection measurements to examine if any correlation between the two is present.

The results presented in this thesis are part of a larger study on plate tolerances for steel girders. The study is sponsored by the Texas Department of Transportation (TxDOT) and includes field measurements, laboratory studies, and computational investigations. Current research projects at the University of Texas at Austin in conjunction with prior and current projects at the University of Houston will help establish the basis for the overall plate tolerance study. Data presented in this thesis will be included in the field measurements aspect of the overall project and will further be used to establish a range of typical plate imperfections found in fabricated steel girders.



With this knowledge, plate tolerances based upon the impact of structural behavior can be formulated and implemented into current specifications to help provide a more uniform code of practice.

### **1.3 Scope**

As outlined in the previous section, the results reported in this thesis are a component of a larger study on plate tolerances for steel girders. The study has included field measurements, laboratory tests and computational studies. Results are presented in this thesis from measurements from a twin box girder bridge constructed at the Ferguson Structural Engineering Laboratory at the University of Texas. The bridge was comprised of two steel trapezoidal box girders that were recently removed from service in Houston, Texas. Initially the primary use of the girders was to conduct measurements on the structural redundancy of the twin box girder bridge by fracturing one of the girders using a shape charge. However, the girders provided a wealth of data to several research projects. The material that is presented in this thesis focuses on data gathered during construction of the concrete bridge deck and rails, as well as subsequent live loading on the girders using a simulated design truck. The results will provide a basis of comparison for laboratory and computational studies that are being performed by other researchers on the overall project. The field results achieved will also play a vital role in stepping forward towards formulating plate tolerances for guidelines and specifications.

Following this introductory chapter, background information on local instabilities on plate members is provided in Chapter 2. Chapter 2 provides an overview of geometric plate imperfections and tolerance values from various specifications throughout the world. Chapter 3 presents the field measuring instrumentation and techniques used.

Information regarding the bridge geometry as well as details regarding all sensor measuring devices, deformation monitoring instruments, and data acquisition systems are discussed. Chapter 4 presents the data that was gathered from the strains on the girder cross-section through the construction and live load process. Chapter 5 provides an overview of measured out-of-flatness of several of the web panels and bottom flanges of the box girders. In addition to the field measurements, finite element analysis results are presented and compared with field results in Chapters 4. Finally, the results of the thesis are summarized in Chapter 6 as well as a brief overview of recommendations for future work.

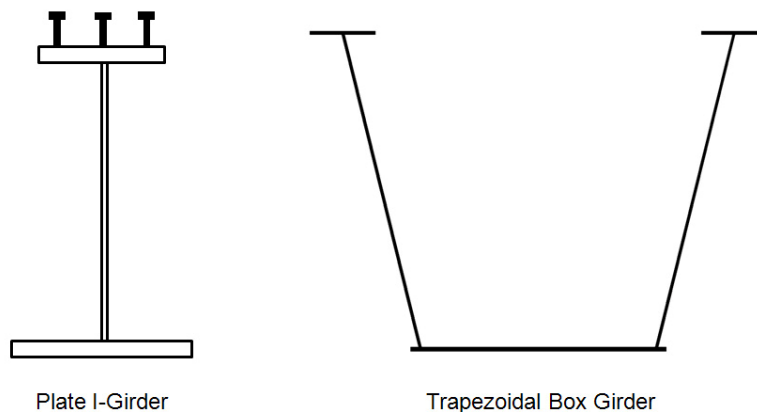
## CHAPTER 2

### Background Studies

#### 2.1 Introduction

Background information is presented in this chapter to provide the framework for the reader to understand the measurement procedures and data presented in later chapters. Summaries of previous investigations on plate buckling, imperfections, and tolerances are discussed in the proceeding sections of this chapter.

Typical steel sections in steel bridges may consist of either hot-rolled or built-up sections. Most standard hot-rolled sections are proportioned so that local instability problems are minimal. However, some projects require steel members larger than standard rolled shapes. While fabrication costs of built-up sections can be large, the sizes of the steel plates can be varied along the girder length in proportion to the force demand thereby minimizing the weight of the steel section. Figure 2-1 shows some typical built-up plate sections.



**Figure 2-1 Typical Built-Up Plate Sections**

Built-up sections are often used in bridge construction, where different loading patterns are present. Thus, the plate sections often experience shifts in stress distributions during construction stages and live loading occurrences. For economy, the webs and flanges of built-up plate members are often proportioned for the flexural, shear, and torsional demands along the girder length. While slender flanges are often avoided in these sections, relatively thin webs can often result. Although minimizing the plate thicknesses can have economical advantages, the thin plates are susceptible to local instabilities when from compressive forces. Plate instabilities can lead to both local and global buckling problems in the structure. Geometric distortions and structural imperfections are important factors regarded with plate sections due to their influence on local instabilities. Imperfections can come from several sources including the out-of-flatness that results during the rolling of plates. Additional imperfections can come during the fabrication processes, transportation, and erection, and these imperfections are liable to reduce strength capacities and increase local buckling instances (Segui, 2003).

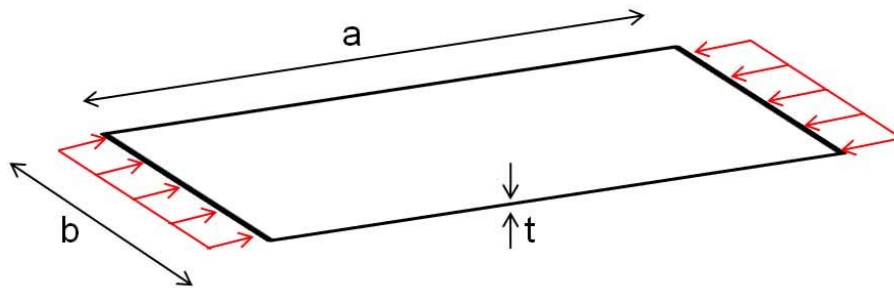
## **2.2 Local Stabilities of Steel Plates**

The terms local instability and local buckling can be used interchangeably to define out-of-plane deformations that occur in plates as a result of stresses that are compressive in nature. When a plate element is subjected to compressive stresses that may result from axial force, bending, shear, or any combination of these, the plate may reach a local instability. Depending on the slenderness of the plate, this local buckling can occur at stresses significantly below the yield stress of the member. Plate behavior has been a researched field that has evolved over time. The behavior of plates can be

categorized into pre- and post-buckling phases. The presence of initial out-of-flatness in plate elements and its effects will also be discussed.

### 2.2.1 Plate Buckling

Theories regarding plate bending in the eighteenth century neglected twisting restraint and therefore often resulted in estimated plate deformations that were too large. In 1820, Navier studied plate bending and formulated an expression that would later be improved by St. Venant. The basic assumptions of the plate bending theory were that deflections were small (less than the plate thickness), the middle plane of the plate does not stretch, plane sections rotated but did not distort, shear forces were neglected, and finally that the plate thickness was substantially smaller than any of the other plate dimensions (Allen, 1980). A plate of width  $b$ , length  $a$ , and thickness  $t$  under uniform compression is shown in Figure 2-2.



**Figure 2-2 Simply Supported Compressed Plate**

Equation (2.1) shows the linear theory of plate buckling.

$$\nabla^4 \omega = \frac{\partial^4 \omega}{\partial x^4} + 2 \frac{\partial^4 \omega}{\partial x^2 \partial y^2} + \frac{\partial^4 \omega}{\partial y^4} = \frac{q}{D} \quad (2.1)$$

The variable  $\omega$  is the plate deflection,  $q$  is the lateral load applied, and  $D$  is the flexural stiffness of the plate.  $D$  is a function of the modulus of elasticity,  $E$ , the plate thickness,  $t$ , and Poisson' ratio,  $\nu$  and is given in Equation (2.2).

$$D = \frac{E t^3}{12 (1 - \nu^2)} \quad (2.2)$$

It is possible that there are additional forces applied to the plate that act on the edges and can have a significant affect the overall plate bending. These additional forces, when implemented with Equation (2.1), produce the following expression:

$$\nabla^4 \omega = \frac{1}{D} \left( q + N_x \frac{\partial^2 \omega}{\partial x^2} + 2N_{xy} \frac{\partial^2 \omega}{\partial x \partial y} + N_y \frac{\partial^2 \omega}{\partial y^2} \right), \quad (2.3)$$

where,  $N_x$  and  $N_y$  are the orthogonal edge compressive forces per unit length, and  $N_{xy}$  and  $N_{yx}$  are the edge shearing forces.

In 1891, G.H. Bryan modified the general differential equation. Only one edge compression load was applied in the longitudinal direction. Assuming the flat plate buckles at a certain critical load, a buckling stress equation was formulated (Galambos, 1988). In Equation (2.4),  $k$  represents a plate buckling coefficient that is dependent on several parameters that are discussed later in the chapter.

$$\sigma_{cr} = \frac{N_{cr}}{t} = \frac{k\pi^2 D}{tb^2} = \frac{k\pi^2 E}{12(1 - \nu^2) \left(\frac{b}{t}\right)^2} \quad (2.4)$$

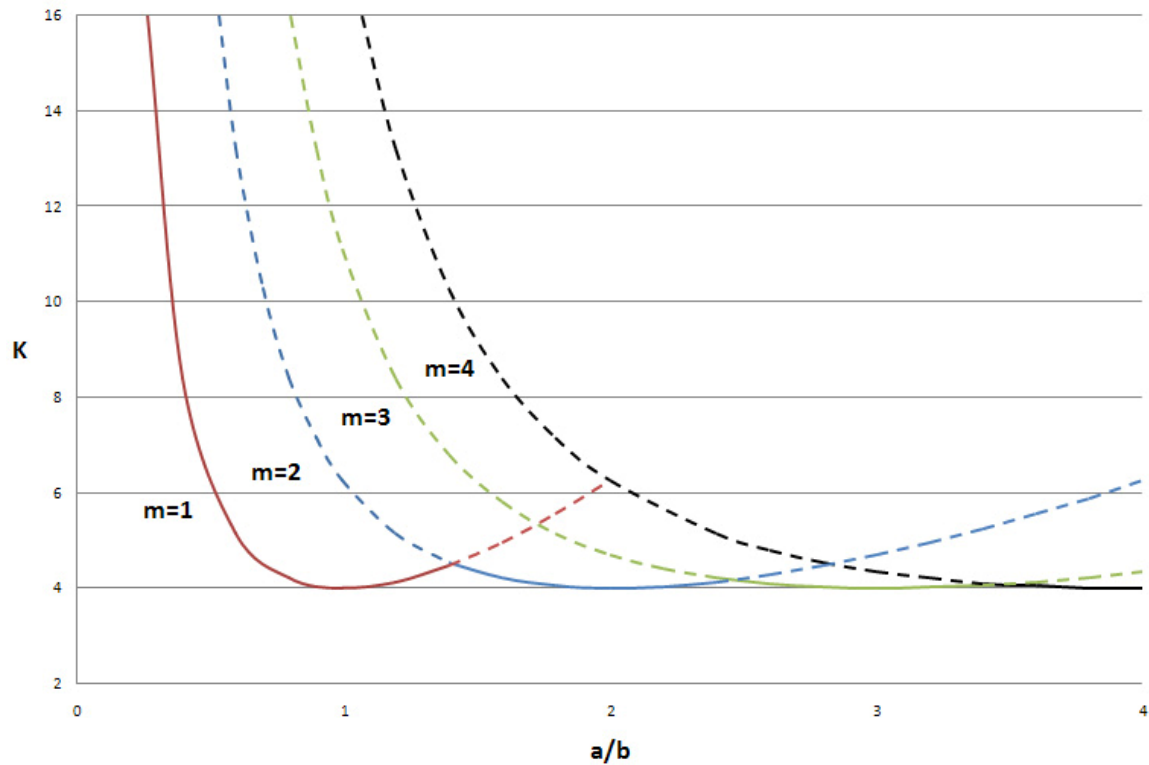
The buckling coefficient is a function of the geometry and boundary conditions of the plate. For a long simply supported plate subjected to uniform compression, the buckling coefficient is as follows,

$$k = \left( \frac{m}{\gamma} + \frac{n^2 \gamma}{m} \right)^2. \quad (2.5)$$

In Equation (2.5),  $\gamma$  is the aspect ratio of the plate ( $a/b$ ),  $m$  is the number of half buckling waves in the direction of the compressive load, and  $n$  is the number of waves in the transverse direction (Maquoi, 1995). The value of  $n$  is often taken as 1 making which assumes that the plate buckles in a single half wave in the transverse direction. Therefore Equation 2.5 reduces to the following:

$$k = \left( \frac{m}{\frac{a}{b}} + \frac{\frac{a}{b}}{m} \right)^2 \quad (2.6)$$

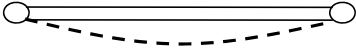

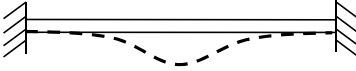
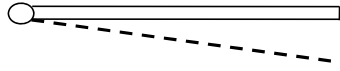
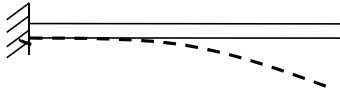
The buckling mode of the plate changes as the aspect ratio increases. Figure 2-3 shows a graph relating the number of waves in a buckled shape ( $m$ ), aspect ratios ( $a/b$ ), and the buckling coefficients ( $k$ ).



**Figure 2-3 Plate Aspect Ratios vs. Buckling Coefficients (Allen, 1980)**

Values of  $m = 1$  through  $m = 4$  are plotted and for each value of  $m$ , there is a non-linear relationship between  $k$  and  $a/b$ . As shown on the graph minimum values of  $k$  can be found when  $m = a/b$ . Equation (2.5) and (2.6) are for plates that are simply supported along the edges. As the boundary conditions change, the buckled shapes change which leads to different buckling coefficients. A diagram showing various boundary conditions and their corresponding buckling coefficients is shown in Figure 2-4.



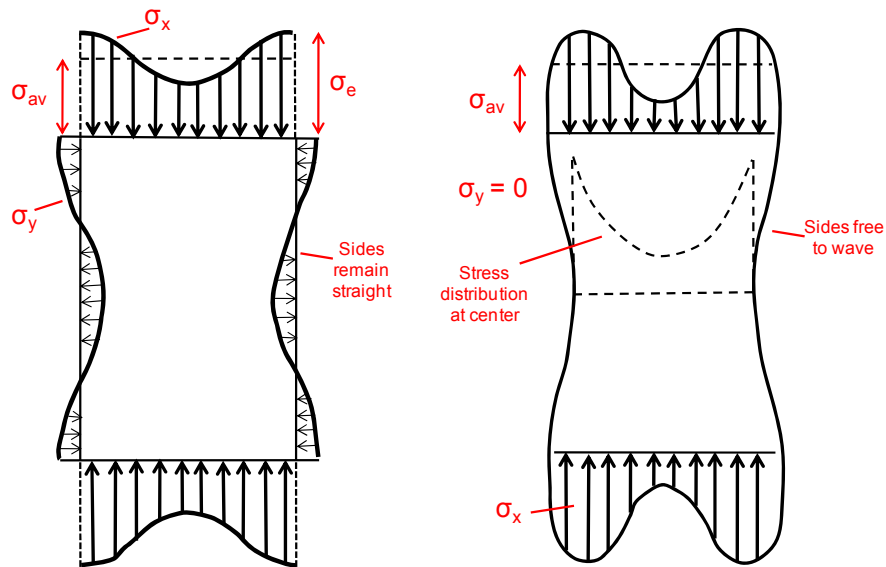
<u>Edge Support</u>	<u>k</u>	
Both edges simply supported	4.00	
One edge simply supported, one fixed	5.42	
Both edges fixed	6.97	
One edge simply supported, one free	0.425	
One edge fixed, one free	1.277	

**Figure 2-4 Coefficients for Various Boundary Conditions (Galambos, 1988)**

### 2.2.2 Post-Buckling Behavior

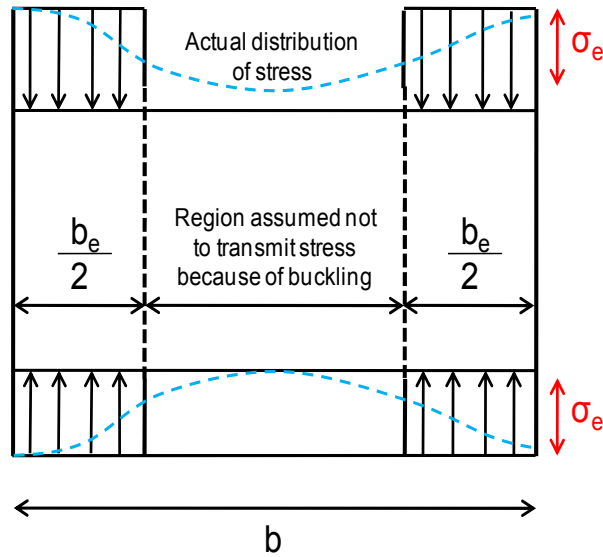
Although the load carrying capacity of members such as columns drop off after buckling, the ultimate strength of plates can be much greater than their critical buckling load strengths. The higher ultimate strength of plates generally comes from post-buckling strength primarily due to stress redistribution. For example, before local buckling may occur in a plate, the distribution of the edge compression may be uniform. When the plate buckles locally, stiffness is lost and the stresses can be redistributed, resulting in a non-uniform distribution of stresses. The stresses that are redistributed cause the middle surface of the plate to stretch. In pre-buckling plate theory (small

deflection theory), the assumption is made that the middle surface does not stretch, however, this assumption is unrealistic. In post-buckling plate theory (large deflection theory), the middle surface is allowed to stretch. The distribution pattern of stress after being redistributed is governed by the constraints along the unloaded edges of the plate. Figure 2-5 shows stress distributions due to different constraints. In the first case, the longitudinal edges are held straight but are allowed to move laterally. The second case shows the longitudinal edges not held straight and allowed to move laterally transversely (Allen, 1980).



**Figure 2-5 Post-Buckled Stress Distribution (Allen, 1980)**

The maximum strengths of plates can be derived using the “effective width” concept. The effective width concept suggests that most of the load applied is carried along the edge of the plate. The edges act as thin strips over which the load is uniformly applied, allowing the middle region of the plate to remain unstressed. Figure 2-6 shows the effective width concept.



**Figure 2-6 Effective Width Concept (Galambos, 1988)**

Von Karman was one of the first to study the effective width concept in relation to thin plate bending. He derived an approximate formula for the effective width of simply supported plates. The plates were exposed to uniform compression and stiffened along the edges parallel to the loading. The formula derived assumed the two strips carried the entire load and is shown in Equation (2.7).

$$b_e = \left[ \frac{\pi}{\sqrt{3(1-\nu^2)}} \sqrt{\frac{E}{\sigma_e}} \right] t \quad (2.7)$$

Combing Equation (2.4) with (2.7) yields Equation (2.8),

$$\frac{b_e}{b} = \sqrt{\frac{\sigma_{cr}}{\sigma_e}} \quad (2.8)$$

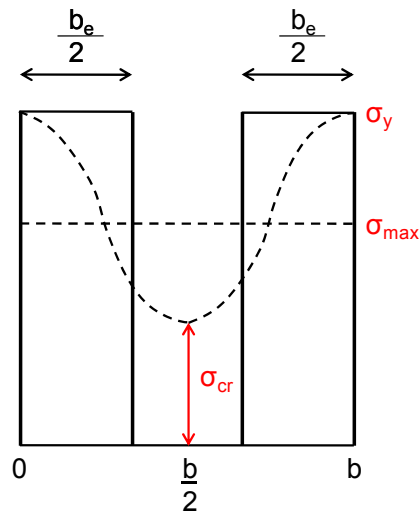
Then from Figure 2-6, the average stress ( $\sigma_{av}$ ) is calculated as

$$\sigma_{av} = \frac{b_e}{b} \sigma_e . \quad (2.9)$$

Substituting Equation (2.8) into (2.9) and assuming the edge stress ( $\sigma_e$ ) is equal to the yield stress ( $\sigma_y$ ), Equation (2.10) is derived (Galambos, 1988).

$$\sigma_{av} = \sqrt{\sigma_{cr} \sigma_y} \quad (2.10)$$

Figure 2-7 shows the stress distribution on the effective width of the plate and the basis of how Equation (2.10) was derived.



**Figure 2-7 Effective Width Stress Distribution (Allen, 1980)**

Imperfections in plates can lower the effective buckling stress as well as the ultimate strength values, thus the equations listed and described above have since been altered to account for numerous initial imperfections in plates such as; out-of-flatness, residual stresses, and strain hardening. They later became the foundations for current specifications regarding the subject.

### 2.3 Geometric Plate Imperfections

During various construction stages, geometric distortions and structural imperfections are created. Plate elements, particularly thin plates, always have initial out-of-flatness. Plate elements are subject to residual stresses during the welding process, in which compressive stresses are formed where the weld metal cools and shrinks. Residual stresses result premature yielding on the cross-section that lowers the effective stiffness of the built up member. The residual stresses can also deform the original element. Figure 2-8 shows some typical out-of-plane deviations.

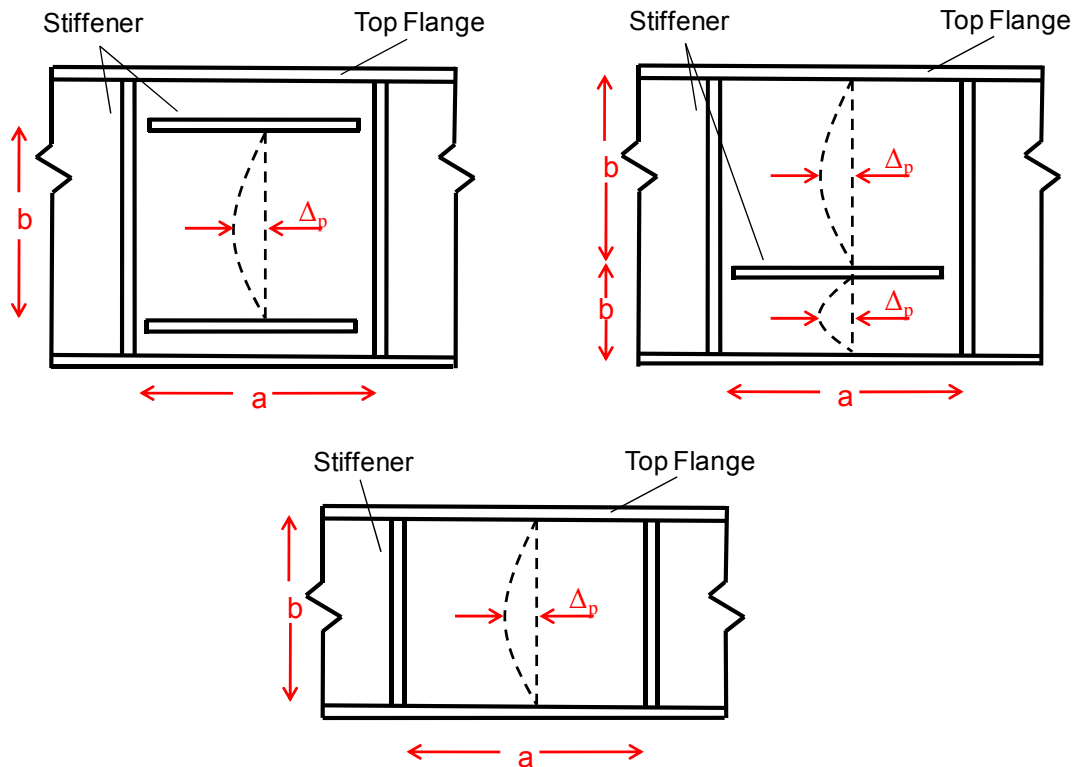
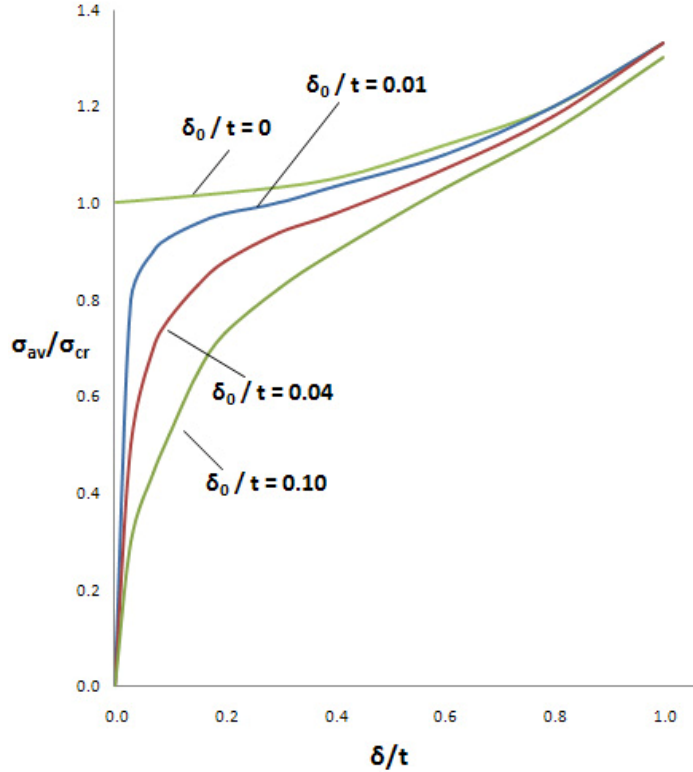


Figure 2-8 Out-of-Plane Deviations (Korol & Thimmhardy, 1987)

The panels shown include stiffeners that are positioned transversely and longitudinally in different configurations. The stiffeners contain initial out-of-flatness magnitudes and can be affected by the welding process much like the panels.

There are references to the effects of initial imperfections on past studies on plate buckling; however, the conclusions and recommendations vary with recent work. The linear elastic buckling theory presented earlier neglects imperfections in plates. Allen et. al 1980 studied plate theory and its relation to initial imperfections. Figure 2-9 depicts the effects of initial imperfections on a plate element. In the figure,  $\delta_o$  represents the initial deviation from flatness,  $\delta$  represents the additional plate deflection and  $t$  is the thickness of the plate. The figure shows that the effects of out-of-flatness reduce the initial stiffness of the plate, which leads to lower strength values. With this logic, even at loads below the buckling capacity, plates with bigger imperfections will experience larger displacements compared to plates with smaller imperfections. From the figure, it is also shown that the larger the initial imperfections, the larger the overall displacement.

Thimmhardy and Korol et. al. 1984 studied plate deviations in box girder systems. Their research showed that plate out-of-flatness increased as panel thickness decreased, however, more extensive research relating imperfections to strength was suggested (Korol & Thimmhardy, 1984). Research concluded that the magnitude of the out-of-plane deviations were a function of the plate panel width-to-thickness ratio. Further research provided tolerance recommendations for panels and stiffeners for Canadian specifications.



**Figure 2-9 Deflection of Plates with Initial Deviation (Allen, 1980)**

Herman et. al. 2001 studied and performed numerous tests on box girder plates with different stiffener configurations and types. During the tests, initial imperfections were measured and analyzed. Imperfections were measured again at different stages during the welding process as well as the installation of the plates on the testing apparatus. As expected, imperfections were shown to increase during these events. The imperfections were then compared to specification tolerances. Results showed that the initial imperfections affected the response of the test plates, specifically the load-displacement response. In addition, the study concluded that the impact of the imperfection is directly related to its magnitude (Herman, 2001).

As part of the research investigation reported in this thesis, Mercan et. al. 2005 presented results from as-fabricated imperfections in trapezoidal box girder systems. The measurements showed that the deformation patterns created by imperfections were random with no definite shapes. Mercan's work resulted in one of the largest compilations of as-fabricated plate imperfection measurements. A total of 23 box girder segments were measured producing 814 web imperfection readings and 446 bottom flange readings. The shapes of the imperfections that were measured consisted of single-curvature (both concave up and down) or double-curvature waves. Although the majority of the imperfection shapes were single-curvature, approximately 25% of the webs and 12% of the bottom flanges experienced double-curvature imperfections. Mercan's work is currently being used as input for parametric finite element studies on the effects of imperfections on the structural behavior of steel girder systems.

## **2.4 Tolerances**

Tolerance values for plate members exist in many specifications, codes, and design manuals. However, tolerance levels vary from source to source. The main reason for the variability is probably due to the fact that most sources base their values from different research findings. This especially holds true when comparing American tolerance levels to International values. Structural members composed of plate elements are used in many different applications throughout the world. For instance, many countries in Europe utilize multi-cell box girder bridge systems, whereas the United States focuses on single-cell box girder systems. Research in different countries tends to follow the local common practice, thus resulting in different conclusions and tolerance



recommendations. This section will further provide an overview of the numerous tolerance specifications used throughout the world.

#### **2.4.1 American Specifications**

United States specifications have variability in the tolerance values specified for plate elements. While some specifications include specific tolerances for various cross-sectional components, others simply reference other sources. The following specifications were reviewed:

- ASTM A6/A 6M-06 Standard Specification for General Requirements for Rolled Structural Steel Bars, Plates, Shapes, and Sheet Piling (2006),
- AASHTO/AWS D1.5M/D1.5 Bridge Welding Code (2002),
- AASHTO Standard Specification for Highway Bridges (2002),
- AASHTO Guide Specifications for Horizontally Curved Steel Girder Highway Bridges (2003), and
- AISC Load and Resistance Factor Design Specification for Steel Buildings, Manual of Steel Construction (2001).

The specifications of the American Society of Testing & Materials (ASTM) acknowledge dimensional tolerances for steel plates. Plate fabrication tolerances are discussed in ASTM A6/A6M Standard Specification for General Requirements for Rolled Structural Steel Bars, Plates, Shapes, and Sheet Piling. The basis and reasoning for the selection of the tolerances are unclear. Out-of-flatness tolerances for plates were first specified in ASTM A6-58 and were generally more relaxed than current specifications (Herman, 2001). Permitted variations in flatness for carbon steel plates are

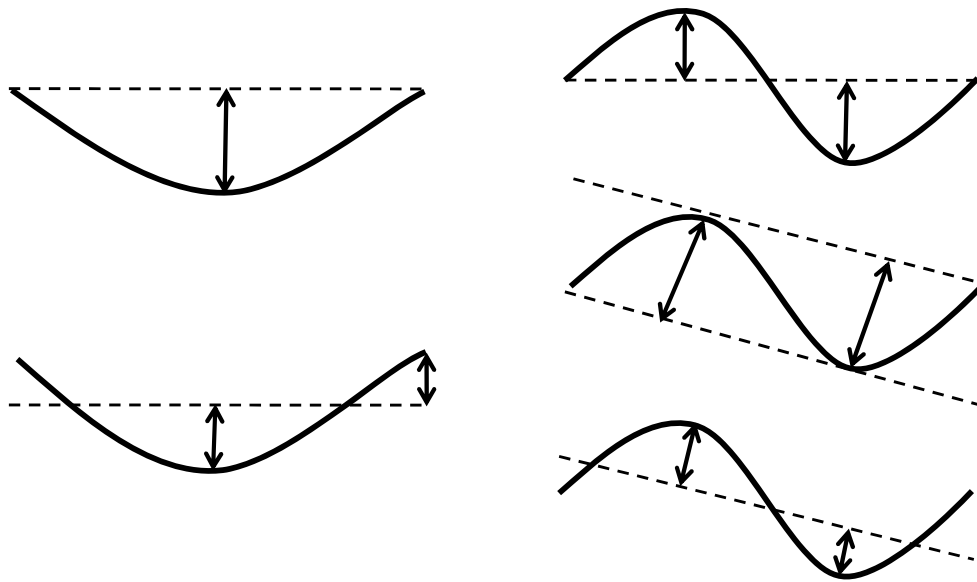
presented in Table 13 of ASTM A6 and are shown in Figure 2-10. According to the notes associated with the table, values specified in the tables can be increased up 50% for plates that have a minimum tensile strength greater than 60 ksi. With a known thickness or weight of a plate, along with the width, a permitted variation can be found in the table. However, the specification does not clearly explain how to measure the variations. The specification simply states that the plate must be in a horizontal position on a flat surface when measured. No details are provided regarding how the out-of-flatness should be measured. Herman et. al 2001 presented the possible measuring variations depicted in Figure 2-11. As shown in the figure, while ASTM A6 is relatively vague about the measuring techniques, there are multiple measuring variations for simple half wave shapes as well as double wave shapes. According to Herman, TxDOT representatives were interviewed regarding the methods used in the practice of measuring the out-of-flatness of plate members. The method was further described as using a 12-ft. straightedge that would touch the plate in 2 separate locations, maximizing the distance between the plate surface and the straightedge. The distance measured would then be used and compared to the tolerance values. Figure 2-12 depicts this method. As shown from the figure, it is likely the measured out-of-flatness is dependent on one the side of the plate that is measured which may necessitate measurements on both sides of the plate.

		Permitted Variations from a Flat Surface for Specified Widths Given in Inches, in.												
Specified Thickness, in.	Specified Weight, lb/ft <sup>3</sup>	to 36	36 to 48	48 to 60	60 to 72	72 to 84	84 to 96	96 to 108	108 to 120	120 to 144	144 to 168	168 and over		
		9/16	3/4	15/16	1 1/4	1 3/8	1 1/2	1 5/8	1 3/4	1 7/8	...	...	...	...
to 1/4	to 10.2	9/16	3/4	15/16	1 1/4	1 3/8	1 1/2	1 5/8	1 3/4	1 7/8	...	...	...	...
1/4 to 3/8	10.2 to 15.3	1/2	5/8	3/4	15/16	1 1/8	1 1/4	1 3/8	1 1/2	1 5/8	...	...	...	...
3/8 to 1/2	15.3 to 20.4	1/2	9/16	5/8	5/8	3/4	7/8	1	1 1/8	1 1/4	1 7/8	2 1/8	...	...
1/2 to 3/4	20.4 to 30.6	7/16	1/2	9/16	5/8	5/8	3/4	1	1	1 1/8	1 1/2	2	...	...
3/4 to 1	30.6 to 40.8	7/16	1/2	9/16	5/8	5/8	5/8	3/4	7/8	1	1 3/8	1 3/4	...	...
1 to 2	40.8 to 81.7	3/8	1/2	1/2	9/16	5/8	5/8	5/8	5/8	5/8	11/16	1 1/8	1 1/2	1 1/8
2 to 4	81.7 to 163.4	5/16	3/8	7/16	1/2	1/2	1/2	1/2	1/2	9/16	5/8	7/8	1	1 1/8
4 to 6	163.4 to 245.1	3/8	7/16	1/2	1/2	9/16	9/16	5/8	3/4	7/8	7/8	7/8	1	1 1/8
6 to 8	245.1 to 326.8	7/16	1/2	1/2	5/8	11/16	3/4	7/8	7/8	1	1	1	1	1 1/8
8 to 10	326.8 to 409.0	1/2	1/2	5/8	11/16	3/4	13/16	7/8	15/16	1	1	1	1	1 1/8
10 to 12	409.0 to 490.1	1/2	5/8	3/4	13/16	7/8	15/16	1	1	1	1	1	1	1 1/8
12 to 15	490.1 to 613.0	5/8	3/4	13/16	7/8	15/16	1	1	1	1	1	1	1	1 1/8

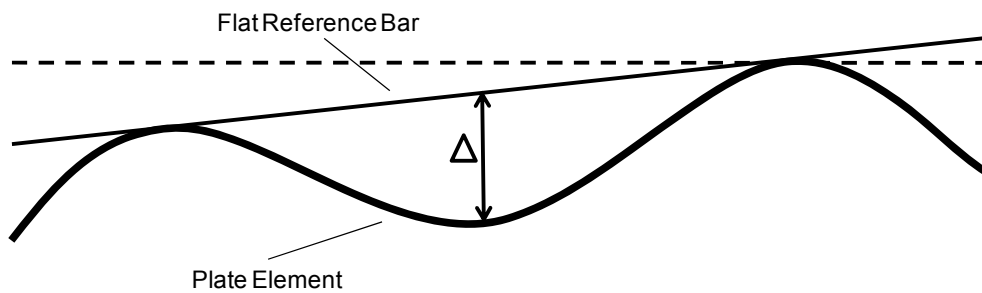
Notes:

1. When the longer dimension is under 36 in., the permitted variation from a flat surface shall not exceed 1/4 in. When the longer dimension is from 36 in. to 72 in., incl, the permitted variation from a flat surface shall not exceed 75% of the tabular amount for the specified width, but in no case less than 1/4 in.
2. These permitted variations apply to plates that have a specified minimum tensile strength of not more than 60 ksi or comparable chemical composition or hardness. The limits in this table are increased 50% for plates that have a higher specified minimum tensile strength or comparable chemical composition or hardness.
3. This table and these notes cover the permitted variations from a flat surface for circular and sketch plates, based upon the maximum dimensions of such plates.
4. Where "..." appears in the table, there is no requirement.
5. Plates must be in a horizontal position on a flat surface when flatness is measured.

Figure 2-10 Permitted Tolerances for Carbon Steel Plates (ASTM A6, 2006)



**Figure 2-11 Possible ASTM Measurement Variations**

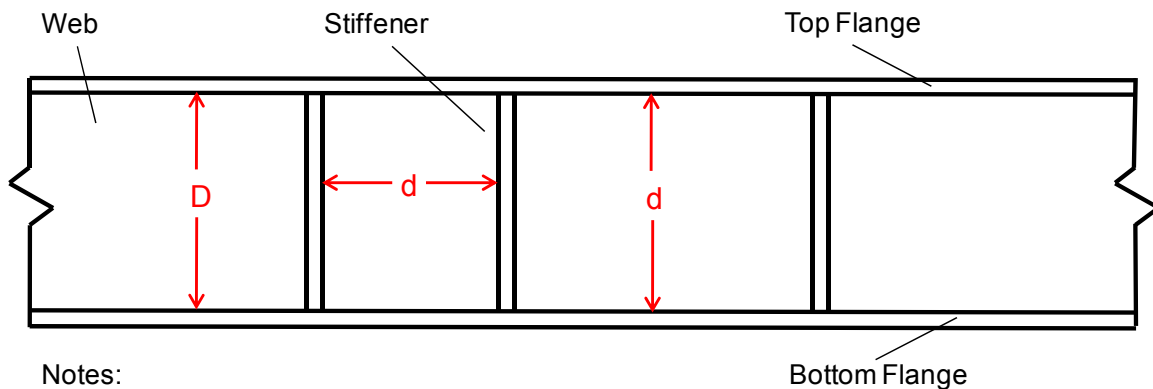


**Figure 2-12 Common Method of Measuring ASTM Out-of-Flatness**

As reported in earlier sections, the welding process is capable of producing additional stresses that lead to out-of-flatness in plates. The American Welding Society (AWS) addresses tolerance limits in Section 3.5 of the AASHTO/AWS D1.5 Bridge Welding Code (2002). The specification provides limits on maximum out-of-flatness values for different I-girder web configurations, as shown in Figure 2-13. Figure 2-14 shows the dimensions used;  $D$  and  $t$  are the depth and thicknesses of the web, while  $d$  is the least dimension of the panel bounded by stiffeners or flanges.

<p><b>Intermediate stiffeners on both sides of web:</b></p> <p><i>Interior Girders:</i>  where <math>D/t &lt; 150</math> - maximum variation = <math>d/115</math>  where <math>D/t \geq 150</math> - maximum variation = <math>d/92</math></p> <p><i>Fascia Girders:</i>  where <math>D/t &lt; 150</math> - maximum variation = <math>d/130</math>  where <math>D/t \geq 150</math> - maximum variation = <math>d/105</math></p> <p><b>Intermediate stiffeners on one side of web:</b></p> <p><i>Interior Girders:</i>  where <math>D/t &lt; 100</math> - maximum variation = <math>d/100</math>  where <math>D/t \geq 100</math> - maximum variation = <math>d/67</math></p> <p><i>Fascia Girders:</i>  where <math>D/t &lt; 100</math> - maximum variation = <math>d/120</math>  where <math>D/t \geq 100</math> - maximum variation = <math>d/80</math></p> <p><b>No intermediate stiffeners - maximum variation = <math>D/150</math></b></p>
--

**Figure 2-13 Tolerances for I-Girder Webs (Bridge Welding Code, 2002)**

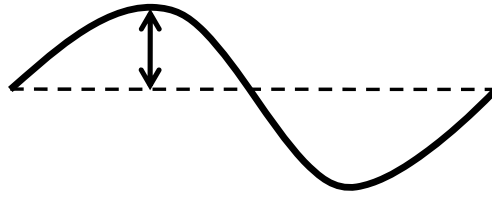


- Notes:
- D = depth of web
  - d = least panel dimension

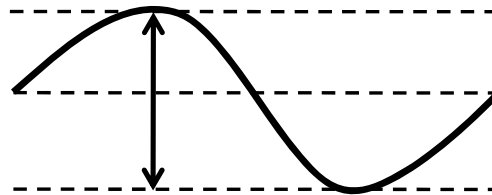
**Figure 2-14 Girder-Web Dimensions (Bridge Welding Code, 2002)**

While the AWS D1.5 specification seems to be straight-forward and somewhat more organized than the ASTM A6 specification, there are still some uncertainties. First and foremost, AWS D1.5 is specifically directed at the webs of I-girders. Nothing is mentioned regarding the suggested tolerances to box girder plate elements. Research by Mercan (2005) suggests that fabricators apply the AWS D1.5 specification to box girder web and bottom flange elements, mainly due to the fact that box girder provisions are lacking. However, Mercan (2005) also stated that AISC officials were against the use of AWS D1.5 for individual box girder elements. When compared to the ASTM A6 specification Mercan found that the ASTM tolerances were less stringent than the AWS D1.5 values. As stated earlier, ASTM A6 does not specify details pertaining to the method required for measuring out-of-flatness values other than placing the plate on a flat surface to measure the maximum deviation. Thus, it is assumed that ASTM A6 would result in measuring the distance from the extremities of two different waves in the shape. However, AWS D1.5 briefly describes a recommended method that produces different results. According to AWS D1.5 Bridge Welding Code, a straight edge must be placed between the two edges of the panel, meaning the out-of-flatness is measured from the center-line of the plate to the peak of a wave. Both methods are shown in Figure 2-15 and prove that different magnitudes of imperfections are measured (Mercan, 2005). Different methods used in measuring imperfections may be reasoning behind the inconsistencies in the tolerance values between the two specifications, specifically when measuring panel with a reverse curvature shape of deformation.

AWS D1.5  
Method



ASTMA6  
Method



**Figure 2-15 Imperfection Measuring Method Variance (Mercan, 2005)**

Plate tolerances are further reviewed in the AASHTO Standard Specifications for Highway Bridges (2002). The specification refers to orthotropic-deck superstructures with an emphasis on box girder plate elements. The specification limits the dimensional tolerances for members that are completed, but unloaded. The deviation from detailed flatness or straightness at any point is defined as “the perpendicular distance from that point to a template edge which has the detailed straightness or curvature and which is in contact with the element at two other points (AASHTO Hwy Bridge, 2002).” Detailed specifications for the template edge are also provided, a description of which is provided in Figure 2-16.

### 11.4.13.2 Flatness of Panels

(a) The term “panel” as used in this article means a clear area of steel plate surface bounded by stiffeners, webs, flanges, or plate edges and not further subdivided by any such elements. The provisions of this article apply to all panels in the bridge; for plates stiffened on one side only such as orthotropic-deck plates or flanges of box girders, this includes the total clear width on the side without stiffeners as well as the panels between stiffeners on the side with stiffeners.

(b) The maximum deviation from detailed flatness or curvature of a panel shall not exceed the greater of:

$$\frac{3}{16} \text{ inch or } \frac{D}{144\sqrt{T}} \text{ inch}$$

where,

- D = the least dimension in inches along the boundary of the panel
- T = the minimum thickness in inches of the plate comprising the panel.

**Figure 2-16 Flatness of Panels Specification (AASHTO Hwy Bridge, 2002)**

The AASHTO Guide Specifications for Horizontally Curved Steel Girder Highway Bridges (2003) simply refers the user to the Bridge Welding Code and notes that flatness should be measured with respect to a straight edge. The AISC LRFD Specifications for Steel Buildings Manual of Steel Construction (2001) limits tolerances in accordance with ASTM A6.

In summary, although many specifications provide tolerance limits to out-of-flatness, there are many issues still regarding the subject in the United States. Most specifications provide no basis for their proposed limits. There is also confusion as to



how to measure out-of-flatness, with methods differing depending on the specification referenced. One of the goals of the overall project, of which this thesis is a part, is to recommend a consistent method of measuring plate out-of-flatness.

#### **2.4.2 International Specifications**

Plate tolerances are specified in numerous international standards, codes, and guides. A variety of maximum limits are presented in European, Britain, and Japanese codes. Common construction practices differ throughout the world, and thus research and field studies lead to different results and recommendations. The variation of in the specified tolerances of various countries is outlined in this section.

Even though different countries may provide different tolerances, most specifications measure out-of-flatness based on the imperfection depicted in Figure 2-17. Tolerances throughout the European countries had a large variability before the development of the Eurocode 3 Design of Steel Structures (1993). Tolerance values from various countries in Europe ranged from  $b/133$  to  $b/500$ . As stated earlier, it is typical for individual countries to base their own specifications on common practice and knowledge, which would differ in various parts of the world. Various plate tolerance limits throughout Europe prior to the 1993 Eurocode are shown in Figure 2-18.

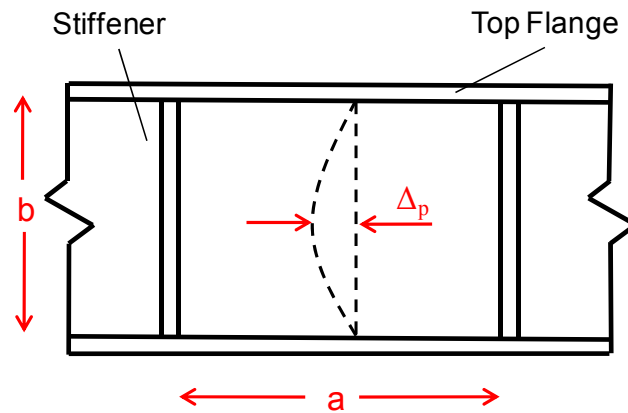
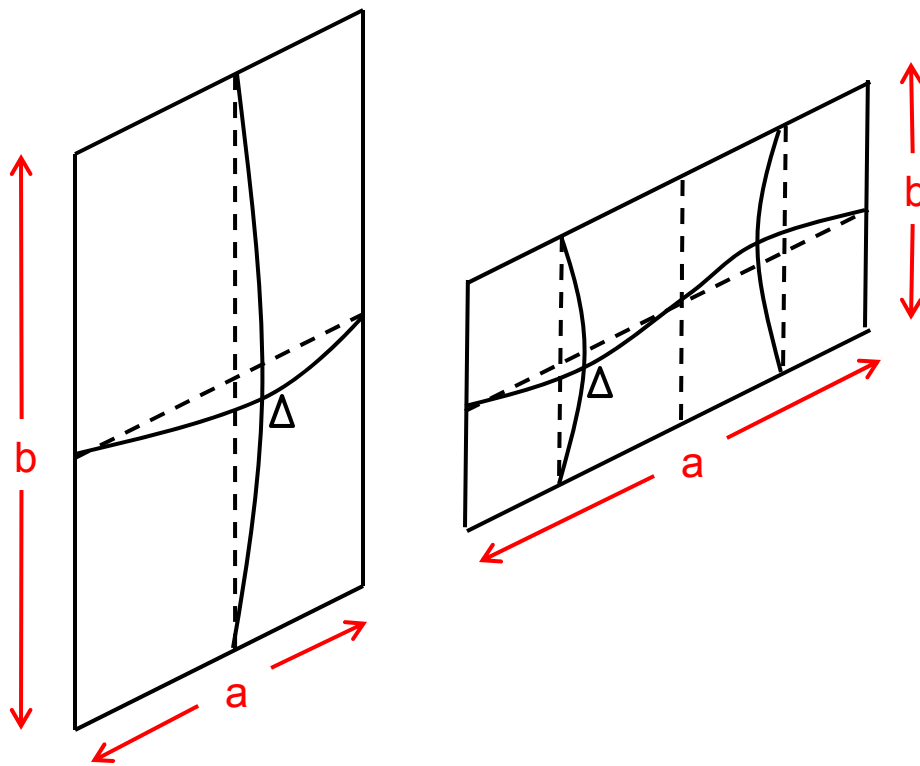


Figure 2-17 Typical Imperfection Measurement (Korol & Thimmhardy, 1987)

Code	Country	Permissible out-of-plane deviations	Notes
ONORM B 4600 (1975)	Austria	$a/250$ or $b/250$	a: length of stiffener or length of the half wave of stiffener buckling mode
NBN B51-001	Belgium	$a/250$ or $b/250$ max: 4mm	
DAST 012 (1978)	West Germany	$a/250$ or $b/250$	
C N R	Italy	$a/400$ or $b/400$	stated for web panels
SIA-161 (1979)	Switzerland	$a/250$ or $b/250$	for unstiffened webs of plate girders, the max out-of-plane deflections $\Delta_o$ are prescribed with reference to a gauge length of 2 m. $\Delta_o = 5$ mm for railway bridges and $\Delta_o = 8$ mm for highway bridges
St. BK-N1	Sweden	$b/150$	valid for the web of a beam subjected to a bending moment
European Recomm. For Steel Const. (1978)	ECCS	$a/500$ or $b/500$	
NS 3472	Norway	$b/133$	valid for the web plate

Figure 2-18 Plate Tolerances in European Specifications (Mercan, 2005)

The Eurocode 3 Part 1.5 (EN 1993-1-5 2003) provides specifications for plate structures. The specification addresses both global and local imperfection tolerances. According to the specification, the shape and magnitude of the geometric imperfections should be considered. Figure 2-19 shows details providing proper use of the specification. The tolerance limit of the imperfection is the smaller of  $a/200$  or  $b/200$  (Mercan, 2005).



**Figure 2-19 Panel Imperfection Details (Eurocode 3, 2003)**

The Japan Road Association published the 1973 Specifications for Highway Bridges which contains tolerances on out-of-plane imperfections. The specification went as far as specifying tolerances for box girder plate members. The tolerances provided are  $b/150$  for the flanges of box girders and  $b/250$  for the web panels (JSHP, 1973).

BS5400 Part 6 in the United Kingdom specifies maximum initial imperfections with Equation (2.11). In the specification,  $\Delta_o$  is the imperfection,  $L$  is the gauge length and  $f_y$  is the material yield strength. The gauge length is the smaller of  $a$  or  $2b$ . It should be recognized that the specification is one of the only in the world to limit the imperfection based on material strength. The equation is in SI units and requires the use of 250 or 350 N/mm<sup>2</sup> to be used as  $f_y$  (BS5400, 1970).

$$\Delta_o \leq \frac{L}{165} \sqrt{\frac{f_y}{355}} \quad (2.11)$$

## **CHAPTER 3**

### **Field Measuring Instrumentation and Techniques**

#### **3.1 Introduction**

An overview of the geometry and instrumentation layout for the twin girder bridge that was monitored at Ferguson Structural Engineering Laboratory (FSEL) is provided in this chapter. A discussion of the sensors that were used to monitor strain values is reviewed along with the data acquisition system used. The chapter also provides an overview of the instrumentation and processes used to measure the out-of-flatness of the web and flange plate members. Results from the laboratory measurements are discussed and compared to predictions from a finite element computer model in the proceeding chapters.

#### **3.2 Instrumented Bridge**

The bridge used for the field studies is a single span steel twin trapezoidal box girder system. The bridge was originally a segment of the Interstate 10 highway located in Houston, Texas. The top flanges and webs of the girders were heavily deformed during removal of the concrete bridge deck. The girders were sent to Trinity steel fabricators in Houston for straightening. The girders were then transported to the Phil M. Ferguson Structural Engineering Laboratory located at the J.J. Pickle Research Center campus in Austin, Texas. A map of the bridge location is presented in Figure 3-1. The satellite image shows the abutments that had been constructed prior to transport of the girders from Houston to FSEL. The girders were be erected and assembled, followed by

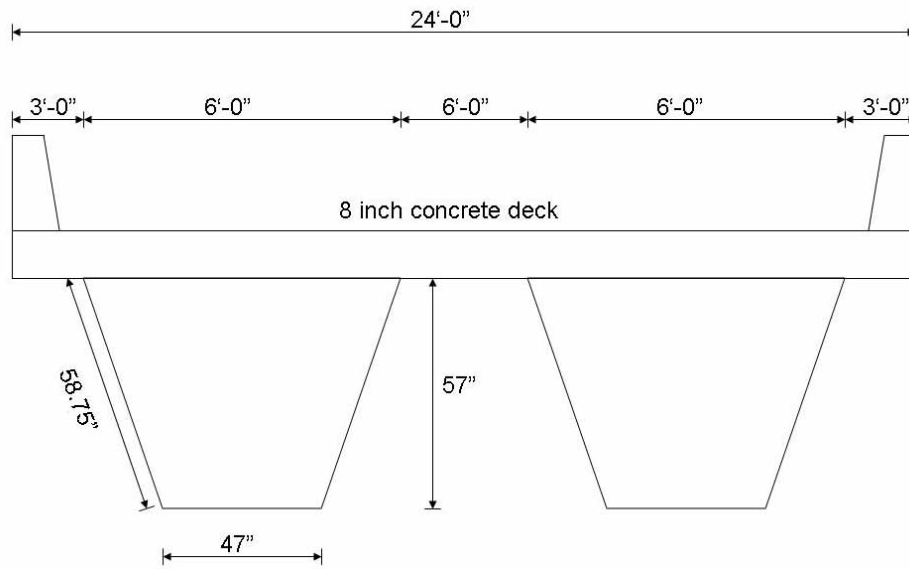
the construction of an 8 inch thick concrete deck thereby creating a composite bridge system. The pier assemblies, erecting of the girders, and construction of the concrete deck and rails were performed in coordination with local contractors and TxDOT officials. While the relocation of an existing bridge was a difficult endeavor, several research projects benefited from this system.



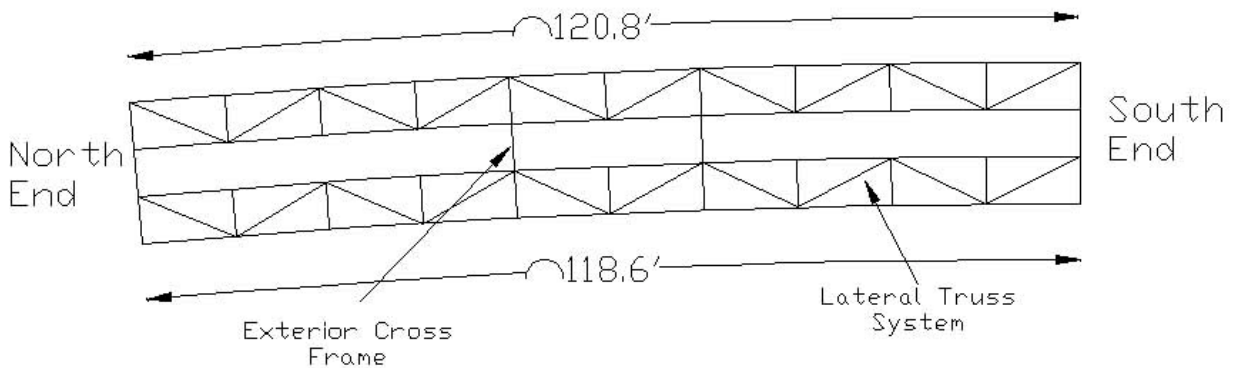
**Figure 3-1 Bridge Location at Ferguson Laboratory (Microsoft, 2007)**

The bridge is comprised of two single span units, with span lengths of 119 and 121 feet respectively. The girders curved slightly from right to left, with the west girder having a slightly longer span. The radius of curvature at the centerline of the bridge was 1365.393 feet. Steel trapezoidal girders consist of two top flanges, one bottom flange, and two inclined webs. The depth and box width of the girders are usually uniform along the length of the bridge, however the plate thickness and the top flange widths vary at locations throughout the bridge. The typical cross section of the bridge is shown in

Figure 3-2. External solid plate diaphragms were provided at the supports and a top flange lateral truss system was used along the length of the girders. External cross-frames were provided at two locations, approximately 12 feet away from midspan in each direction. A plan view showing the span lengths, lateral truss orientation, and cross-frame locations is provided in Figure 3-3.



**Figure 3-2 Cross-Section of Box Girder Bridge**



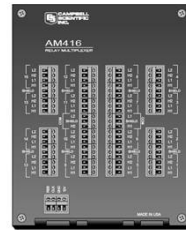
**Figure 3-3 Plan View of Instrumented Bridge**

### 3.3 Data Acquisition System

The data acquisition system used on the instrumented bridge included equipment manufactured by Campbell Scientific, Inc. The main components of the system included 3 CR5000 Dataloggers, 16 AM416 Relay Multiplexers, 2 AVW100 Vibrating Wire Interfaces, 44 4WFB350 4 Wire Full Bridge Terminal Input Modules, and 103 4WFB120 4 Wire Full Bridge Terminal Input Modules. Figure 3-4 shows pictures of these instruments. The instrumentation components are discussed in further detail in the following sections.



CR5000 Datalogger



AM416 Relay Multiplexer



4 Wire Bridge Module



AVW100 Interface

Figure 3-4 Data Acquisition System Components

#### 3.3.1 CR5000 Datalogger

The CR5000 datalogger shown in Figure 3-4 provided the backbone for recording and storing data on the project. The CR5000 provides precision measurement capabilities in lieu of being a versatile, portable, and durable instrument. The datalogger



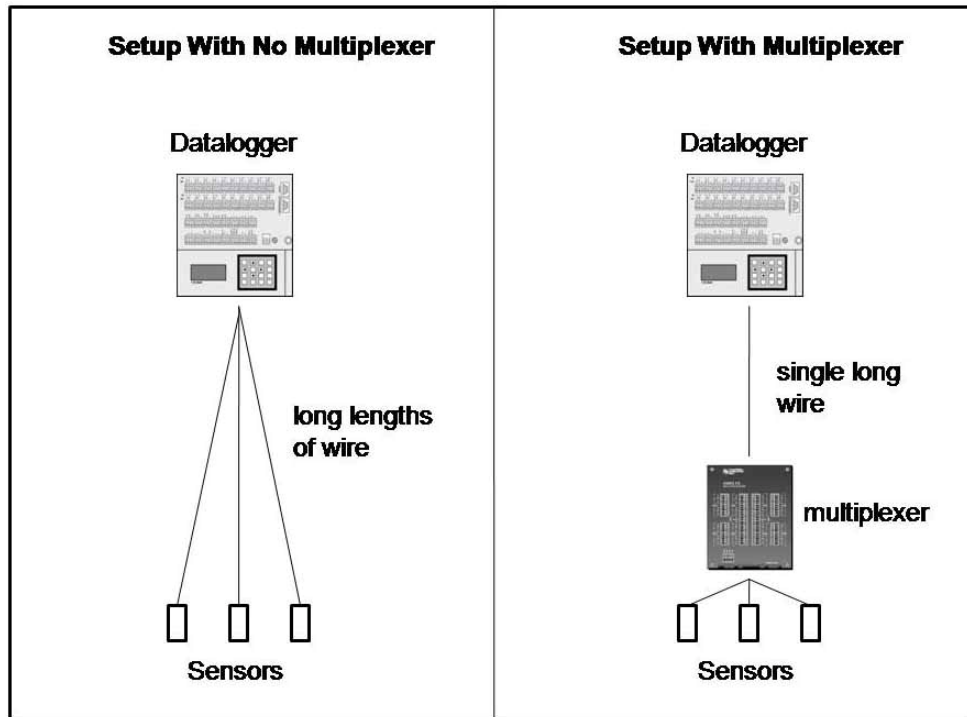
is able to make measurements at a rate of up to 5,000 samples/second with 16-bit resolution. The CR5000 includes the CPU, a keyboard display, internal power supply, and analog and digital inputs and outputs. The internal battery supply can be interchanged with a rechargeable battery base, or by a 12V external battery source. The CR5000 is equipped with a BASIC-like programming language and includes data processing and analysis commands. Although the datalogger can be programmed directly using the keypad, the CR5000 also has the ability to sync to a computer through the supplied serial port and programmed using with the software PC9000. In addition to programming, the PC9000 software can be used to perform other tasks such as file and data transferring and downloading, as well as real time data monitoring. PC9000 is the software provided by Campbell Scientific, Inc. and is included with the purchase of the CR5000 datalogger (Campbell, 2001).

The CR5000 has the ability to connect and monitor 40 single-ended connections or 20 differential connections. Voltage measurements of up to 5V can be read with the datalogger. Within the CR5000 wiring panel, a thermistor is included and can be used as a reference temperature for thermocouple measurements. The CR5000 has four switched excitation channels to provide programmable voltages within the  $\pm 5V$  range for bridge measurements. Four switched current excitation channels are also available and provide programmable currents within the  $\pm 2.5$  mA range for resistance or bridge measurements. The CR5000 is equipped with an internal memory, however the size is limited. For this reason, the datalogger has a slot for Type 1, 2, or 3 PCMCIA memory cards that can be used to increase the memory capacity. With the use of the memory cards, a large amount of data can be stored from the datalogger and directly transferred to a computer without the use of a serial link chord (Campbell, 2001).

### **3.3.2 AM416 Relay Multiplexer**

Although the data the number of channels on the data logger is limited as outlined in the previous section, the number of sensors can be substantially increased using multiplexers. A multiplexer acts like a switch that is linked between the datalogger and the sensors. The AM416 is intended to be used in applications where the required number of sensors exceeds the number of input channels on the datalogger input channels. The multiplexer can allow up to 32 single-ended or differential sensors that do not require excitation (thermocouples) and up to 16 single-ended or differential sensors that do require excitation (full bridge measurements). In addition to increasing the number of channels that can be monitored, another main advantage of using a multiplexer is the fact that the overall length of wiring required in the system can be reduced. This benefit is especially important when field monitoring points are far apart. Figure 3-5 shows an example of this (Campbell, 1996).

The CR5000 datalogger is not capable of directly reading the vibrating wire strain gages, and therefore an interface attachment is needed. The AVW100 Interface was used in conjunction with the instrumentation setup. In theory, each vibrating wire strain gage should be connected to an interface, and then the interface connected to the datalogger. However, in practice, each vibrating wire strain gage is connected to the multiplexer, which is then connected to a single interface that is connected to the datalogger. This efficient method was practiced in the instrumentation of the box girder bridge system.



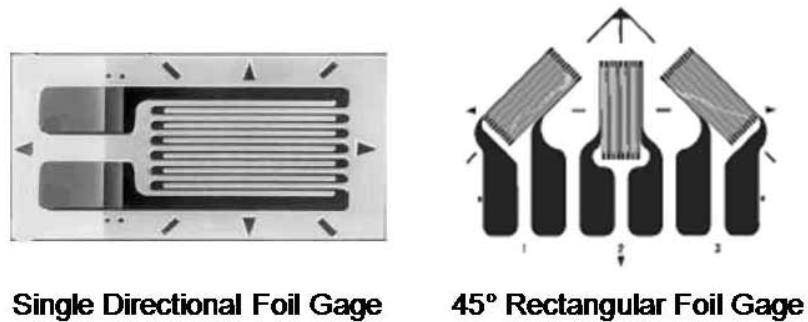
**Figure 3-5 Multiplexer Scenarios**

### **3.4 Sensor Measuring Devices**

The devices used on the instrumented bridge were able to measure strain and temperature values. In order to read resistive strain values, single directional foil strain gages and rectangular 0-45-90 rosette foil strain gages were used. A third type of strain gage was also used. Vibrating wire strain gages are capable of measuring strain and temperature changes and were used. Using three types of strain devices was important in comparing the validity of the readings and would lead to future recommendations of gage choice. For thermal readings, Type T thermocouples were used.

### 3.4.1 Resistive Strain Measurement Devices

Resistive strain gages are widely used in applications to measure strain. The most common type of strain gage consists of an insulating flexible backing that supports a metallic foil pattern. The metallic strain gage consists of a very fine wire arranged in a grid-like pattern. The most common nominal resistance values available commercially are 120, 350, and 1000  $\Omega$ . Because of their economical pricing, short response time, and accurate results, they are the leading gage when used in most engineering applications. Typical resistive strain gages are shown in Figure 3-6 (Wikipedia, 2007).



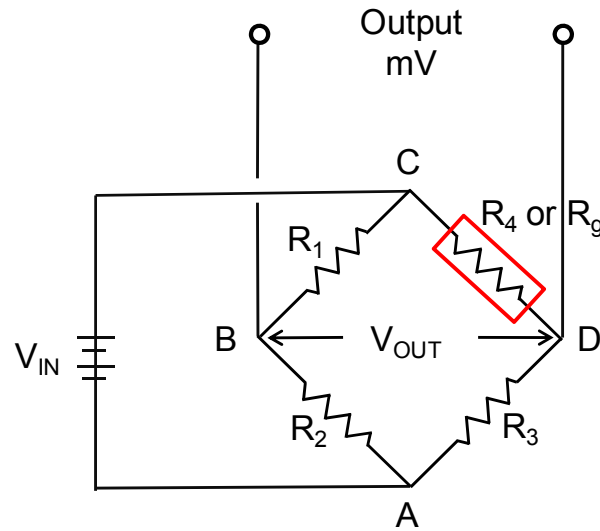
**Figure 3-6 Resistive Strain Gages**

Electrical resistance strain gages provide an indication in strain changes by monitoring the corresponding change in the electrical resistance for a differential strain. If tension is applied to a wire, the wire lengthens as the cross-section decreases. This changes the resistance,  $R$ , in proportion to the strain sensitivity of the wire's resistance. Strain sensitivity for a particular gage is given by the gage factor,  $GF$ , which is represented in Equation (3.1).  $\Delta R$  is the change in resistance and  $\Delta L$  is the change in length of the gage.

$$GF = \frac{\left(\frac{\Delta R}{R}\right)}{\left(\frac{\Delta L}{L}\right)} = \frac{\left(\frac{\Delta R}{R}\right)}{Strain} \quad (3.1)$$

The ideal strain gage would only experience a change in resistance due to the deformations of the surface of the specimen it is applied to. However, in the field temperature changes, the material properties of the specimen and the bond of the adhesive used to attach the gage to the surface may all affect the resistance. Preferably, the ideal strain gage is small in size and mass, economical in cost, easy to attach to the candidate surface, highly sensitive to the strain of that surface, but still insensitive to temperature variations (National, 2007).

To gain an indication of expected strain changes, Hooke's Law can be rearranged to solve for the strain  $\epsilon = \sigma/E$  within the elastic range of the material. For steel,  $E = 29000$  ksi and for a 1 ksi stress change the corresponding change in strain is 34.5 microstrains. Therefore ideally in structural applications the accuracy of the strain sensors should be within a few microstrains. To achieve this, the gage must be connected to an electrical circuit that is capable of measuring minute changes in resistance. A bridge configuration with a voltage excitation source, named a Wheatstone bridge, is preferably used to achieve this. Figure 3-7 shows the circuitry of a Wheatstone bridge.



**Figure 3-7 Wheatstone Bridge Circuit (National, 2007)**

The output voltage of a Wheatstone bridge is expressed in volt output per volt input. In Figure 3-7, if  $R_1$ ,  $R_2$ ,  $R_3$ , and  $R_4$  (or  $R_g$ ) are equal and a voltage is applied ( $V_{IN}$ ), then the circuit is balanced and there will be no voltage output. However, if  $R_4$  (or  $R_g$ ) is changed to a value not equal to  $R_1$ ,  $R_2$ , and  $R_3$ , then the bridge is unbalanced and an output voltage will be present making it possible to detect strain. Equation (3.2) shows the circuit balance.

$$V_{Out} = V_{In} \left[ \left( \frac{R_3}{R_3 + R_g} \right) - \left( \frac{R_2}{R_1 + R_2} \right) \right] \quad (3.2)$$

When Wheatstone bridge is setup so that  $R_g$  is the only active strain gage, a strain change in  $R_g$  will result in a voltage output, and can be converted to strain. Knowing the gage factor ( $GF$ ), the change in strain can be calculated using Equation (3.3) (Omega, 2007).

$$\Delta strain = \frac{\frac{\Delta R_g}{R_g}}{GF} \quad (3.3)$$

Rosette strain gages are similar in concept to that of the single directional foil strain gages. They consist of an arrangement of two or more closely positioned gage grids that are oriented specifically to measure the strains along different directions of the surface to which they are applied. The rosette strain gages used were 45° rectangular gages. The gage itself consists of 3 grids, a middle gage that is straight (as represented by a single directional foil gage), and 2 side gages, each oriented by 45° from the center gage. Rosettes are made of the same materials as single directional foil gages, and experience the same effects due to temperature changes, material properties, and adhesion bonds. The gage acts as 3 different strain gages and measures 3 different strain values. However, all of these values are needed to determine the principal strains using Mohr's Circle for strain. Hooke's Law is then used to determine the corresponding principal stresses. Equations (3.4) – (3.8) show the necessary calculations to convert the rosette strain values to a stress value. The equations are derived from a stress-transformation relationship.

$$\varepsilon_{max} = \frac{\varepsilon_1 + \varepsilon_3}{2} + \frac{1}{\sqrt{2}} \sqrt{(\varepsilon_1 - \varepsilon_2)^2 + (\varepsilon_2 - \varepsilon_3)^2} \quad (3.4)$$

$$\varepsilon_{min} = \frac{\varepsilon_1 + \varepsilon_3}{2} - \frac{1}{\sqrt{2}} \sqrt{(\varepsilon_1 - \varepsilon_2)^2 + (\varepsilon_2 - \varepsilon_3)^2} \quad (3.5)$$

$$\theta = \frac{1}{2} \tan^{-1} \left( \frac{\varepsilon_1 - (2 * \varepsilon_2) + \varepsilon_3}{\varepsilon_1 - \varepsilon_3} \right) \quad (3.6)$$

$$\sigma_{max} = \frac{E}{1 - \nu^2} * (\varepsilon_{max} + \nu(\varepsilon_{min})) \quad (3.7)$$

$$\sigma_{min} = \frac{E}{1 - \nu^2} * (\varepsilon_{min} + \nu(\varepsilon_{max})) \quad (3.8)$$

In the equations above,  $E$  is the modulus of elasticity of the material being monitored,  $\nu$  is Poisson's ratio,  $\varepsilon_{1,2,3}$  are the measured strain values from the rosette,  $\varepsilon_{min}$  and  $\varepsilon_{max}$  are principal strains,  $\theta$  represents the acute angle from the principal axis to the reference grid of the rosette, and  $\sigma_{min}$  and  $\sigma_{max}$  are the principal stresses. For Equations (3.7) and (3.8) to be true, the test material must be homogeneous in composition, and isotropic in its mechanical properties (Vishay, 2005). The stress-strain relationship is also assumed to be linear. The bridge specimen instrumented met these criteria and thus the equations were used to calculate stress values

The resistive strain gages used are quarter bridge circuits and will not function properly when directly connected to the CR5000 datalogger. The CR5000 is only capable of reading full quarter bridge circuits; therefore terminal input modules must be used in conjunction with the gages to achieve accurate results. The terminal input modules provide completion resistors for the strain gages. The 4WFB120 and 4WFB350 are the favored modules of choice, each containing a nominal resistance of either 120 or 350 ohms, respectively. Depending on the resistance of the strain gage utilized, the appropriate input terminal must be used. Figure 3-4 shows one of the 4 wire full bridge terminal input module that was used. The input terminal consists of 3 completion resistors;  $R_1$ ,  $R_2$ , and  $R_3$ . According to specifications,  $R_1$  and  $R_2$  always have an equal resistance of 1000  $\Omega$ .  $R_3$  is the resistance value that changes according to the type of module (120 or 350  $\Omega$ ).  $R_g$  represents the resistance provided through the strain gage. The terminal input modules are able to connect directly to the CR5000 datalogger or to AM416 relay multiplexers. Figure 3-8 shows the full bridge between an input terminal module and a strain gage.



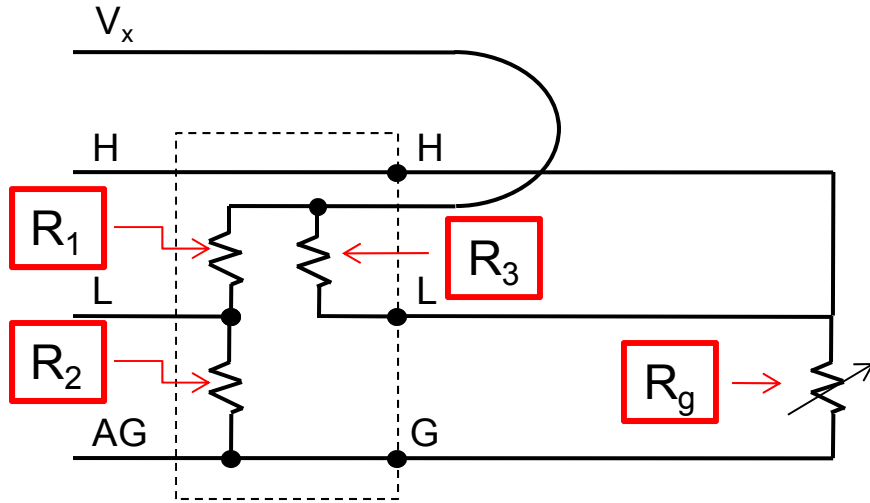


Figure 3-8 Strain Gage in Full Bridge (Campbell, 1996)

The CR5000 can be programmed to measure the output voltage of the bridge,  $V_{out}$  and then supplies the ratio of output voltage to input excitation voltage ( $V_{in}$ ). In theory, the output voltage is small relative to the provided excitation voltage, thus making it easier for the datalogger to read and record. The following equations show the steps of calculating the change in strain within the circuit. The direct ratio of voltages can be expressed as

$$\frac{V_{out}}{V_{in}} = \frac{R_g}{R_3 + R_g} - \frac{R_2}{R_1 + R_2} \quad (3.9)$$

The previous equation represents when the gage is unstrained. When the gage is strained, a resistance change occurs,  $\Delta R$ .

$$\left(\frac{V_{out}}{V_{in}}\right)_{strained} = \frac{R_g + \Delta R_g}{R_3 + R_g + \Delta R_g} - \frac{R_2}{R_1 + R_2} \quad (3.10)$$

Subtracting the unrestrained result from the strained result gives the difference in reference and strained measurements,  $V_r$ :

$$V_r = \left( \frac{V_{out}}{V_{in}} \right)_{strained} - \left( \frac{V_{out}}{V_{in}} \right) = \frac{R_g + \Delta R_g}{R_3 + R_g + \Delta R_g} - \frac{R_g}{R_3 + R_g} \quad (3.11)$$

The appropriate input terminal is used according to the resistance of the strain gage (120 or 350  $\Omega$ ). Therefore,  $R_3 = R_g$  and gives the following simplified equation:

$$V_r = \frac{\Delta R_g}{4R_g + 2\Delta R_g} \quad (3.12)$$

Rearranging Equation (3.12) and solving for strain gives the following equation:

$$\frac{4V_r}{1 - 2V_r} = \frac{\Delta R_g}{R_g} \quad (3.13)$$

Finally dividing both sides by the gage factor,  $GF$  yields the change in strain.

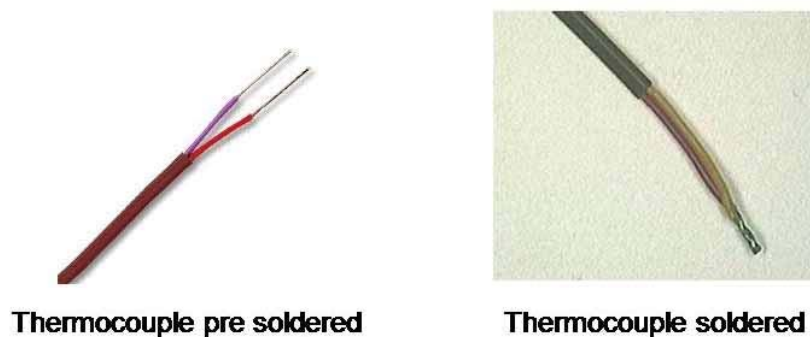
$$\Delta \varepsilon = \frac{4V_r}{GF(1 - 2V_r)} \quad (3.14)$$

Equation 3.14 is used by the CR5000 to calculate the change in strain for a full bridge circuit (Campbell, 1996)

### 3.4.2 Temperature Measurement Devices

There are a wide variety of temperature measuring devices, however, the thermocouple is the most common sensor used in the field. Because of their low cost, no moving parts, ability to measure a wide range of temperatures, reasonably accurate, short response time, and ruggedness, they are the leading candidate for temperature measurements.

In 1822 an Estonian physician named Thomas Seebeck discovered that the junction between two metals generates an electrical voltage that is a function of temperature (Pico, 2007). A thermocouple is simply a pair of junctions formed from two dissimilar metals. One junction is located at a reference point where the temperature is known and should stay constant. The other junction is located at the point where the temperature is to be measured. If one end of the thermocouple experiences a temperature that is different than the other end, an electrical voltage will be formed as a function of the temperature differential. Thermocouples generally come manufactured as a single coated wire. The ends must be stripped and the two separate wires within the coating must be separated, and then the ends of these wires must be soldered together. Figure 3-9 shows a before and after picture of thermocouples soldering.



**Figure 3-9 Thermocouples**

There are numerous types of thermocouples and each has their own unique advantages and properties. Certain thermocouples are meant for specific materials, while some are have designated temperature ranges at which they can accurately function. Table 3-1 shows numerous types of thermocouples and their working temperature ranges.

**Table 3-1 Temperature Ranges for Types of Thermocouples (Watlow, 2007)**

<i>Thermocouple Type</i>	<i>Temperature Range (°F)</i>
<b>B</b>	2500 – 3100
<b>C</b>	3000 – 4200
<b>E</b>	200 - 1650
<b>J</b>	200 – 1400
<b>K</b>	200 - 2300
<b>N</b>	1200 – 2300
<b>R</b>	1600 – 2640
<b>S</b>	1800 – 2640
<b>T</b>	32 - 660

Type T thermocouples were chosen for use in the field on this project. Type T thermocouples are composed of copper and constantan wires and generate 22 microvolts per °F. Because of their temperature range, they are used widely in the civil engineering field because most specimens tested never reach the upper limit of the temperature range. Thermocouple manufacturers produce tables that list millivolts according to temperature values for each type of thermocouple. The table format is usually the same throughout the industry, listing temperature increments in values of 10°F along the first column with

ranges in increments of 1°F usually along the top row. Once the proper temperature is located, the user can then read the millivolt value directly off the table. Table 3-2 is a portion of a Type T thermocouple voltage-temperature table.

However, the process of measuring the temperature is not as simple as connecting a thermocouple to a voltmeter, reading the voltage, and then using the tables to find the corresponding temperature. When the user attaches the voltmeter to one end of the thermocouple, a second unwanted junction is formed that will affect the measurements. Thus, the second junction should always be kept at a constant value, preferably 32°F. In the field, this is not practical and thus another method must be used. The CR5000 datalogger, as previously stated, contains a thermistor within itself. When the thermocouples are attached to the datalogger, the second junction is measured with the thermistor that is supplied by the datalogger. Because the temperature value of the thermistor is known, the CR5000 has the ability to calculate and correctly measure the thermocouple temperature without the effects of the second junction interfering, leading to an accurate and precise temperature measurement.

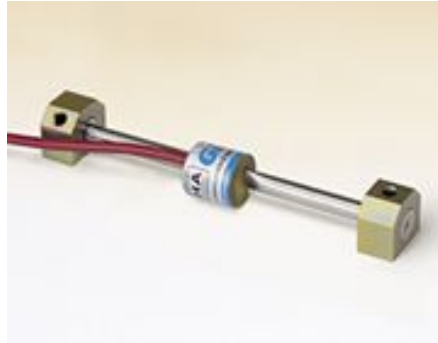
**Table 3-2 Type T Thermocouple Voltage-Temperature (ISE, 2007)**

°C	0	1	2	3	4	5	6	7	8	9
<b>Thermoelectric Voltage in mV</b>										
<b>0</b>	0.000	0.039	0.078	0.117	0.156	0.195	0.234	0.273	0.312	0.352
<b>10</b>	0.391	0.431	0.470	0.510	0.549	0.589	0.629	0.669	0.709	0.749
<b>20</b>	0.790	0.830	0.870	0.911	0.951	0.992	1.033	1.074	1.114	1.155
<b>30</b>	1.196	1.238	1.279	1.320	1.362	1.403	1.445	1.486	1.528	1.570
<b>40</b>	1.612	1.654	1.696	1.738	1.780	1.823	1.865	1.908	1.950	1.993
<b>50</b>	2.036	2.079	2.122	2.165	2.208	2.251	2.294	2.338	2.381	2.425
<b>60</b>	2.468	2.512	2.556	2.600	2.643	2.687	2.732	2.776	2.820	2.864
<b>70</b>	2.909	2.953	2.998	3.043	3.087	3.132	3.177	3.222	3.267	3.312
<b>80</b>	3.358	3.403	3.448	3.494	3.539	3.585	3.631	3.677	3.722	3.768
<b>90</b>	3.814	3.860	3.907	3.953	3.999	4.046	4.092	4.138	4.185	4.232
<b>100</b>	4.279	4.325	4.372	4.419	4.466	4.513	4.561	4.608	4.655	4.702
<b>110</b>	4.750	4.798	4.845	4.893	4.941	4.988	5.036	5.084	5.132	5.180
<b>120</b>	5.228	5.277	5.325	5.373	5.422	5.470	5.519	5.567	5.616	5.665
<b>130</b>	5.714	5.763	5.812	5.861	5.910	5.959	6.008	6.057	6.107	6.156

### 3.4.3 Combined Measurement Devices

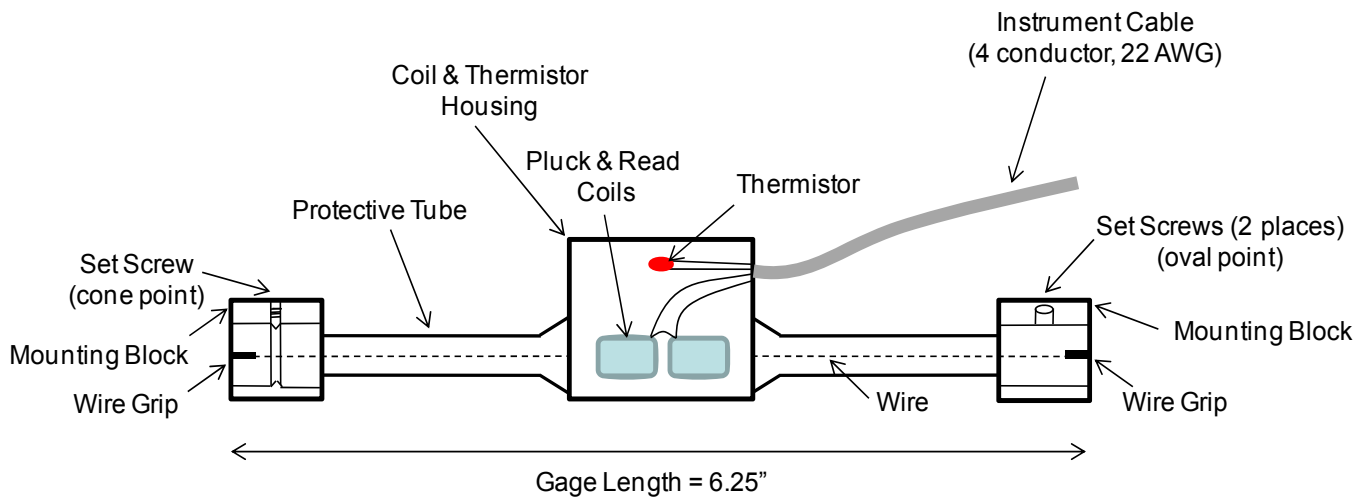
Resistive strain gages are often used in the field quite often due to their numerous advantages: however they are sometimes affected by temperature and age. Resistive strain gages have also been known to produce inaccurate results when used on long term projects since the gage readings can drift over time. In projects that are focused on long-term monitoring of strains, many researchers are experimenting with a new type of strain

reading device, the vibrating wire strain gage. Figure 3-10 shows a Geokon Model 4000 vibrating wire strain gage.



**Figure 3-10 Geokon Model 4000 Vibrating Wire Strain Gage**

Vibrating wire strain gages have many advantages. Since the gages work based upon mechanical means, they can provide long term consistent readings. The gages are much more rugged and durable than conventional. As a bonus, the gages are reusable and under the right conditions can provide stable long-term consistent results. Vibrating wire strain gages also have the ability to measure not only strain values, but temperatures as well. Another advantage is that wire lengths are not an issue and do not affect measurements, which can be a problem with resistive strain gages. One drawback to vibrating wire strain gages is that they are not suitable for the measurement of dynamic or rapidly changing strains. A detailed drawing of the vibrating wire gage can be seen in Figure 3-11.



**Figure 3-11 Vibrating Wire Strain Gage Schematic (Geokon, 2005)**

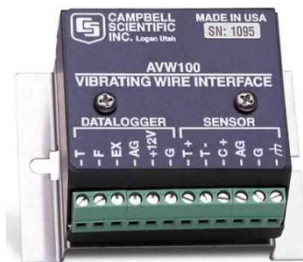
Strains are measured using the vibrating wire principle. Within the protective tube runs a thin steel wire that is tensioned prior to mounting. The gage is supported by two mounting blocks that can be bolted, welded, or epoxied to the surface of the specimen. Deformations on the specimen surface cause the mounting blocks to shift and change position causing the tension in the wire to change. The resonant frequency of vibration of the wire is a function of its tension, thus if the tension in the wire changes, so will the frequency of the gage. Attached to the gage is a unit that houses a thermistor and pluck & read coils. This housing unit plucks the thin steel wire and the electromagnetic coils then measure the frequency. The frequency can then be converted to strain values. As previously stated, the vibrating wire strain gage housing unit also contains a thermistor. A change in the thermistor's temperature causes a change in its resistance. A relationship between the resistance and temperature of the device can be defined using the Steinhart-Hart equation:

$$T = \frac{1}{A + B(\ln R) + C(\ln R)^3} - 273.2, \quad (3.15)$$



where  $A$ ,  $B$ , and  $C$  are constants that are given in the Geokon Model 4000 Vibrating Wire Strain Gage Instruction Manual,  $R$  is the resistance of the thermistor in ohms, and  $T$  is the temperature in °C (Geokon, 2005)

The CR5000 dataloggers's software, PC9000, is capable of writing simple programs that are able to easily convert the frequency of the vibrating wire strain gage to both a strain and a temperature. However, the CR5000 datalogger does not have the capability of directly reading the frequency signals and therefore an interface must be used. When working with the CR5000 the most common interface to use is the AVW1 Vibrating Wire Interface, which was used on this project. Figure 3-12 shows the AVW1 interface.



**Figure 3-12 AVW1 Vibrating Wire Interface**

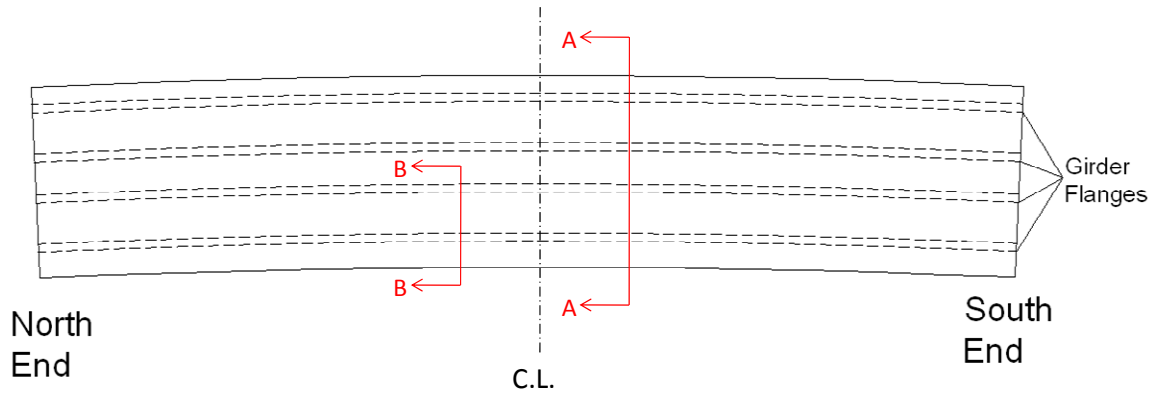
The AVW1 interface supplies frequency signal conditioning that: completes the thermistor bridge needed to measure temperatures accurately, convert the swept frequency excitation to a workable value, reduces noise for the vibrating wire signal, and provides additional protection for the temperature and vibrating wire circuits (Campbell, 1992). A single vibrating wire strain gage can be attached to an AVW1 interface, which can then be connected to the CR5000 datalogger. When working with AM416 multiplexers and numerous vibrating wire strain gages a single interface can be used with each multiplexer. This method proves advantageous over resistive strain gages because

of the low number of interfaces required as opposed to the high number of input modules (completion resistors) required for resistive strain gages. However, one of the main disadvantages of vibrating wire strain gages are their high price as opposed to typical resistive strain gages. In addition, results on this research project have shown that the gages are quite sensitive to thermal effects – particularly with direct exposure to the sunlight.

### **3.5 Sensor Locations on the Bridge**

Due to the number of individual research projects associated with the bridge specimen, an instrumentation plan was needed to suit the needs of all objectives. One of the main concerns was the issue of the blast-testing project. Since one of the girders was going to be subjected to an explosive blast, storing the data acquisition units and corresponding components inside the girders was not an option. Therefore, all data acquisition units and components were located in a storage unit that was assembled on a location that would provide shield from the blast. The storage unit was located at the south end of the bridge system and was protected from the blast by the southern pier. All wiring from the numerous types of gages was extended from the original gage locations to the storage unit. Although several gages were installed on various sections of the bridge specimen, not all of the data that was gathered pertained to the study reported in this thesis.

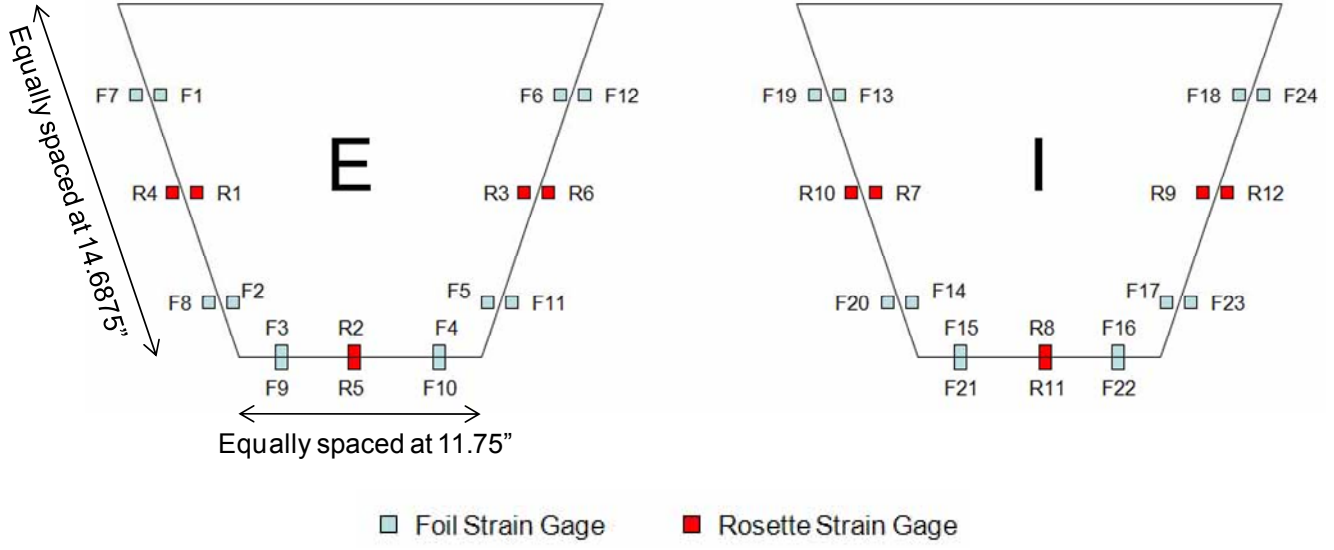
Two regions of the bridges were instrumented for this project. Figure 3-13 shows the locations of the two instrumented sections on the twin girder system. Sections A-A and B-B are both located on the two bridge girders.



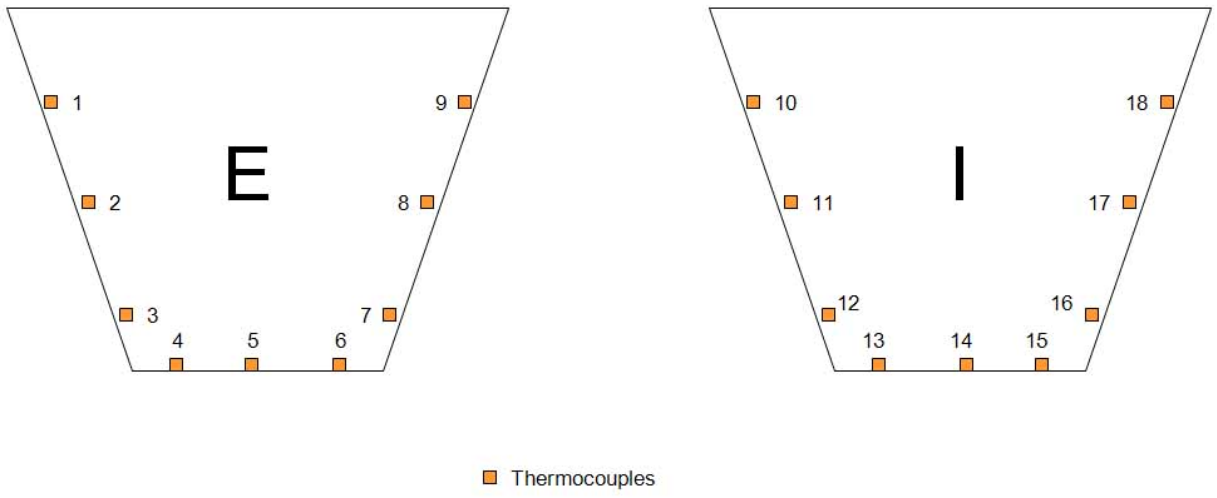
**Figure 3-13 Section Locations for Instrumentation**

Section A-A (known as Section A from here on out) is located 72 inches south of the center line and extends through both the interior (western) and exterior (eastern) girders. Section B-B (known as Section B from here on out) is located 70 inches north of the center line and is only located on the interior girder. These locations were chosen because of their relative close distance to the centerline while still maintaining some distance from the blast-test location (midspan centerline). Section B was only instrumented on the interior girder because the exterior girder was to be fractured with the blast test and would produce stresses in the interior girder that would later be studied on another project.

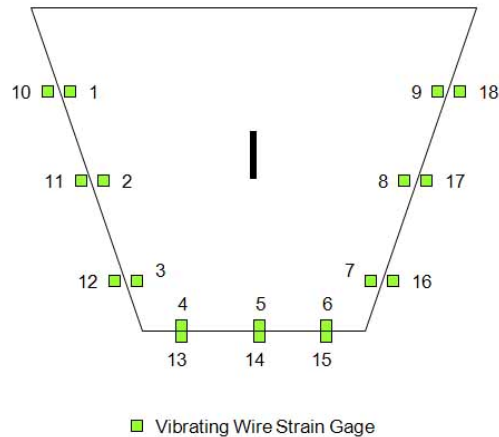
Section A was the primary location for data on this project and contained 24 foil strain gages, 12 rosette foil strain gages, 18 vibrating wire strain gages, and 18 thermocouples. Figure 3-14, Figure 3-15, and Figure 3-16 show the different cross-sections of section location A. The spacing for all gages on the main section was constant throughout the cross-section.



**Figure 3-14 Section A Foil and Rosette Locations**



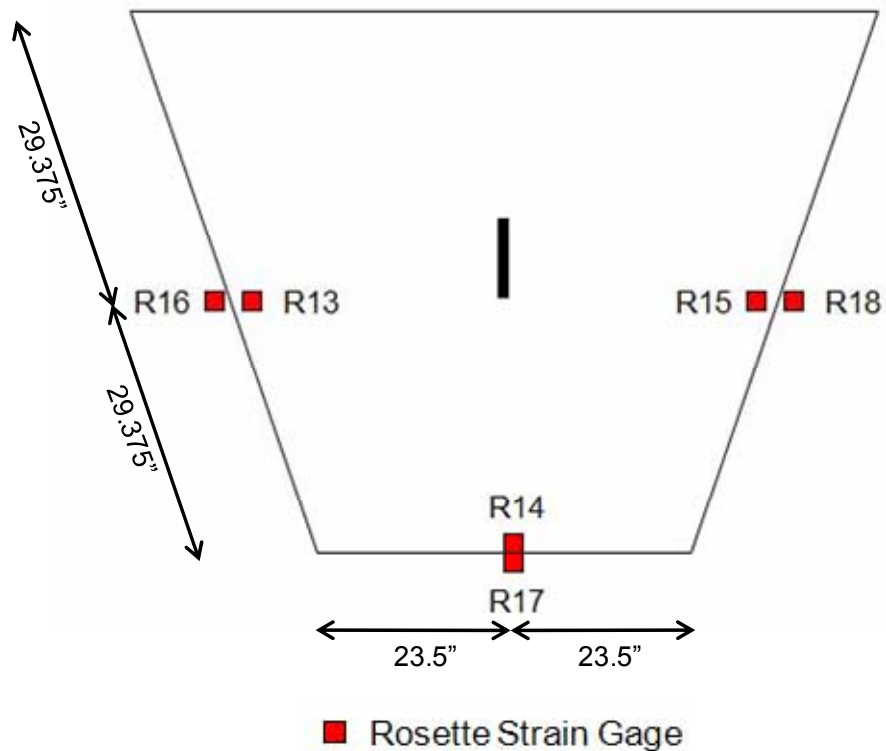
**Figure 3-15 Section A Thermocouple Locations**



**Figure 3-16 Section A Vibrating Wire Strain Gage Locations**

Section A included 4 types of sensors that were monitored throughout the study. Thermocouples at the locations provided temperature measurements, whereas the other gages provided strain measurements. Wires from each gage on the interior of the girders were extended to the southern end of the bridge along the inner chambers of the girder. Wires from each gage located on the exterior surface of the girder were extended to the southern end of the bridge along the outer edges of the bottom flanges of the girders. Clamps and wire ties were used to support the wires along the bridge length.

Section B contained 6 rosette strain gages and was primarily instrumented to monitor changes to the interior girder during and after the blast loading. Although these gages were primarily installed for the blast loading, data was still recorded and analyzed during the construction and live loading phases. Measurements were recorded to later be compared to the section A measurements. Figure 3-17 shows a cross-section of section B.



**Figure 3-17 Section B Rosette Strain Gage Locations**

As previously stated, the data acquisition system and its corresponding components were all housed in a storage unit near the south pier. In total, the storage unit housed three CR5000 dataloggers and eleven AM416 multiplexers to gather and store data for this particular study. Additional multiplexers and gages were maintained and monitored for other projects associated with the bridge specimen. The storage unit also housed 2 auto-marine 12V batteries that provided power to the CR5000 dataloggers. The storage unit proved to be an essential item in organization and planning since it enabled the entire project to be monitored from a single, protected, and easily accessible location. Table 3-3 details a more thorough explanation of the components utilized in the study.

**Table 3-3 Data Acquisition System and Components**

<b>Datalogger Label</b>	<b>Multiplexer Label</b>	<b>Contents</b>
1	J	18 thermocouples
1	R	10 foil gages
1	S	10 foil gages
1	H	12 foil gages
1	C	5 rosette gages
2	K	12 foil gages
2	A	5 rosette gages
2	B	5 rosette gages
2	D	3 rosette gages
3	Y	10 vibrating wire gages
3	Z	10 vibrating wire gages

A large number of sensors and data acquisition components were utilized in the various projects studying the twin girder system. Although each of the projects obtained measurements from different gages; many of the gages provided data to multiple studies. Therefore, a well planned organized structure was needed to ensure an efficient method of data acquisition. Each gage, multiplexer, and datalogger was labeled and recorded with a specific labeling format. Master files that provided a detailed overview of every component were then created and distributed to all persons working in correlation with the bridge girders.

### **3.6 Datalogger Programming**

The CR5000 dataloggers used needed to be capable of reading and storing data for numerous gages. As outlined in the last section, several different sensors were monitored throughout the bridge system. The gages were spread out over eleven multiplexers that were dispersed among three CR5000 dataloggers. Each datalogger was programmed specifically for the multiplexers and gages assigned to it. Predetermined time intervals were also inserted into the programming so that the dataloggers were triggered to take measurements at specific time intervals throughout the duration of the project. This time interval could easily be altered in the programming and changed during different phases of the project. The dataloggers were able to store the data received onto memory cards which were then linked to a personal computer. The data could then easily be downloaded and analyzed from the remotely instead of onsite. The data included temperature values from the thermocouples, strain values from both foil and rosette strain gages, temperature and strain values from the vibrating wire strain gages, and timestamps providing the time for each data point received.

Programming of the datalogger required proper planning and organization of all aspects of the project before final programs could be written. Programs were written based on an algorithm produced by a previous graduate student (Arakan, 2005). The simple algorithm includes variable and table definitions, scans of each multiplexer and final data tables based on measurements received. The complete programs used in this project are provided in Appendix A.

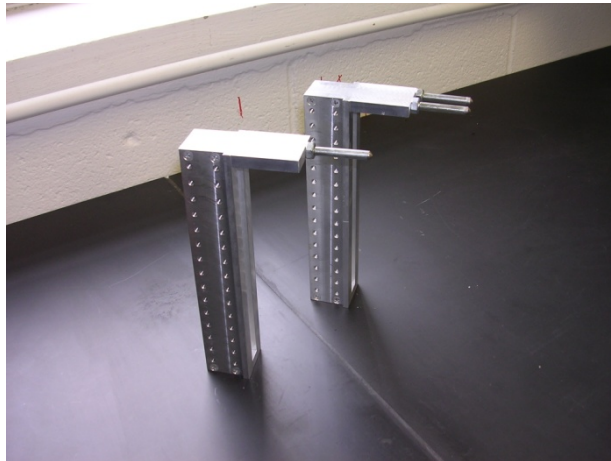
### **3.7 Linear Potentiometer Displacement Gage**

The webs and bottom flanges of the girders were subjected to stresses during the removal of the girders from their original location, transportation, and erecting of the



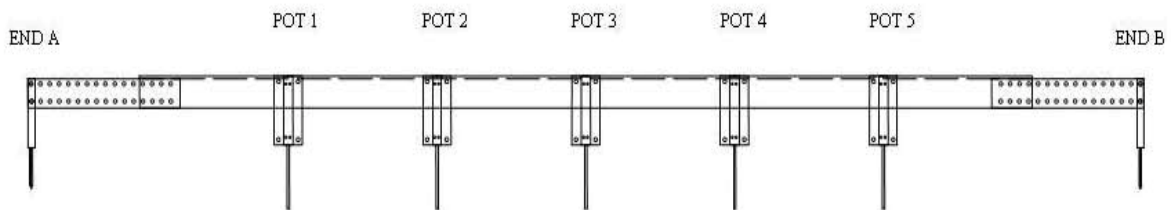
system at the Ferguson Structural Engineering Laboratory. After the girders were erected into their final positions at FSEL, initial plate imperfections were measured. These initial imperfections served as a reference for future deformations. Plate deformations were expected to occur due to the planned construction phases, primarily after the concrete deck was cast. Subsequent readings were taken after the supporting form brackets were removed.

Readings of the plate imperfections and deformations were made using the Linear Potentiometer Displacement Gage (LPDG) developed by Mercan, 2005. The LPDG is composed of a main aluminum channel section, five linear potentiometers, and two adjustable aluminum end caps. The linear potentiometers are equally spaced along the main aluminum channel, enabling the device to simultaneously measure and record the out of flatness at five locations along the plate. This setup is useful because the LPDG provides a measure the profile of a web or flange plate at a certain location simultaneously. Because there are a variety of girder depths and bottom flange widths, the LPDG was designed to be flexible in accommodating these variables. Figure 3-18 shows a picture of the end caps separate from the main channel. The end caps are machined sections roughly 8 inches in length with a grid of connection holes drilled at  $\frac{1}{2}$  inch increments along their lengths. Thus, when connected to the main channel section, screws can be used to connect and adjust the end caps position on the main channel. This enables the researcher to vary the total length of the LPDG according the project's needs. On the underside of the ends of the end caps are machined end tips that act as support legs forming a tripod that balances the overall device when used.



**Figure 3-18 End Caps**

It should be noted that different length main channel sections were also used. The geometry of bridge girders can significantly vary, and when initially designed, the LPDG was to be used for any type of girder regardless of size. In this project, researchers used 2 separate main channels. The C 1 ½ x 1 ½ x 1/8 aluminum channels were 2.67 and 4 feet in length. The smaller channel section was used for the bottom flange measurements, while the larger was used for the web plates. Figure 3-19 shows the LPDG and its components.



**Figure 3-19 Linear Potentiometer Displacement Gage (Mercan, 2005)**

As previously stated, adjusting the connection holes between the end caps and the main channel section allows 0.5 in. adjustments in the device length. Table 3-4 shows the range of device lengths possible.

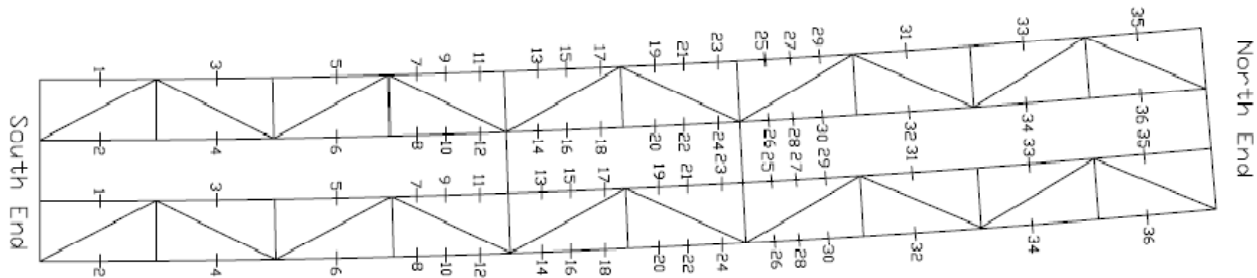
**Table 3-4 Usable Lengths of Different Main Channel Sections**

Channel Length (ft)	Channel Length (in)	Usable Device Length	
		Minimum (in)	Maximum(in)
2.667	32	33.5	45.5
4	48	49.5	62

The CR5000 datalogger was used in conjunction with the LPDG to measure and record data. The CR5000 was the optimal choice of data acquisition due to its light weight and portable ability. A cable length of approximately 20 feet connected the device to the LPDG which provided generous freedom of mobility. A switch mechanism was used to trigger datalogger to take readings. The datalogger was programmed to take readings from the linear potentiometers when the switch was engaged. Data was stored in the CR5000 and was manually retrieved when the desired measurements were recorded.

A 1 ½ inch-square aluminum bar, 10 feet in length, was calibrated as a reference surface as outlined in Mercan, 2005. Imperfections in the bar were calibrated with the LPDG using the bed of a machinist’s lathe. Before any measurements were taken on the girder specimens, measurements on the reference bar were taken to provide a zero reading for comparisons with the plate measurements. All girder webs and bottom flanges were measured on both girders during different phases throughout the

construction. Web and flange imperfections were first measured immediately after erection prior to any other construction activity. Measurements were then taken after the concrete deck had been cast, followed by final measurement after form brackets had been removed. Each girder is comprised of 10 segments, each roughly 12 feet in length. Measurements were taken on the 3 north segments, as well as the 3 south segments only at midspan of the segment, or roughly 6 feet. The middle 4 segments were divided into quarters and measurements were taken at each quarter, as shown in Figure 3-20. The same spacing guidelines were used for web and flange measurements on both girders.



**Figure 3-20 Locations of Web Imperfection Measurements**

Each phase of the measuring began with zero readings taken using the reference bar. The process required two researchers to take readings, one researcher operating the datalogger and the switch, while the other researcher manually controlled the LPDG. The person operating the CR5000 could monitor the field readings for errors using the LCD display, and carried a clipboard with schematics in case special notes needed to be recorded during the measuring process. Three measurement readings were taken at each location to ensure accuracy in the readings. The linear potentiometers had spring returns so that the plungers in the instruments returned to the same position when the LPDG was not engaged on a plate. The process of plate measurements began by aligning the LPDG

at the desired location and firmly pressing down on the entire apparatus engaging the linear potentiometers until the three support points rested on the plate. The switch on the datalogger was then activated to take a reading of the plate imperfection. The LPDG was then removed from the plate and the process was repeated until three readings were taken at each location. If there was a malfunction in the placement of the LPDG, a note was made in the manual log that was taken during the reading process and an additional reading was taken so that three readings were recorded. Figure 3-21 and Figure 3-22 depict two researchers operating the LPDG in the field on both web and flange plates. Results regarding imperfections are discussed in Chapter 5.



**Figure 3-21 Measuring Web Imperfections (Mercan, 2005)**



**Figure 3-22 Measuring Bottom Flange Imperfections (Mercan, 2005)**

## CHAPTER 4

### Girder Stresses during Construction and Live Loading

#### 4.1 Introduction

The previous chapter provided an outline of the instrumentation and techniques that were used in the field measurements. This chapter will present the data from the measurements on the girder cross-sections during casting of the concrete deck as well as subsequent simulated live loading. Readings from the strain gages were converted to stresses using Hooke's Law. The stress changes in the instrumented members are also compared to finite element analysis (FEA) that were conducted by the another graduate student working on the study (Quan Chen). The results from these field measurements provide a good indication on how steel twin box girder systems behave during the construction and loading processes. The chapter will first discuss the results of the steel box girders during the different construction phases, as well as the live loading scenarios. Comparisons between the measured results and FEA predictions are then discussed.

#### 4.2 Steel Trapezoidal Box Girders

The twin steel trapezoidal box girders were erected onto the concrete piers in January of 2006. Solid plate end diaphragms were installed at the ends of the bridge to control twist of the slightly curved girders. The girders were instrumented between May and July of 2006. As outlined in the last section, the instrumentation consisted of a total of 100 sensors (82 strain gages and 18 temperature gages) (see Table 3-3). By early August 2006, the data acquisition system was functioning and recording data. Data was

recorded every 30 minutes, until late September 2006, when the sensors were switched to a high-speed data acquisition system. Once on the new system, data was recorded until the end of October 2006. Data acquisition units ran for a period of time that enabled them to monitor all construction and live load testing phases. The data measured during construction and live loading provided insight into how the system reacted to induced stresses. Although data was recorded over a relatively long period of time, there were a few key milestones that were of primary interest for this research project. Strain and stress changes were evaluated for the following time periods:

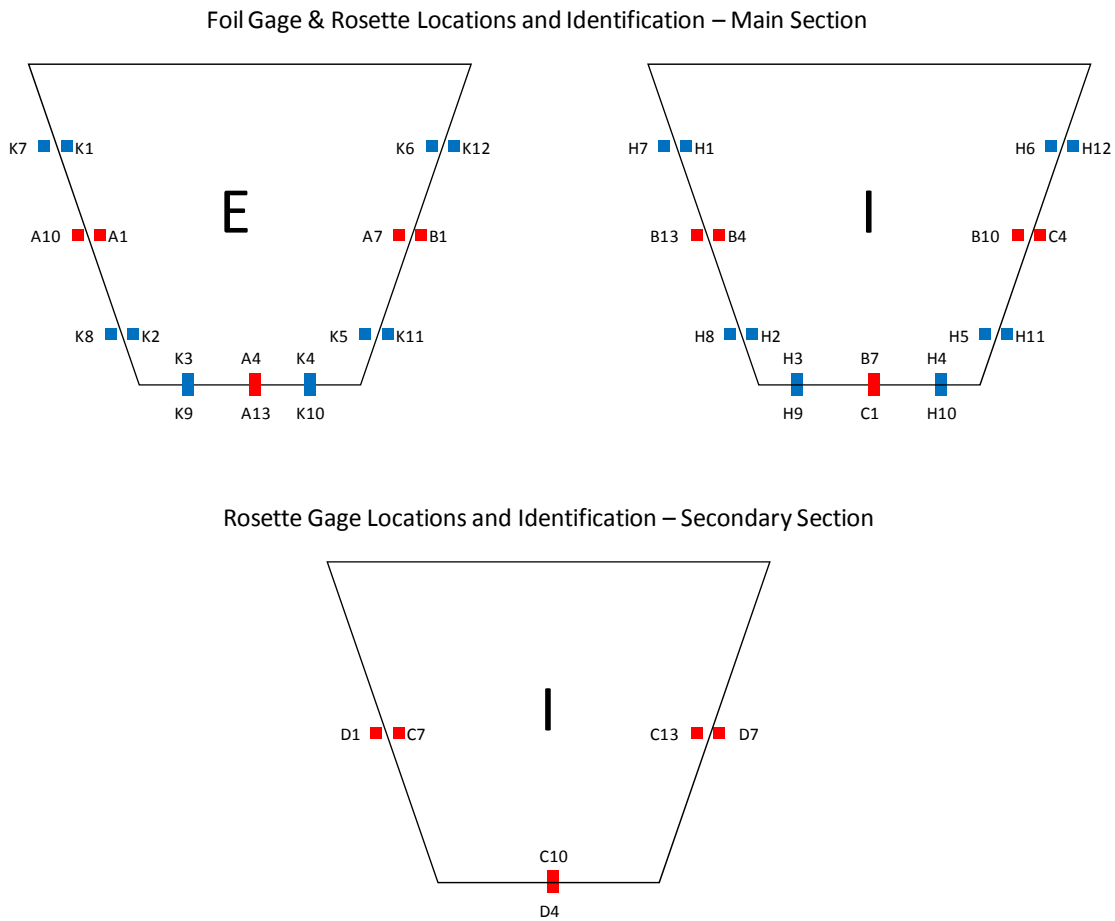
- Before and after the pouring of the concrete deck
- Before and after the pouring of the west concrete deck rail
- Before and after the pouring of the east concrete deck rail
- Before and after the simulated live load testing (3 different load positions)

#### **4.2.1 Stress Changes due to Concrete Deck Construction**

The data presented in this section represents the stress changes due to the casting of the concrete deck and rails on the girder bridge system. The entire construction process was monitored and documented with photos. The weight of the deck and the rails totaled approximately 380 kips of applied load. The effects of daily thermal cycles can cause large stress gradients on steel bridge girders. To minimize the thermal effects and obtain a measure of the stress changes due to construction activity, strain gage data recorded in the early morning (midnight-5 am) time period were chosen for study. Since temperature reading devices were installed at numerous locations alongside foil gages, the ideal time (according to temperature) for a strain reading could be located. Figure 4-1 shows the locations of the strain gages from which the readings are presented and



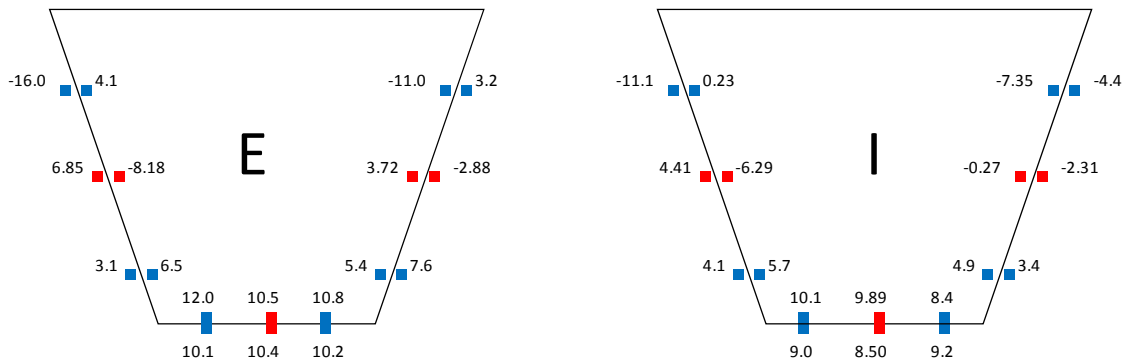
discussed in this section. The box girders were instrumented at a main cross-section (Section A) and at a secondary section (Section B) (see Figure 3-13, Figure 3-14 and Figure 3-17 for dimensions).



**Figure 4-1 Strain Gage Locations and Labels**

An initial stress value was chosen at 0:00 on August 17, 2006, while the pouring of the concrete deck began at 7:30 on August 17, 2006. Pouring of the deck started on the north end and ended at approximately 13:30. A final stress value at 4:00 on August 18, 2006 was chosen as the end of the time cycle due to a similar ambient temperature as

the initial night before. Because both stress values were taken in the early morning period, the values were less likely influenced by temperature, and solely based on the load of the concrete deck that was applied. Figure 4-2 shows the change in stress values at Section A due to the casting of the concrete deck. As denoted, negative values represent compressive stresses, and positive values represent tensile stresses. All numerical values provided in figures in this section have units of kips per square inch (ksi). Rosette strain gages are marked as red boxes, while foil strain gages are marked as blue boxes. Figure 4-2 shows the girder stresses during casting of the concrete deck and as expected the gravity loading created compressive stresses at the top of the web elements and tensile stresses on the lower elements. A comparison of the stresses on either side of the web plates shows that a significant amount of plate bending occurred as evidenced by the large difference between the respective gage readings.



**Figure 4-2 Stress Changes due to Casting of Deck (ksi) Section A**

The large plate bending effects occurred due to the relatively large out-of-flatness in the web plates that existed in the erected girder. The imperfections will be discussed in detail in Chapter 5. To eliminate the effects of plate bending, two strain gages were placed at each location of interest; one on the interior of the girder, and one on the

exterior of the girder. This can be seen in any of the figures presented in this section. The effects of plate bending can be accounted for by averaging the gage readings on opposing sides of the plate, which eliminates plate bending and therefore captures axial components of the stress. The assumption is made that that bending will remain elastic and the strain distribution is linear. When converted to a stress value, the bending strain value accurately portrays stress from bending theory given by the following equation:

$$\sigma = \frac{Mc}{I} \quad (4.1)$$

Validation of this process can be seen in Figure 4-3. For the validation experiment, a steel plate was instrumented with two foil strain gages and tested. It is evident that the average strain and stress values presented are similar to the theoretical values calculated (Arakan, 2005).

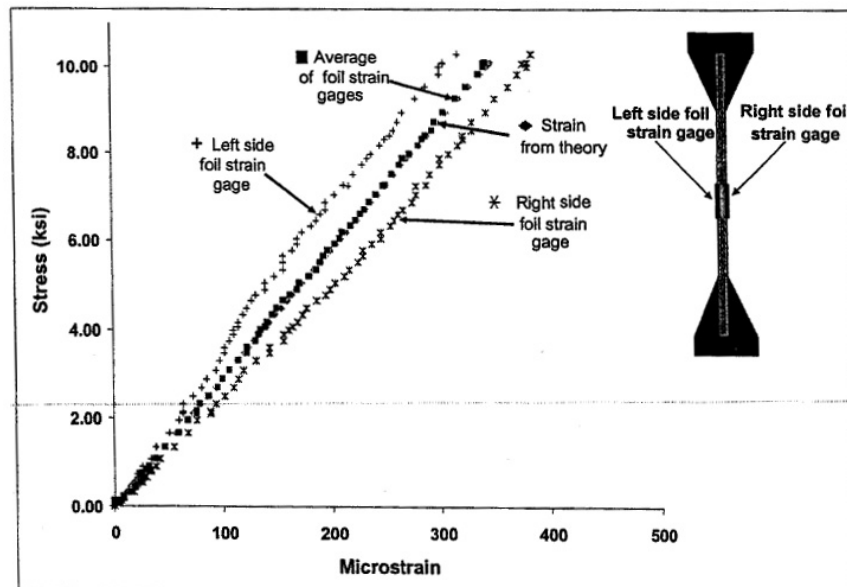
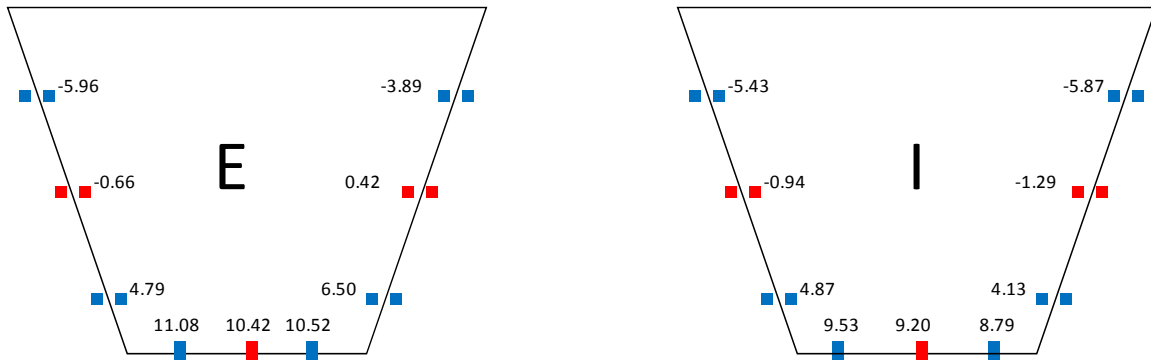


Figure 4-3 Validation of Foil Strain Gages (Arakan, 2005)

To accommodate the effects of plate bending in the research performed, stress values at each location instrumented were averaged and plotted to indicate the true bending stress. Figure 4-4 shows the average change in stress values at Section A due to the casting of the concrete deck. The values shown in Figure 4-4 are the averages from the corresponding gage readings shown in Figure 4-3.



**Figure 4-4 Average Stress Changes due to Casting of Deck (ksi) Section A**

While in most cases the average stress readings are of interest, on this project the effects of the plate bending are also of interest. The measurements provide data that can be used in finite element analysis to compare measured plate bending with predicted values.

As seen, the top portions of the webs exhibit compressive stresses due to the casting of the concrete deck. At roughly mid-height of the webs, compressive stresses still exist but have decreased in magnitude. The magnitude values are closer to zero because the gage locations are closer to the neutral axis, where bending stresses are minimal. From the figure, it can also be seen that the bottom flanges experience large tensile stresses in both girders. Proper monitoring of data was performed during the construction phases to ensure values were in the correct range of expected values. Figure 4-5, Figure 4-6, and Figure 4-7 present stress values exerted during the casting of the

concrete deck at single locations along the exterior web of the exterior girder. The graphs show the stress levels as a function of the time period in which the casting took place. It can be seen that stress levels started to change significantly at 7:30 when the concrete placement began. The rapid increase between 8:30 and 9:30 was due to the weight of the weight of the wet concrete and the screed that was used to finish the surface. Between 9:00 and 9:20 the screed was directly over the main section of the girders that were instrumented. Average stress values are graphed to show values that negate the plate bending effects. It should also be noted that the some of the stress changes are likely due to temperature effects. During the pouring of the concrete deck, the ambient temperature changed however the sunlight exposure also changed as the sun rose in the sky during the concrete placement. Additional thermal effects can also happen due heat of hydration during the concrete curing. The combined effects from the temperature led to variability in the gage readings even after the concrete placement finished. However the stress readings tended to level out after the sun set and the bridge temperature normalized during the night.

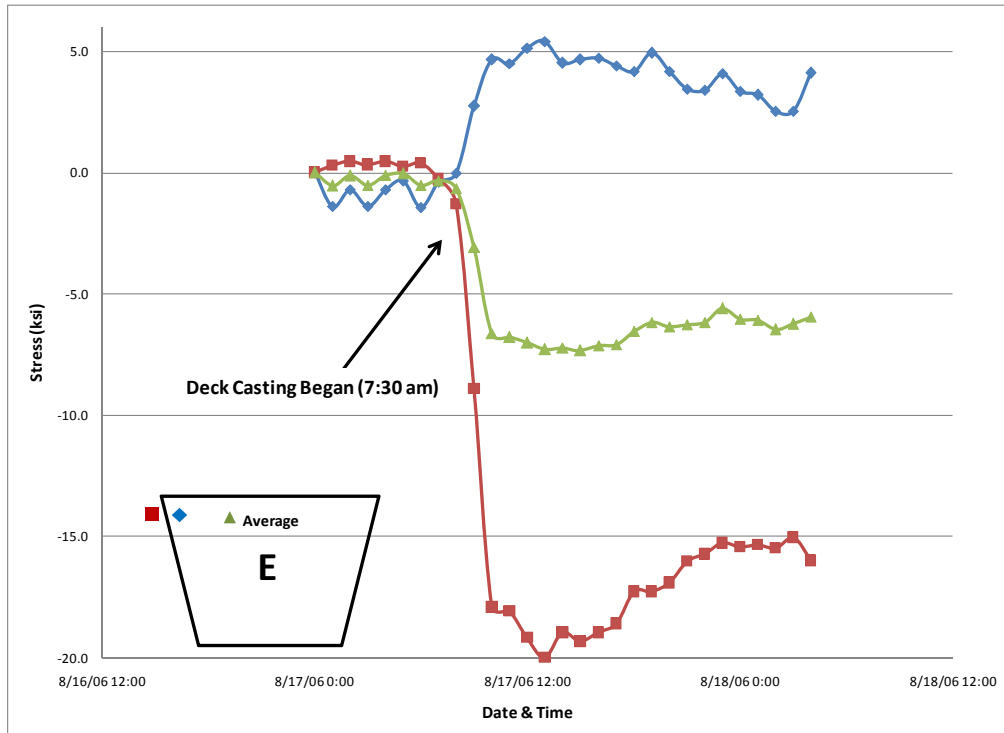


Figure 4-5 Stress Development during Deck Casting – Top of Web

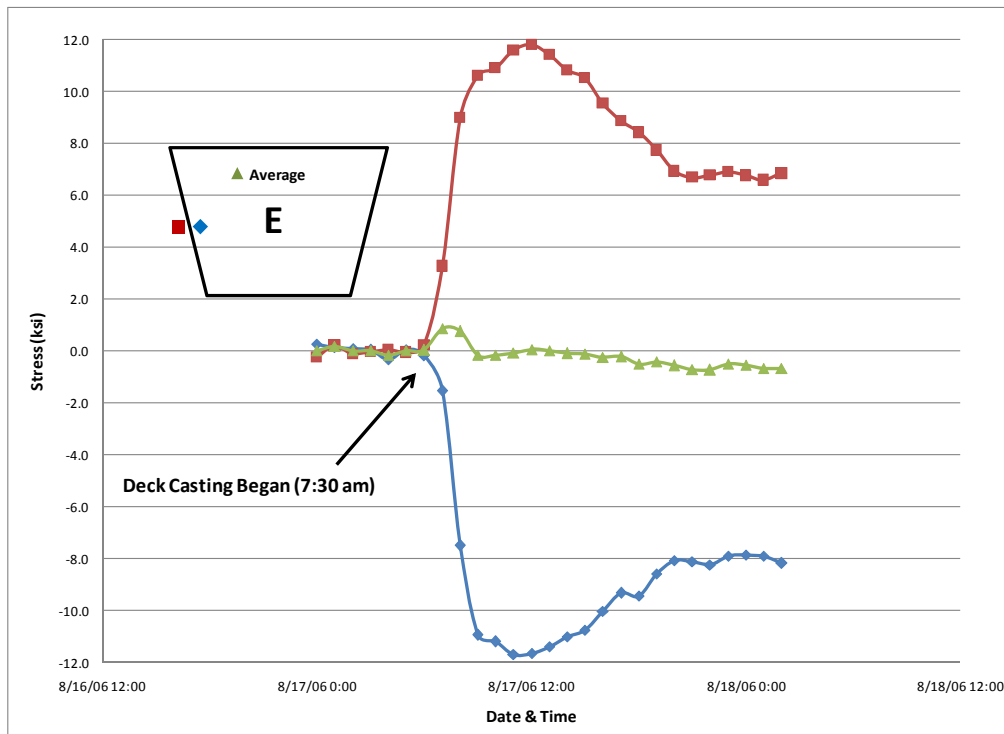
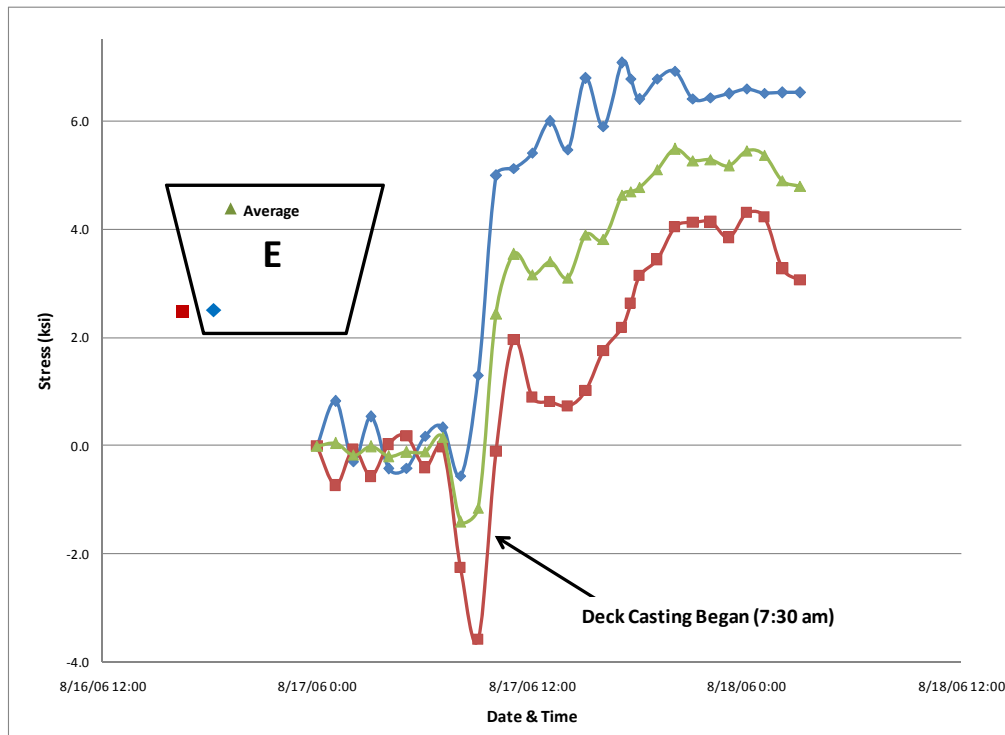
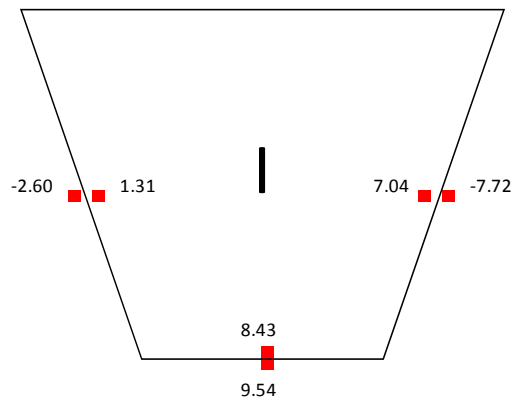


Figure 4-6 Stress Development during Deck Casting – Mid-Height of Web



**Figure 4-7 Stress Development during Deck Casting – Bottom of Web**

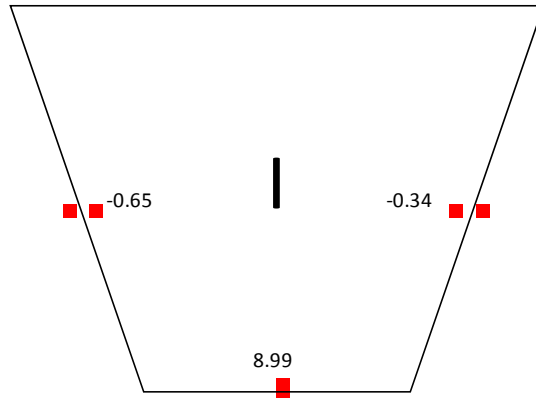
In addition to Section A being instrumented on the girders, Section B was also instrumented on the interior girder as shown in Figure 3-13. Stresses were also monitored at Section B during the casting of the concrete deck. The same time frame was monitored as Section A of the girders. Results are presented in Figure 4-8.



**Figure 4-8 Stress Changes due to Casting of Deck (ksi) Section B**

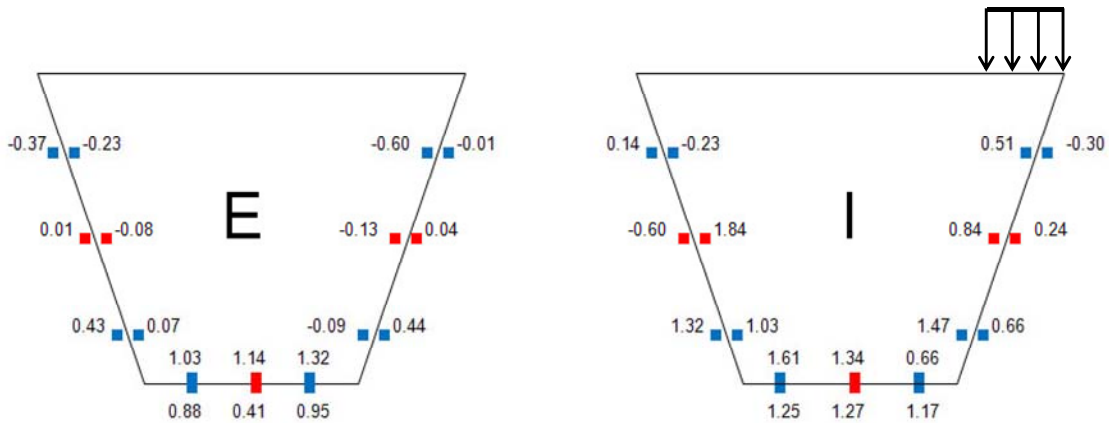
Stresses built up in the webs differ from the web stresses at Section A on the girders. The interior web exhibits stresses that are lower in magnitude than the interior web location on Section A, whereas the magnitudes in the exterior web are larger at Section B than at Section A. The likely explanation for this difference is due to the different initial imperfections of the web plate elements at different locations along the girder. The tensile stresses in the bottom flange elements at both locations are similar in magnitude. Figure 4-9 shows the average stresses located in at Section B. Comparing the average stresses back to Figure 4-4, the comparison stresses between Sections A and B are -0.94 and -0.65 on the interior webs and -1.29 and -0.34 on the exterior webs. While the readings between the two sections are similar the difference on the exterior web is a little larger. It should be noted that form brackets were located along the exterior webs of both girders during construction. Since the form brackets were placed along the entire girder lengths, it is possible that bracket position in regard to Section A and B gages might have differed. Although gage averaging is intended to remove the effects of plate bending, the large force from the overhang brackets may have some additional local effects that affected the readings more at Section B compared to Section A. In any event, the readings between the two sections are relatively close to one another.





**Figure 4-9 Average Stress Changes due to Casting of Deck (ksi) Section B**

The casting of the concrete deck was begun and completed on August 17, 2006. The casting of the west concrete rail took place five days later on August 22, 2006. The initial stress value was measured at 0:00 on August 22, 2006. Actual casting of the west rail began at 8:30 and was completed within a couple of hours. The final stress value was measured at 22:00 on August 23, 2006. This time was chosen because of the similar ambient temperature to the initial time reading. Figure 4-10 shows the change in stress values at Section A of the girders due to the casting of the west concrete rail.



**Figure 4-10 Stress Changes due to West Rail (ksi) Section A**

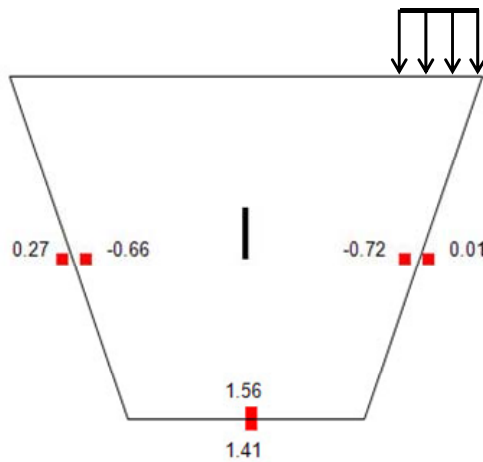
As seen in Figure 4-10, the casting of the west rail created relatively minimal stresses in the girders. Stress changes were expected to be smaller in magnitude due to the nature of the deck member being poured. The self weight of the west rail was approximately 16% of the concrete deck. The smaller weight of the rail is evident in the much smaller stresses that were measured compared to those during concrete casting. Most of the stress changes were under 1 ksi with the exception of the bottom flanges and the bottom portions of the interior girder's webs. Although the West rail was positioned on the left side of the bridge shown in Figure 4-10, both girders experienced stress changes that were similar in magnitude. This is further demonstrated in Figure 4-11 which shows the average stress changes at Section A due to the casting of the west rail. Although the stress change magnitudes are a little larger on interior girder, some of the gage readings on the exterior girders had values relatively close in magnitude. It is interesting to note that nearly all of the gages on the interior girder experience tension, which is probably due to the position of the neutral axis of the composite section, which is near the top flange of the steel section. The average stresses on the exterior girder are a mixture of tension and compression which probably result from the slight torsional effect loading the West end of the bridge would have on girder E. In general the stress changes were relatively small compared to those measured during concrete casting.

As presented in the casting of the concrete deck, measurements were recorded and graphed at a secondary location for the casting of the west rail. Much like the results of the casting of the concrete deck, the comparison of the interior girders at both locations in response to the casting of the west rail is somewhat similar. Figure 4-12 and Figure 4-13 present the actual and average stress change values at Section B in relation to the casting of the west rail, respectively. It is not clear why the sign of the web rosette readings are opposite of those shown for Section A in Figure 4-11. Due to the relatively small stress

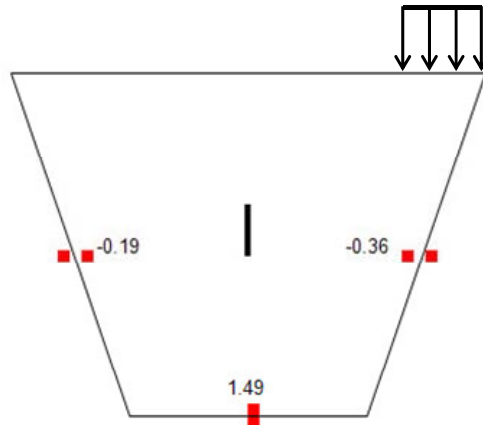
magnitude, the difference is not a major concern. The bottom flange stresses are relatively similar for the two locations. Graphs monitoring stress values at single locations throughout the construction of the west rail are provided in Appendix B.



**Figure 4-11 Average Stress Changes due to West Rail (ksi) Section A**



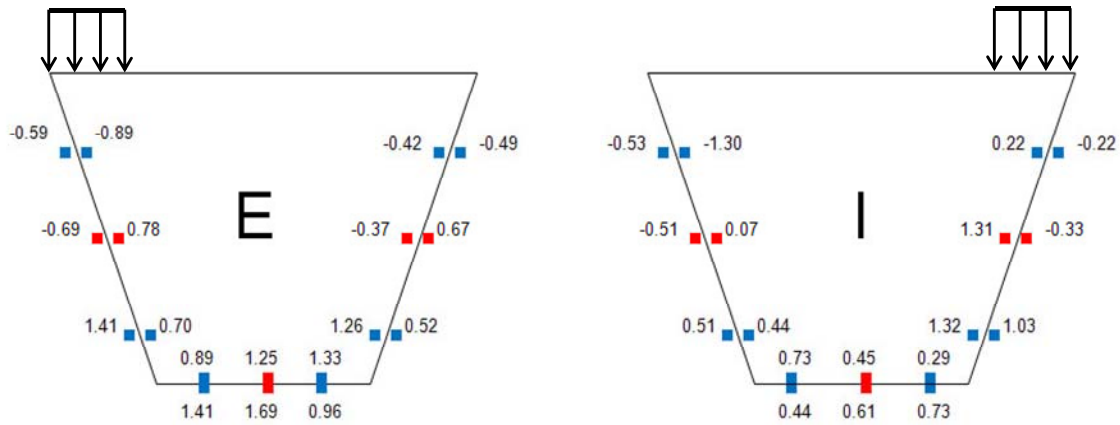
**Figure 4-12 Stress Changes due to West Rail (ksi) Section B**



**Figure 4-13 Average Stress Changes due to West Rail (ksi) Section B**

The casting of the west rail was completed the day it began on August 22, 2006. The casting of the east concrete rail took place two days later on August 24, 2006. The initial stress value was measured at 0:00 on August 24, 2006. Actual casting of the east rail began at 8:30 and was completed within a couple of hours. The final stress value was measured at 1:00 on August 25, 2006 due to the relative similar ambient temperature as the initial time reading. Figure 4-14 shows the change in stress values at Section A of the girders due to the casting of the east concrete rail.

The stress changes during casting of the east rail are shown in Figure 4-14 with the averaged strain gage readings given in Figure 4-15. The stress magnitudes were similar to those observed for the casting of the west rail. From the average stress readings, the neutral axis appears to be located between the top gages and the strain rosettes. The distributions of the stresses differ from what was observed during casting of the west rail where nearly all of the gage readings were in tension for the girder closest to the rail.



**Figure 4-14 Stress Changes due to East Rail (ksi) Section A**

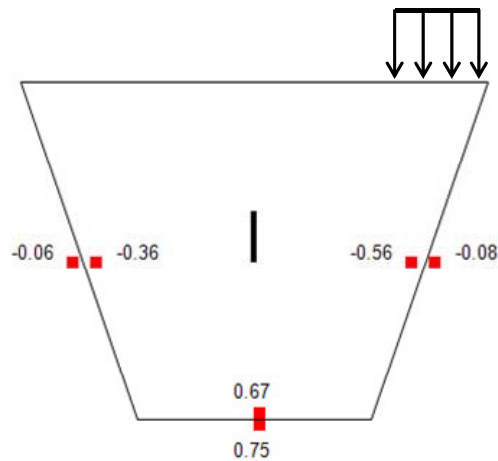


**Figure 4-15 Average Stress Changes due to East Rail (ksi) Section A**

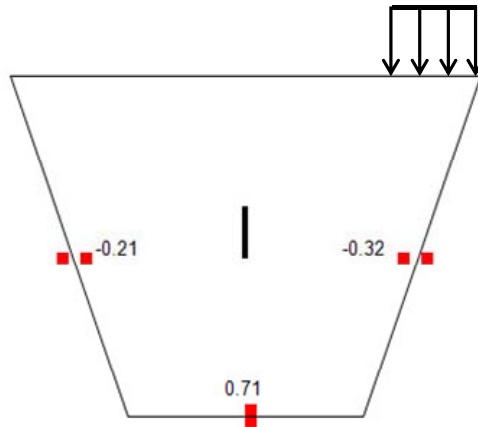
The change in the stress distribution may be caused by the stiffening on the interior side of the bridge caused by the previously cast west rail. This would explain the smaller stresses caused on the interior girder (Figure 4-15, 0.59 ksi maximum bottom flange stress) during casting of the east rail when compared to the stresses in the exterior girder during casting of the west rail (Figure 4-11, 1.14 ksi maximum bottom flange stress). Although the distribution differs, the magnitudes of the stress changes are very

similar for the two different bridge rails. In both cases the stress changes were relatively small.

As presented in the casting of the concrete deck and the west rail, measurements were recorded and graphed at Section B for the casting of the east rail. Similar to the west rail, the comparison of the interior girder stress changes at both locations in response to the casting of the west rail is very similar. Figure 4-16 and Figure 4-17 present the actual and average stress change values at Section B in relation to the casting of the east rail. When compared to Figure 4-14 and Figure 4-15, the values are almost identical. Graphs monitoring stress values at single locations throughout the construction of the east rail are provided in Appendix B.



**Figure 4-16 Stress Changes due to East Rail (ksi) Section B**



**Figure 4-17 Average Stress Changes due to East Rail (ksi) Section B**

#### **4.2.2 Stress Changes due to Live Load Testing**

The primary purpose of testing the twin box girder system was to study the redundancy of the system if one of the girders were fractured. To simulate the type of loading such a bridge would be subjected to in-service; loading simulating and HS-20 truck was placed on the bridge. Although the strain gage readings could have been monitored using the Campbell Scientific dataloggers, these systems were not going to be used during the final fracture tests on the girders. Instead a high-speed data acquisition system was to be utilized during the final tests. To ensure that the instrumentation was configured correctly, all strain reading devices were switched over to a high-speed data acquisition system two weeks prior to the blast test. Therefore all data under the simulated truck loading was gathered with the high-speed system, which was capable of sampling at a rate of 500 readings per second. This high speed was not necessary for the scope of this project and even though the system recorded strain readings every 5 seconds during the live load testing, readings were only analyzed every 60 seconds.

The simulated HS-20 truck was positioned for maximize moment and torsion in the girders as per AASHTO guidelines. The truck axle spacing was 14 feet for both the front and rear axles. The front axle was represented with a concrete block with dimensions 2 ft. W x 3.33 ft. H x 7.33 ft. L. Five steel plates, with dimensions 1.5 ft. W x 0.167 ft. H x 1.67 ft. L, were then bolted together and placed on top of the concrete block as shown in Figure 4-18. The truck mid and rear axle weights were simulated using AASHTO Type IV prestressed concrete beams that were available at the Ferguson lab from a previous research investigation (Figure 4-19). The entire live load simulation weighed 76 kips and is shown positioned on the bridge system in Figure 4-20.



**Figure 4-18 Live Load Simulation - Front Axle**





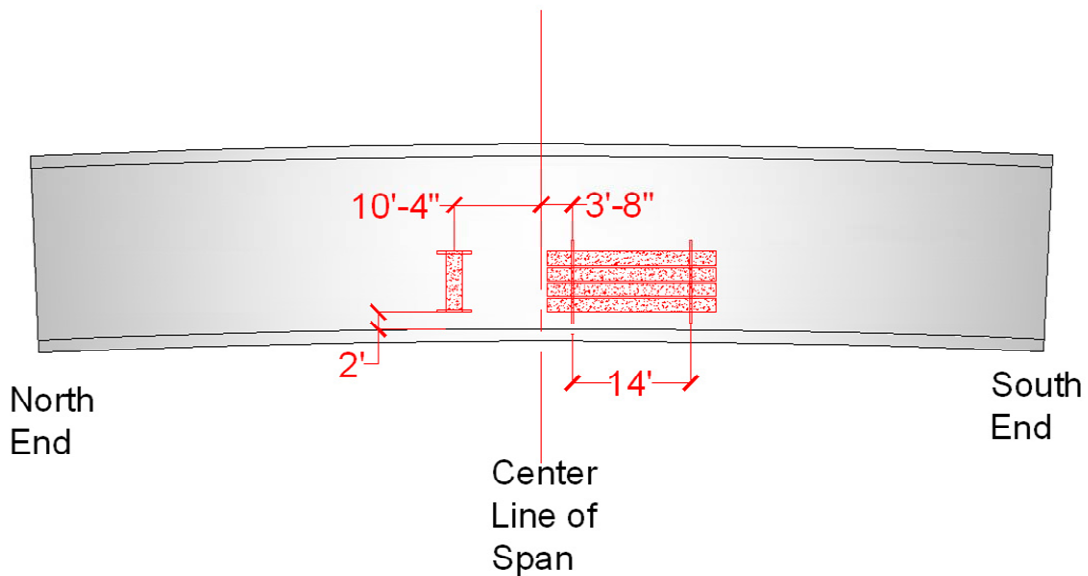
**Figure 4-19 Live Load Simulation - Rear Axle**



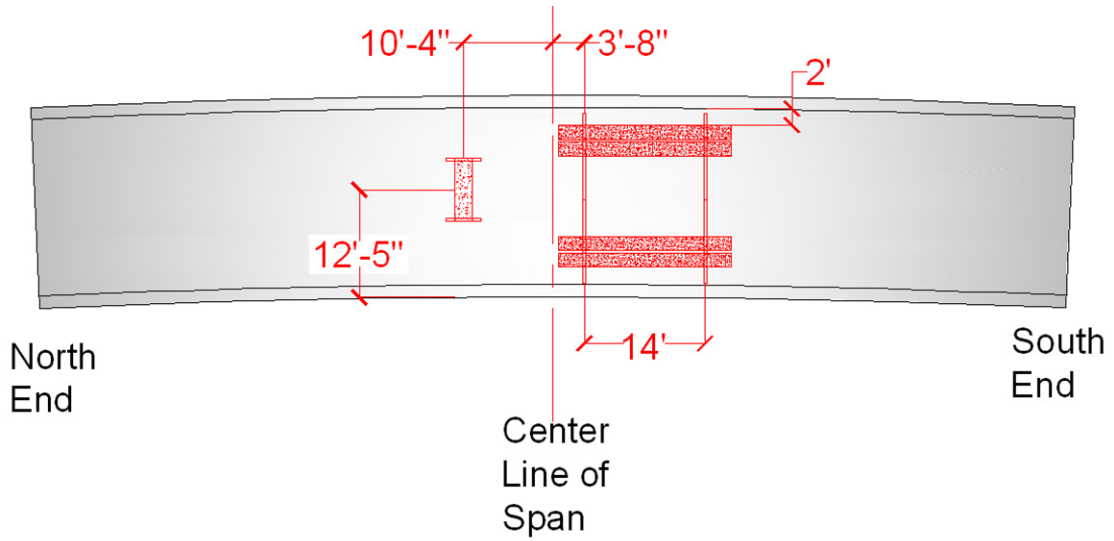
**Figure 4-20 Live Load Simulation - Full View**

The live load test was performed by placing the simulated truck in three different positions on the bridge deck to see how the system would react. During each position, data was recorded once every 5 seconds as previously stated. Position 1 (see Figure

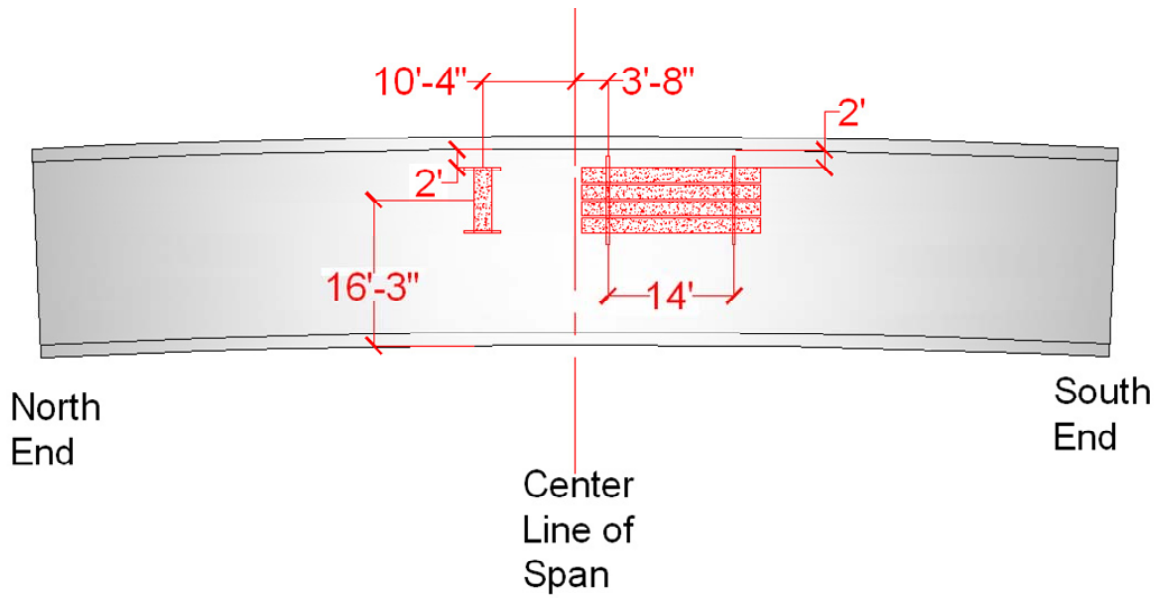
4-21) placed the live load directly over the interior girder. Previous computer modeling had shown the location to provide the greatest deflections due to the loading, and therefore this position was chosen. Once the load had been positioned for approximately 35 minutes, the load was totally removed from the bridge. The load was then reapplied to Position 2 as depicted in Figure 4-22. Position 2 (see Figure 4-22) provided a more balanced distribution of load over the entire deck. After approximately 15 minutes of strain measurements, the live load was once again totally removed from the bridge. The load was then moved to the final position that is designated as Position 3 as depicted in Figure 4-23. Position 3 placed the live load directly over the exterior girder in the position that was determined to provide the greatest deflection, much like position 1. After approximately 5 minutes of data monitoring, position 3 was unloaded to allow strain recording to continue during the unloading process. Once enough data was recorded during the unloading process, the live load was placed back on the bridge system in position 3 for further use in the fracture testing.



**Figure 4-21 Live Load Position 1**



**Figure 4-22 Live Load Position 2**

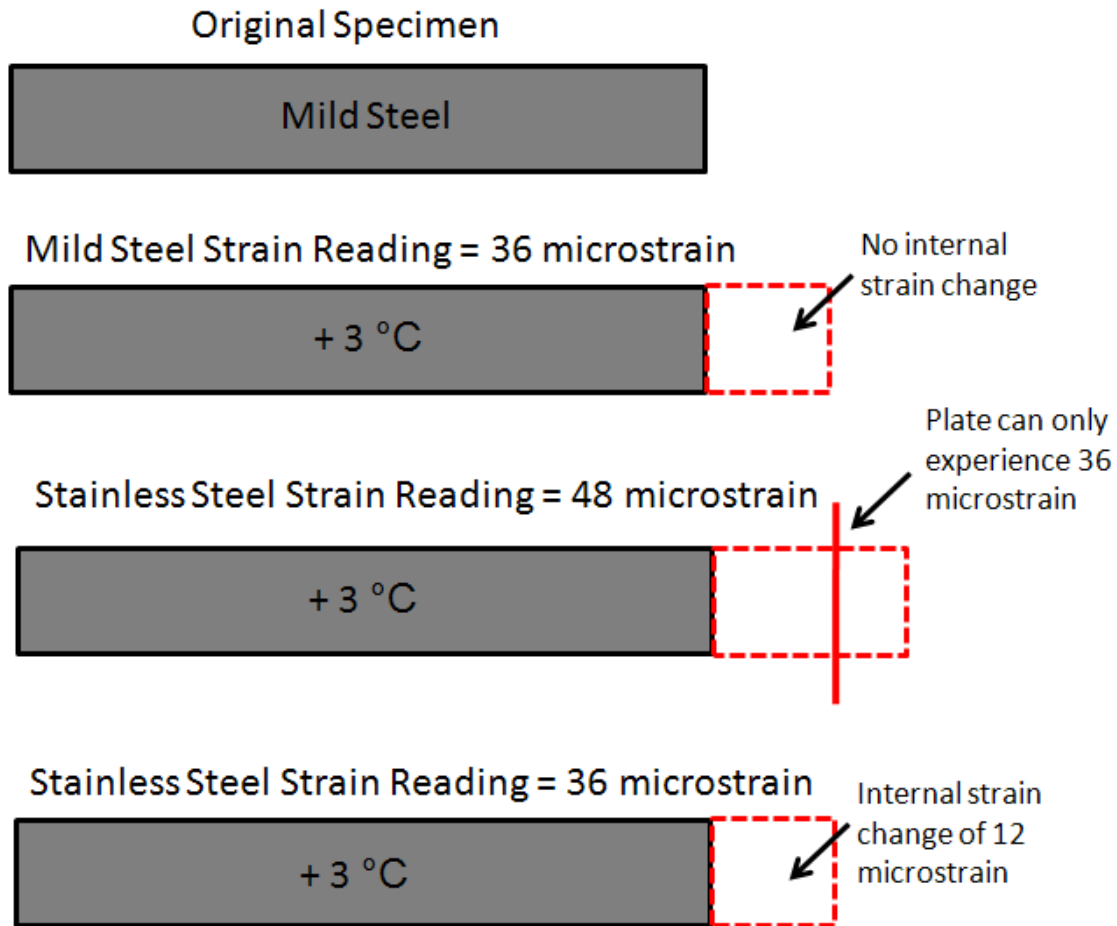


**Figure 4-23 Live Load Position 3**

Because of the length of time required to place the simulated truck loading on the bridge, temperature effects throughout each test were significant. Similar to the results provided regarding the casting of the concrete deck and rails, data was analyzed and plotted in response to the live load testing. Because the concrete deck and rails were each cast on a separate day, strain readings the night before and after each event could be analyzed, thus negating the need to correct the strain readings for thermal effects due to the absence of the sun. However, since all three simulated live load testing positions took place during the day, the temperature effects needed to be studied.

The effects of the temperature on the strain readings were estimated based upon a percentage of thermal change over the course of the test. In addition to the effects of temperature, another factor had influence on the strain readings. The steel twin girders instrumented were composed of mild steel, however, the resistive strain gages used to monitor strain readings were designed to be applied to stainless steel. One of the main differences between mild steel resistive strain gages and stainless steel resistive strain gages is their coefficient of thermal expansion. Mild steel gages have a coefficient of thermal expansion of  $11.8 \times 10^{-6} / ^\circ\text{C}$ , meaning for every change in one degree Celsius, 11.8 microstrain are present. Stainless steel gages have a coefficient of thermal expansion of  $16.2 \times 10^{-6} / ^\circ\text{C}$ . If a constrained (not free to move three-dimensionally) steel specimen is subjected to a temperature increase, it will want to expand. But since the specimen is constrained, the specimen won't stretch, but will experience additional internal strain. The coefficient of thermal expansion accounts for this so that strain readings do not need to be altered. However, since the twin steel girders were instrumented with the wrong type of strain gage, a correction was needed to include the effects of the incorrect coefficient of thermal expansion.

To explain this correction, a simple experiment was performed at the Ferguson Lab to validate the correction method used. A flat steel plate was instrumented with a mild steel strain gage, a stainless steel strain gage, and a thermocouple. The strain and temperature reading devices were monitored using the CR5000 Datalogger as used in previous aspects of this research project. The experiment included positioning the flat steel plate in different environments varying in temperature. Strain readings were taken in each location and recorded. When the specimen was exposed to temperature changes, strain changes were to be expected due to the coefficient of thermal expansion. However, since the specimen was unconstrained, strain values were expected to vary from temperature to temperature. But since the specimen was composed of mild steel, the strain readings for the mild steel strain gage were not expected to vary. Although, the stainless steel strain gage was expected to show strain changes. For example, assume the coefficients of thermal expansion for the mild and stainless gages are 12 microstrain / °C and 16 microstrain / °C respectively. Thus a three degree increase in temperature would cause the mild steel strain gage to show a strain increase of 36 microstrain, but since the specimen is composed of mild steel, this will be accounted for and the strain reading will vary minimally from the original strain reading before the temperature change. The stainless steel strain gage will act differently though, experiencing a strain of 48 microstrain. But since the specimen is composed of mild steel, the specimen cannot experience a strain from temperature of more than 36 microstrain, thus leaving the additional 12 microstrain to be locked in the specimen as an additional compressive strain. Therefore, the results would show the stainless steel strain gage with a 12 microstrain difference from the original strain reading before the temperature change. Figure 4-24 explains this method more visually.



**Figure 4-24 Steel Plate Experiment Scenario**

**Table 4-1 through**

Table 4-3 present the results of the steel plate experiment. In experiments 1 and 2, the field results are similar to the theoretical results. Theoretical results were calculated using the coefficient of thermal expansions provided with each series of strain gages. However, these values are presented as average values amongst the lot of strain gages in a purchased box. Therefore, the coefficient alters slightly from gage to gage, which can be seen in the results since the actual and theory numbers are not identical. In experiment 3 the stainless steel reading was as similar towards the theoretical value as the

previous experiments. Possible reasoning for this is due to the temperature compensation range of the strain gage itself. The strain gages used has a minimum compensation temperature of 10-15 °C. Meaning that as the strain gage is exposed to temperatures close to this range; the influence of the coefficient of thermal expansion is less accurate. Therefore, since the refrigerator temperature was 17 °C, the coefficient of thermal expansion of 16 microstrain / °C is not as accurate, which would lead to different theoretical results. Overall, the flat steel plate experiment validated researcher’s assumptions of how to correct the strain readings during the simulated live load testing. The correction method would simply incorporate two additional steps in calculating the strain readings. An example of the correction methods is presented in Appendix C.

**Table 4-1 Flat Steel Plate Experiment 1**

	<b>Temperature (°C)</b>	<b>Stainless Strain Reading (microstrain)</b>	<b>Mild Strain Reading (microstrain)</b>
<b>Inside A/C Room</b>	23.02	10.04	2.50
<b>Inside Lab</b>	24.75	2.50	2.51
<b>Δ actual</b>	1.73	-7.54	0.01
<b>Δ theory</b>		-7.61	0.00

**Table 4-2 Flat Steel Plate Experiment 2**

	<b>Temperature (°C)</b>	<b>Stainless Strain Reading (microstrain)</b>	<b>Mild Strain Reading (microstrain)</b>
<b>Inside Lab</b>	24.75	2.50	2.51
<b>Outside Shade</b>	25.99	-2.53	2.54
<b><math>\Delta</math> actual</b>	1.24	-5.03	0.03
<b><math>\Delta</math> theory</b>		-5.46	0.00

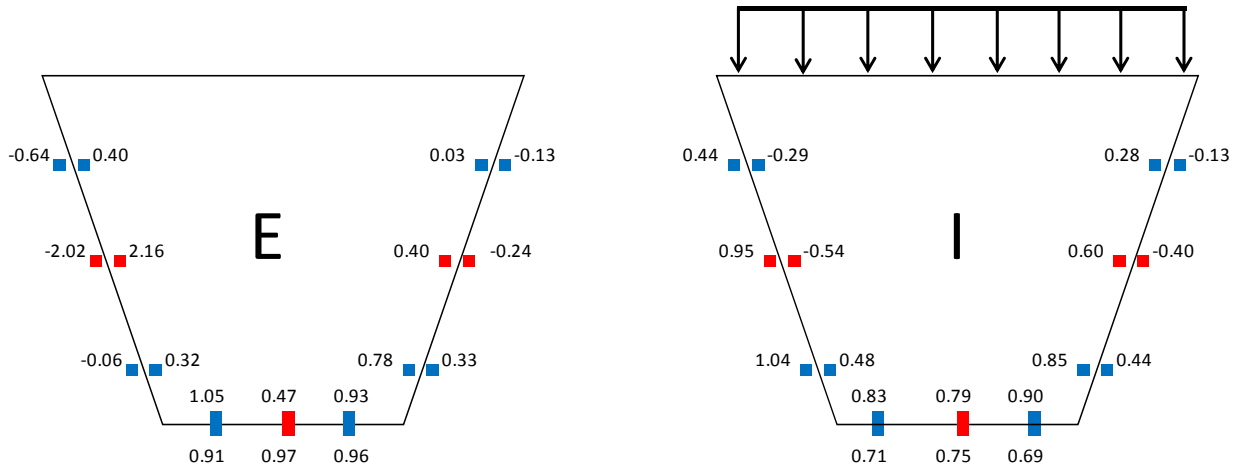
**Table 4-3 Flat Steel Plate Experiment 3**

	<b>Temperature (°C)</b>	<b>Stainless Strain Reading (microstrain)</b>	<b>Mild Strain Reading (microstrain)</b>
<b>Outside Shade</b>	25.99	-2.53	2.54
<b>Refrigerator</b>	17.09	7.68	2.54
<b><math>\Delta</math> actual</b>	-8.90	10.21	0.00
<b><math>\Delta</math> theory</b>		39.16	0.00

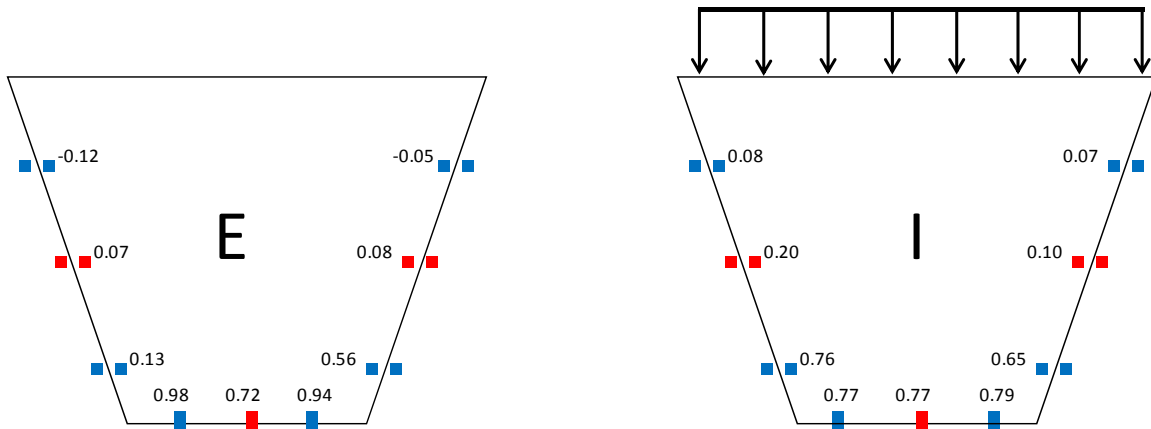
The gages at Sections A and B were monitored throughout the testing. The simulated live load testing began at 9:45 on October 5, 2006 and the unloading of position 1 began at 10:20 and lasted until 10:40. Figure 4-25 shows the change in stress values at Section A due to the live load testing at position 1. Unexpectedly, both girders showed similar levels of increase that were minimal. The interior girder was expected to show a large increase due to the load being applied directly over it. This led researchers



to believe the gages may have experienced problems. As previously performed, average stress values were taken to negate the effects of local plate bending. Figure 4-26 shows the average stress change for Section A of the girders due to the live load testing at position 1.



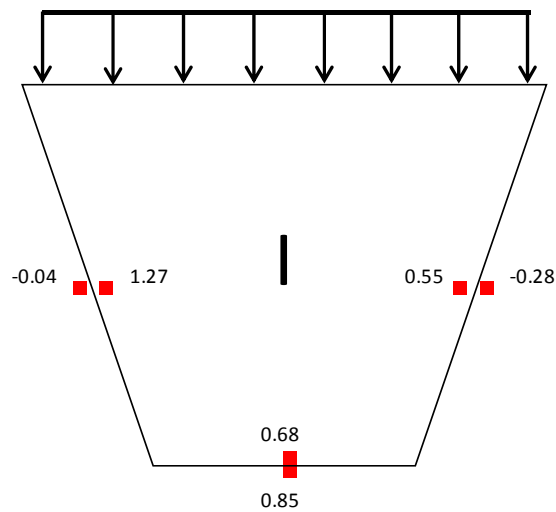
**Figure 4-25 Stress Changes due to Live Load Position 1 (ksi) Section A**



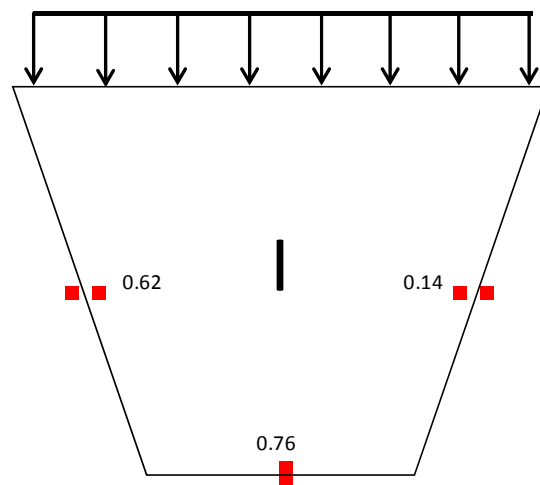
**Figure 4-26 Avg. Stress Changes due to Live Load Position 1 (ksi) Sect. A**

During the live load testing, the rosettes at Section B on the bridge system were also monitored. Results were expected to show similar stress increases, however, stress levels were expected to be lower since the majority of the live load was positioned over

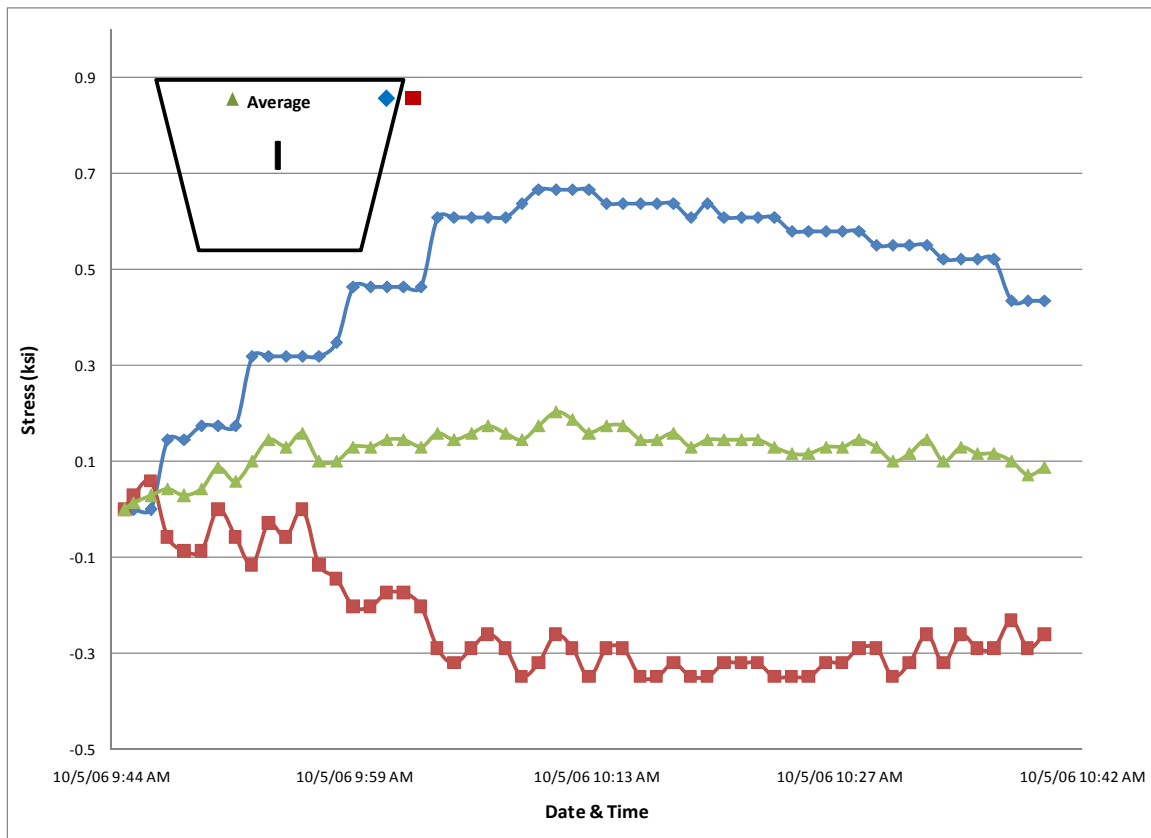
Section A as opposed to Section B. Figure 4-27 shows the change in stress values at the Section B of the girders due to the live load testing at position 1. From the results, it can be seen that the stress changes in the interior girder at both locations are very similar, except at the interior web which differs slightly. Figure 4-28 shows the average change in stress values at Section B due to the live load testing at position 1. When compared to Figure 4-26, the stress values are similar in magnitude.



**Figure 4-27 Stress Changes due to Live Load Position 1 (ksi) Section B**



**Figure 4-28 Avg. Stress Changes due to Live Load Position 1 (ksi) Sect. B**

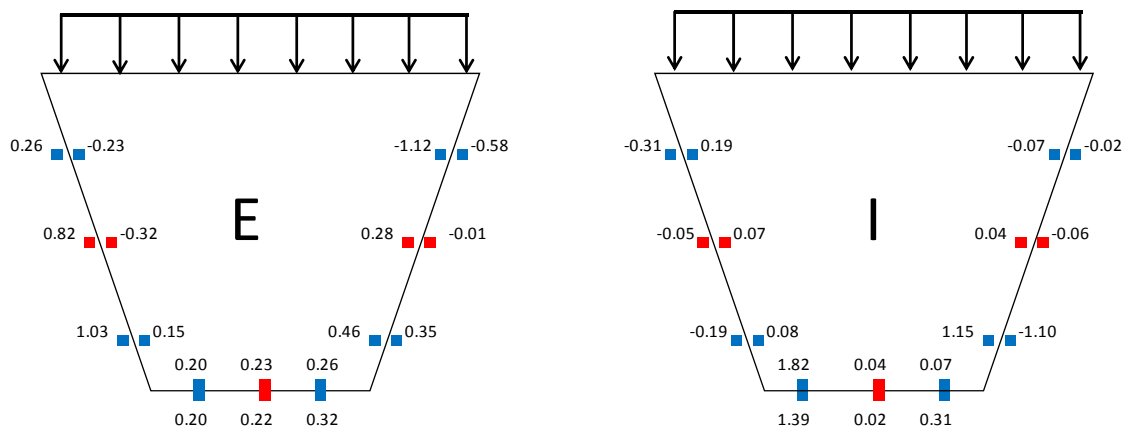


**Figure 4-29 Stress Development of Live Load Position 1 – Top of Web**

Stress levels during the live load testing were monitored during the entire process and were plotted for further analysis. Figure 4-29 shows the strain change of 2 gages on the interior girder’s exterior web versus the time period of live loading at position 1. The graph shows a consistent increase in magnitude of stress levels as expected, followed by a slight leveling off once the load was fully unloaded. However, it can be seen that the outer gage seemed to experience some noise throughout the loading. Other gage positions are graphed and presented in Appendix B.

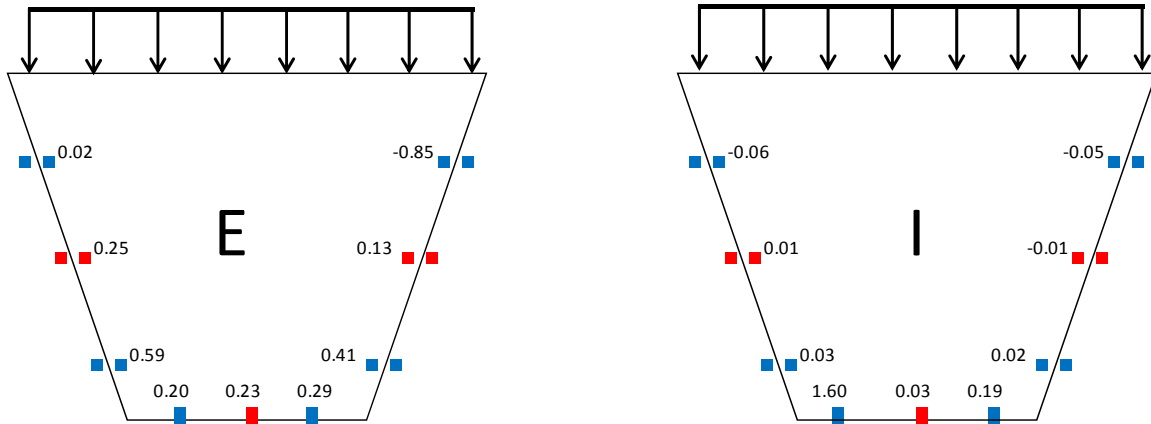
The live load was moved into position 2 at 10:50 on October 5, 2006 and was unloaded at 11:04. The load was completely removed at 11:15. Position 2 would

distribute the live load more evenly across the entire concrete deck, and thus stress changes in both girders were expected to be lower than position 1. Both girders were expected to show similar stress changes due to the symmetry of the loads position. Figure 4-30 shows the change in stress values at the section A of the girders due to the live load testing at position 2. The corresponding average stresses are shown in Figure 4-31.



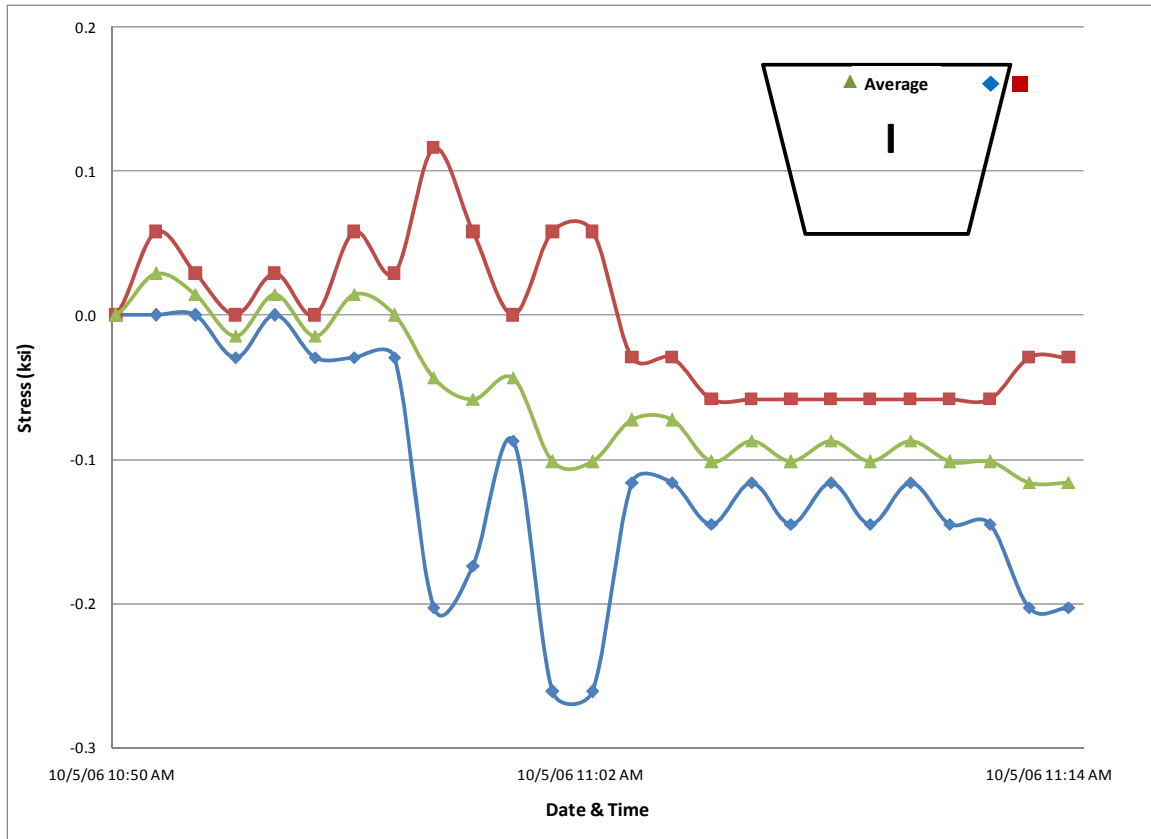
**Figure 4-30 Stress Changes due to Live Load Position 2 (ksi) Section A**

With the more uniform positioning of the truck load over the girders, it was anticipated that the stress changes in the two girders would be similar. Results show that both girders experienced similar stress changes. The distributions of the average stresses do not seem to follow a clear trend from a bending perspective. Due to the slight curvature of the bridge, it would be expected that the exterior girder will have larger bending and torsional effects; however these effects should not be too severe. Since the loads were both placed close to edges of the bridges, the relatively stiff rails may have helped support the load; however it would be anticipated that the girder bending stresses would be larger than approximately 25% of those observed in position 1.



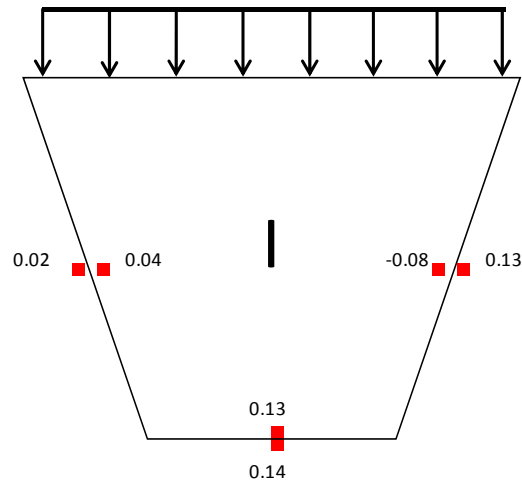
**Figure 4-31 Avg. Stress Changes due to Live Load Position 2 (ksi) Sect. A**

In analyzing the test data throughout positions 1 and 2 some of the gages experienced a significant amount of noise, which may have affected some of the readings. The trend in electronic noise can be seen in the graph of the stress development during live load testing of position 2 graphed in Figure 4-32. From the graph, it can be seen that even though the stress levels decrease overall, there are major fluctuations of stress levels during the loading process. When compared to Figure 4-29, the stress development patterns differ noticeably. Other gage locations are presented in Appendix B.

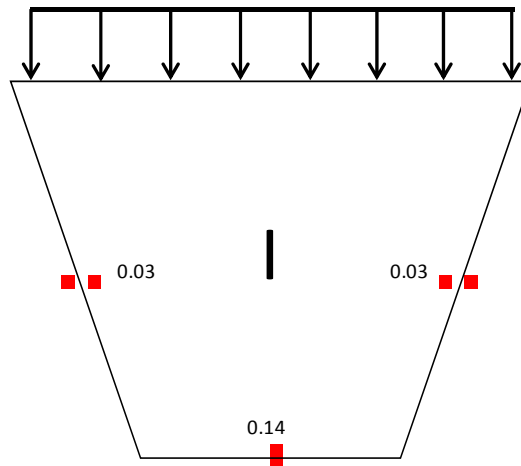


**Figure 4-32 Stress Development of Live Load Position 2 – Top of Web**

Figure 4-33 shows the change in stress values at the Section B of the girders due to the live load testing at position 2. From the results, it can be seen that the stress changes in the interior girder at both locations are very similar. Figure 4-34 shows the average change in stress values at Section B of the girders due to the live load testing at position 2. When compared to Figure 4-31, stress values are very similar as expected. When compared to Figure 4-27 and Figure 4-28, stress levels are smaller in magnitude as expected since fewer load was applied to the interior girder in position 2.

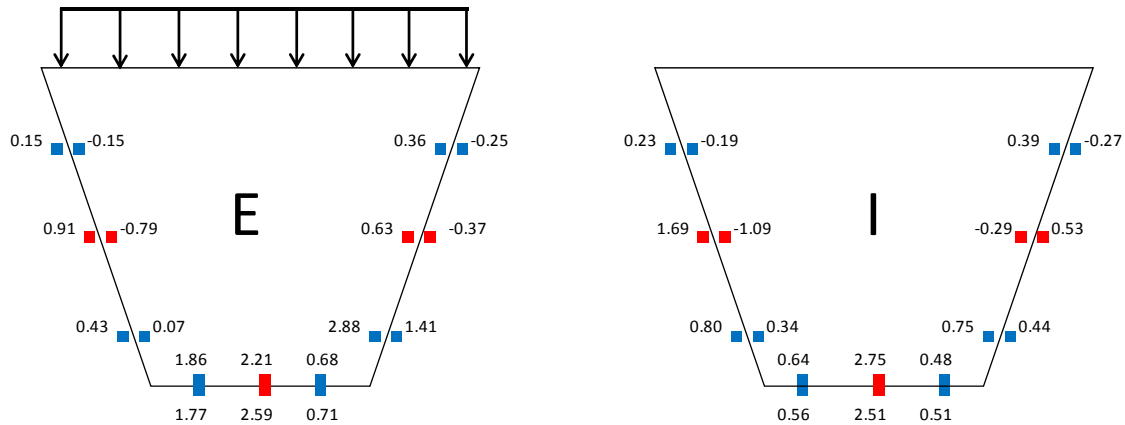


**Figure 4-33 Stress Changes due to Live Load Position 2 (ksi) Section B**



**Figure 4-34 Avg. Stress Changes due to Live Load Position 2 (ksi) Sect. B**

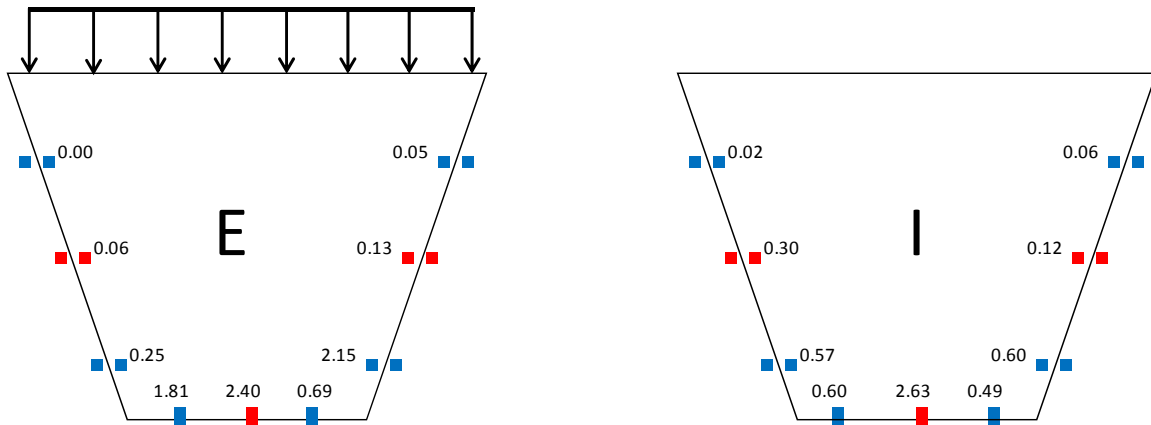
The live load was moved into position 3 at 11:18 on October 5, 2006 and was completely unloaded at 11:57. Load Position 3 placed the live load directly over the exterior girder similar to how position 1 did over the interior girder. Both girders were expected to show similar stress changes as position 1, but with the larger stress changes on the exterior girder. Figure 4-35 shows the change in stress values on Section A of the girders due to the live load testing at position 3. The average stresses at each point on the cross section are shown in Figure 4-36.



**Figure 4-35 Stress Changes due to Live Load Position 3 (ksi) Section A**

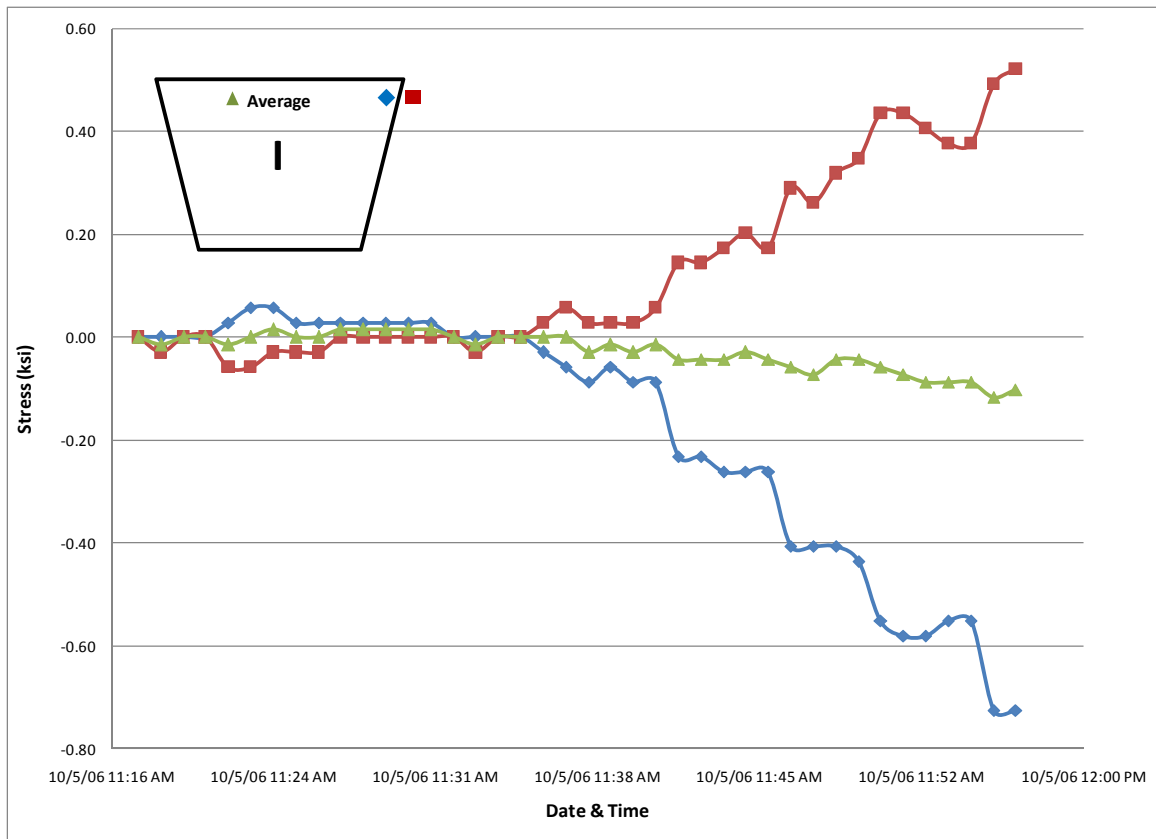
The results presented from the 3<sup>rd</sup> position of live load testing were slightly more acceptable. Both girders experienced stress levels throughout their cross-sections; however the exterior girder was shown to have higher stress levels. With the live load being placed directly over the exterior girder, stresses in the exterior girder should have been noticeably higher in magnitude than those recorded. Possible explanation for this was explained earlier with regards to position 2 of the live load testing regarding noise interference. Figure 4-37 graphs stress development at a single location during the live load testing at position 3. Similar to Figure 4-32, it can be seen that even though the stress levels seem consistent, there are major fluctuations present. Other gage locations are presented in Appendix B.



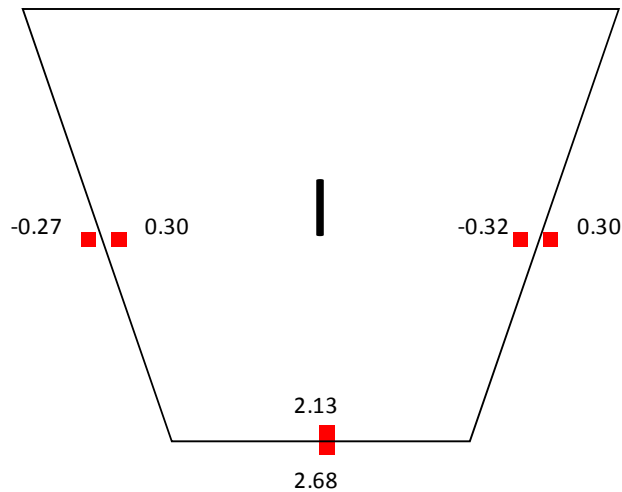


**Figure 4-36 Avg. Stress Changes due to Live Load Position 3 (ksi) Sect. A**

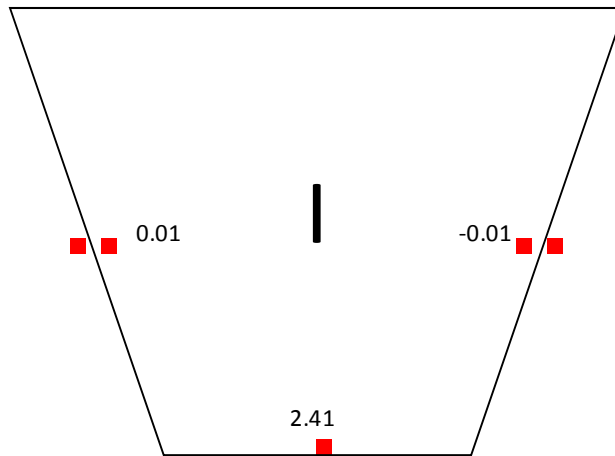
Figure 4-38 shows the change in stress values at the Section B of the girders due to the live load testing at position 3. From the results, it can be seen that the stress changes in the interior girder at both locations are very similar with the exception of the interior web. Figure 4-39 shows the average stress change in stress values at Section B of the girders due to the live load testing at position 3.



**Figure 4-37 Stress Development of Live Load Position 3 – Top of Web**



**Figure 4-38 Stress Changes due to Live Load Position 3 (ksi) Section B**

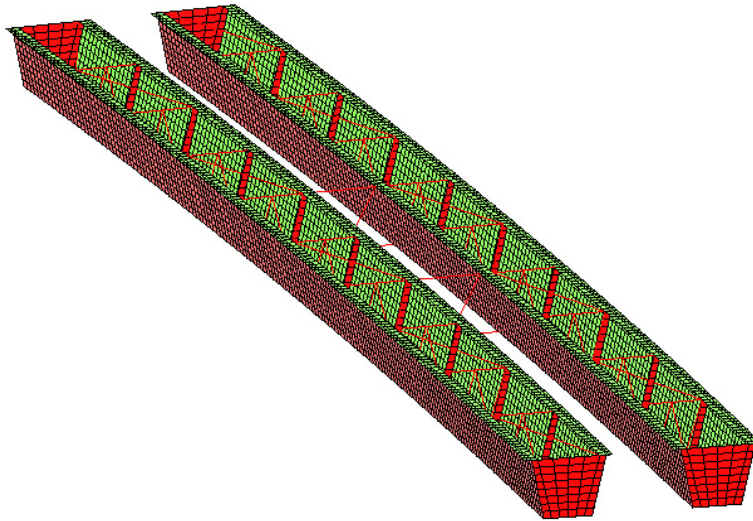


**Figure 4-39 Avg. Stress Changes due to Live Load Position 3 (ksi) Sect. B**

### **4.3 Finite Element Analysis Comparison**

An overview of results from a three-dimensional finite element analysis is presented in this section. The analysis was performed using the ANSYS software package (ANSYS 2006). The model was created by a graduate student (Quan Chen) at the University of Texas at Austin who was currently using the model for another project regarding thermal effects on the bridge system. A general overview of the characteristics of the model is provided followed by a discussion of the results predicted with the model. The model was used to study the effects of the construction of the deck and live load testing on the girders. The model was based on dimensions of the box girders with the assistance of plan drawings and geometric measurements of the girders. Figure 4-40 shows the basic model of the twin box girder system used. Simply supported box boundary conditions were modeled, and twist was restrained at the supports by stopping lateral deformation of the top and bottom of the girder web. The cross-section of the girders was made up of eight noded shell elements. Three-dimensional beam elements were used to model the internal and external cross-frames as well as the top flange lateral

truss. The actual web imperfections were modeled on the girders using measurements from the LPDG that was discussed in Chapter 3.

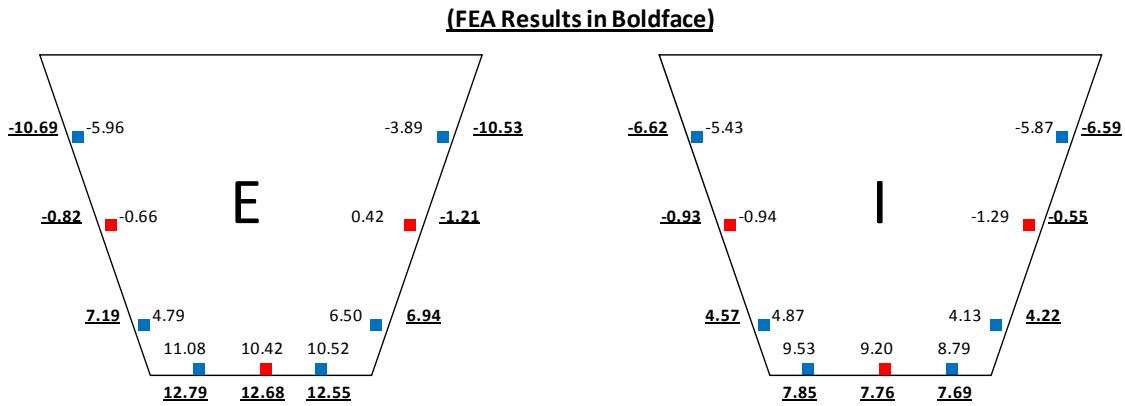


**Figure 4-40 FEA Steel Box Girders Model**

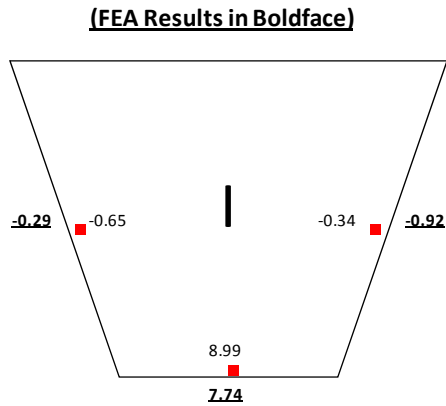
The comparison of the FEA solution and the measured results are presented simply to demonstrate the accuracy of the finite element modeling techniques that are also being conducted on the project for the parametric investigations. Figure 4-41 presents a comparison of the FEA and field results of the effects of the concrete deck casting on the girders at Section A. It should be noted that the results presented are average values of stresses used to eliminate the effects of plate bending. Field measurements are distinguished by normal text font, whereas the FEA numerical results are bold and underlined. The accuracy of the computational and measured results varies at different locations around the cross-section. The results tended to agree better on the interior girder compared to the exterior girder. The bottom flange stresses tended to agree better than web stresses; however there are some uncertainties in how to properly

model the overhang brackets and that may be where the uncertainty in the modeling exists. The same basic comparisons can be seen in Figure 4-42, which depicts the results comparison of the casting of the concrete deck at Section B. Better agreement is observed in the bottom flange stresses compared to the web stresses.

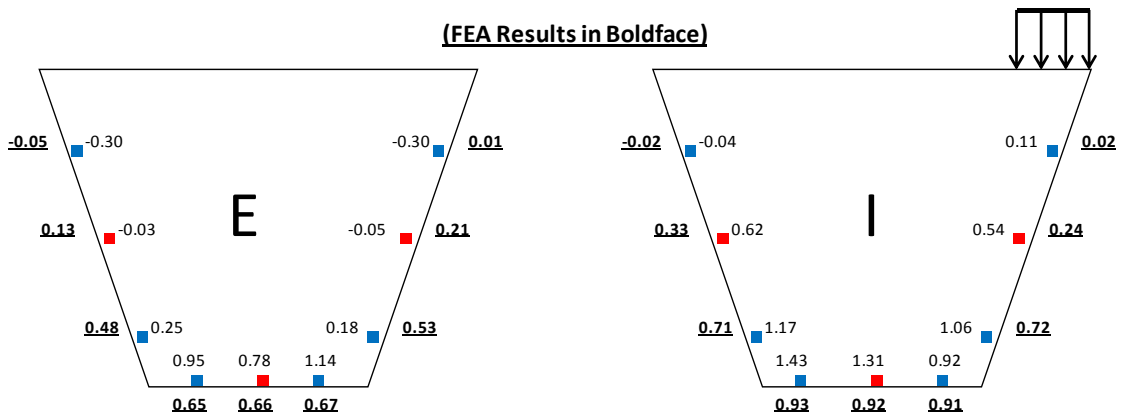
Figure 4-43 and Figure 4-44 present the comparisons of FEA results to the field results of the effects of the casting of the west rail. Figure 4-45 and Figure 4-46 present the result comparisons for the effects of the casting of the east rail. It is evident that the results comparisons for the effects of the casting of the east and west rail castings are more accurate and similar than the casting of the deck. This is most likely due to the small magnitude of load that was applied during these processes.



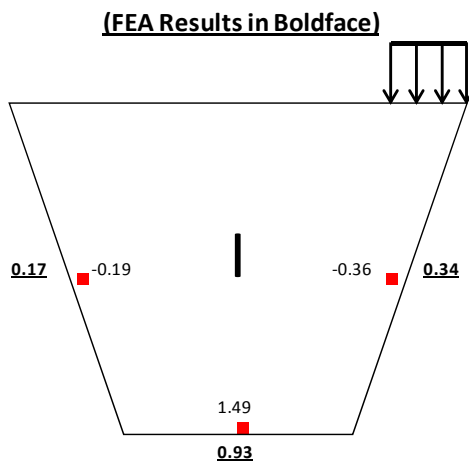
**Figure 4-41 Field & FEA Results for Construction of Deck (ksi) Section A**



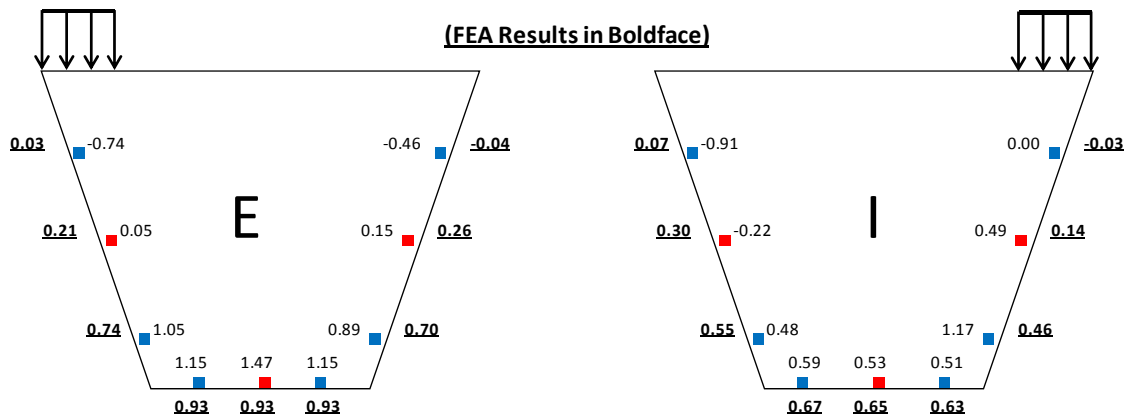
**Figure 4-42 Field & FEA Results for Construction of Deck (ksi) Section B**



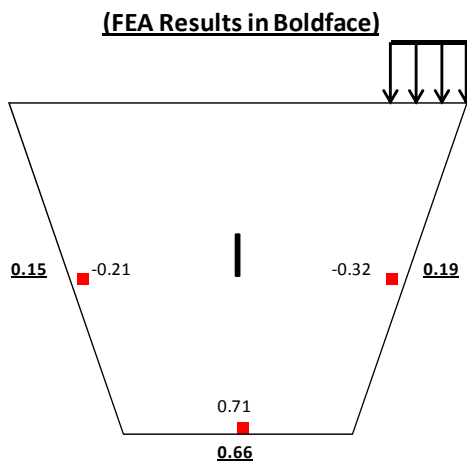
**Figure 4-43 Field & FEA Results for West Rail (ksi) Section A**



**Figure 4-44 Field & FEA Results for West Rail (ksi) Section B**



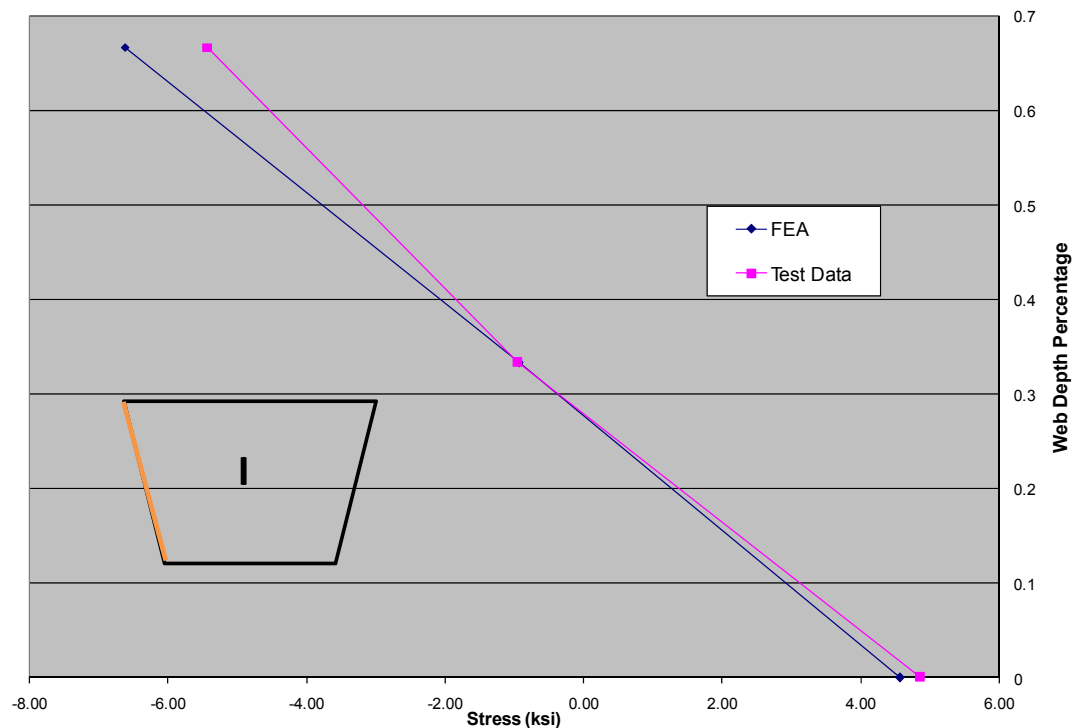
**Figure 4-45 Field & FEA Results for East Rail (ksi) Section A**



**Figure 4-46 Field & FEA Results for East Rail (ksi) Section B**

The results show that the FEA predicted similar results of the field measurements. To ensure values being analyzed and compared were sufficient for the study, stress patterns were graphed and compared for various plate elements throughout the testing phases. Figure 4-47 shows the stress distribution patterns for the interior web of the interior girder during the casting of the deck. Stress values are along the horizontal axis, whereas the vertical axis represents the depth of the web (i.e. 0.5 is mid-depth of the web). Two conclusions can be presented with the assistance of this graph. First, it is clear that the FEA results are nearly identical to the field measurements, and secondly, it

is evident that the stress distribution along the web is linear as assumed. Traveling from top to bottom along the web's depth, compressive stresses eventually become no stress (neutral axis), and then later form tensile stresses as indicated.



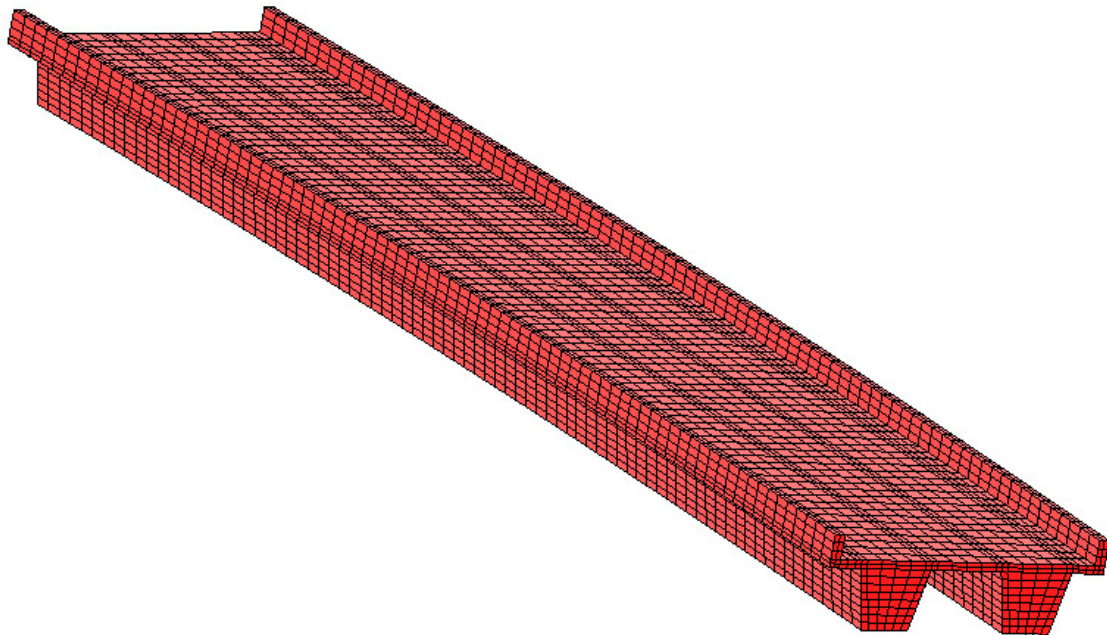
**Figure 4-47 Stress Distribution due to Deck – Inner Web of Interior Girder**

As previously stated, there are issues regarding the modeling that were overlooked. For example, the metal decking, rebar, and formwork were not accounted for. While their presence may have been minimal, estimated weights of these items should have been included in the loading values of the girder specimens. Form brackets were modeled and their relevance towards transferring loads as simulated point loads on the girders was accounted for. Although the accuracy of the modeling of the form brackets is not clear, a consistent model was used to simulate the effects of the brackets.



However, miscellaneous construction loads, such as the weight of the workers, equipment, and the screed were not accounted for and may have provided extra stresses on the girders during construction. While the unaccounted weights of these many items may seem minute to the sheer weight of the concrete deck and rails, they remain possible explanations for the slight variations in data comparisons.

Live load testing results were also compared and analyzed. The finite model was recreated to include a solid concrete deck that was fully cured and strengthened, as well as the rails. Figure 4-48 shows the model used without the live load applied.

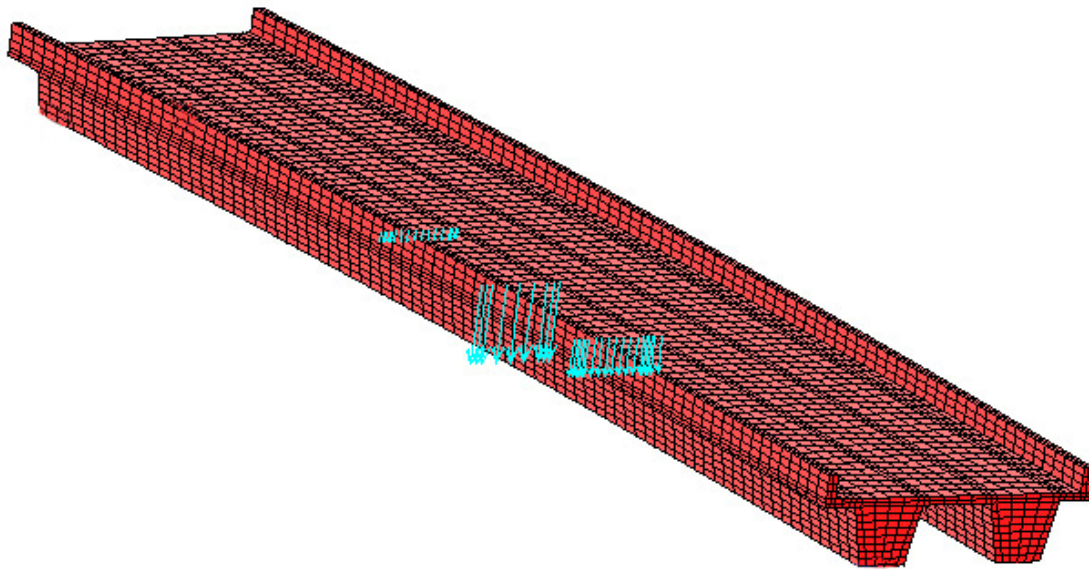


**Figure 4-48 FEA Live Load Testing Model**

There were some approximations that were taken in modeling the composite section. The rails were modeled as simple shaped vertical rectangles, whereas on the plan drawings for the bridge, they are not rectangular and include smooth curves on some

sides. The simple rectangular model should not have too significant of an effect on the model performance.

Figure 4-49 shows the FEA model that was used including the applied simulated truck live load. The truck loads are represented as point loads distributed over the exact locations as position 1 shown in Figure 4-21.



**Figure 4-49 FEA Live Load Testing Model with Applied Loads**

Figure 4-50 presents a comparison of the FEA and field results of the effects of live load position 1 on the girders at Section A. There seems to be no obvious similarities in the results, and differences seem to be scattered. At Section B, the interior web results are similar. But as Figure 4-51 depicts, the other elements results show a relatively large difference between the FEA and measured results. Although the stress magnitudes are relatively small, the difference is similar to those observed at Section A.

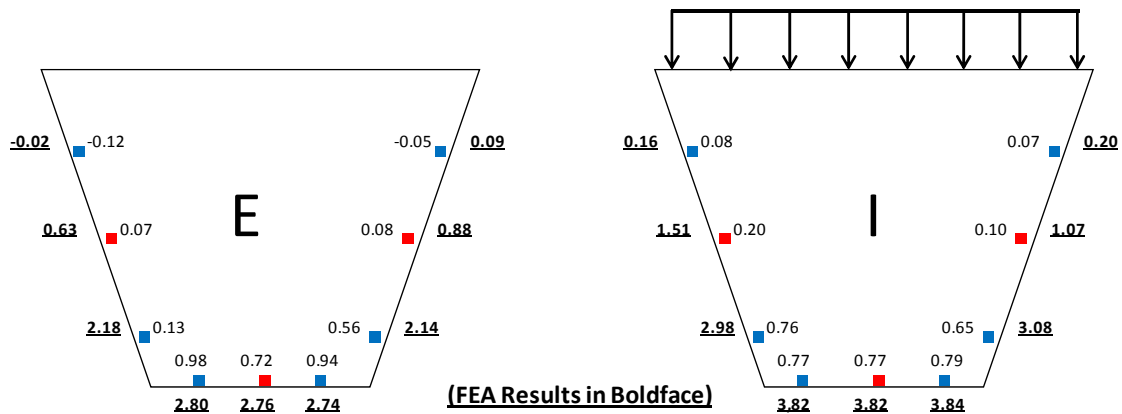


Figure 4-50 Field & FEA Results for Live Load Position 1 (ksi) Section A

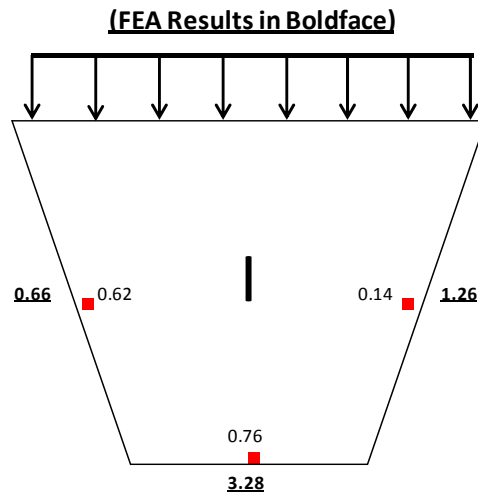


Figure 4-51 Field & FEA Results for Live Load Position 1 (ksi) Section B

Figure 4-52 and Figure 4-53 present the comparisons of FEA results to the field results of the effects of live load position 2 at both locations. Position 2 comparisons present the same inaccuracies as position 1 and vary quite noticeably. The accuracy of the measured results is questionable as outlined earlier due to the increased noise levels that were noticed. Similar comparisons were observed with the Position 3 loading as shown in Figure 4-54 and Figure 4-55. It is evident that the field results for all positions have some source of errors that affected the accuracy of the data.

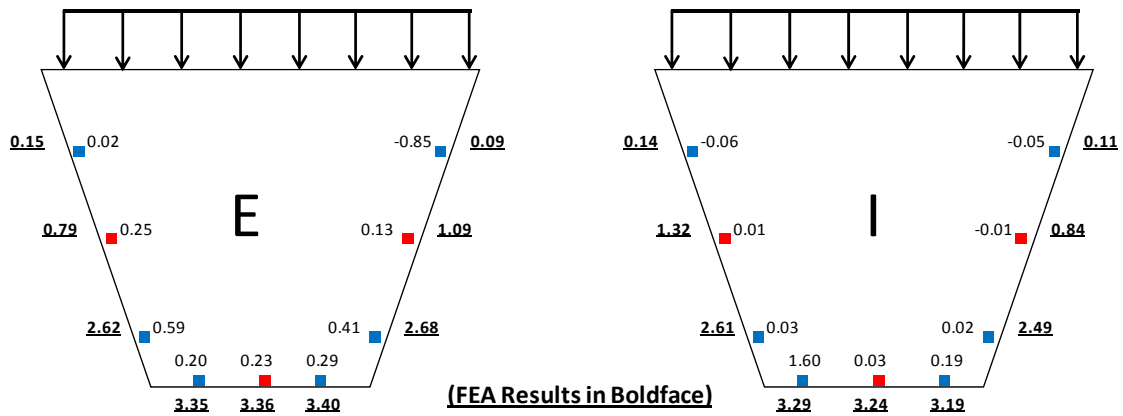


Figure 4-52 Field & FEA Results for Live Load Position 2 (ksi) Section A

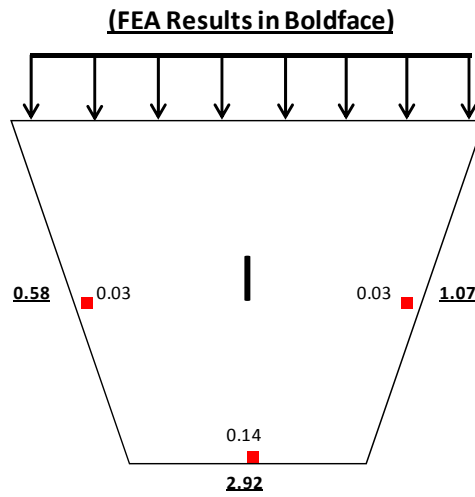


Figure 4-53 Field & FEA Results for Live Load Position 2 (ksi) Section B

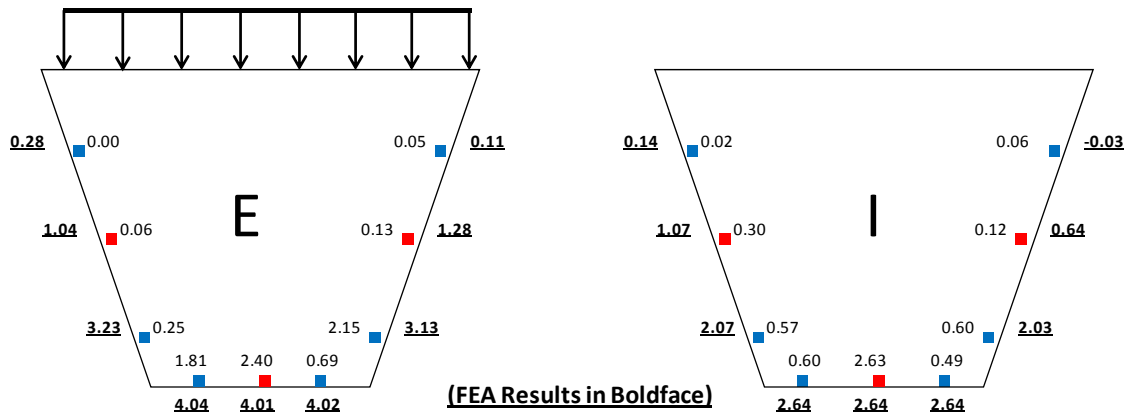
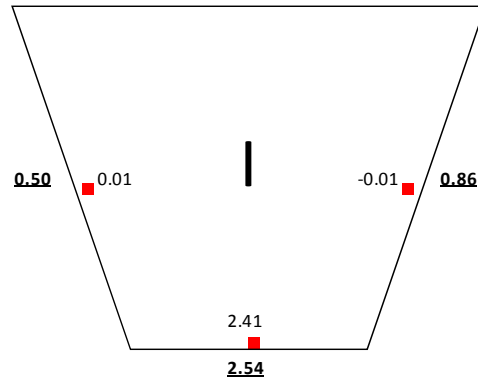


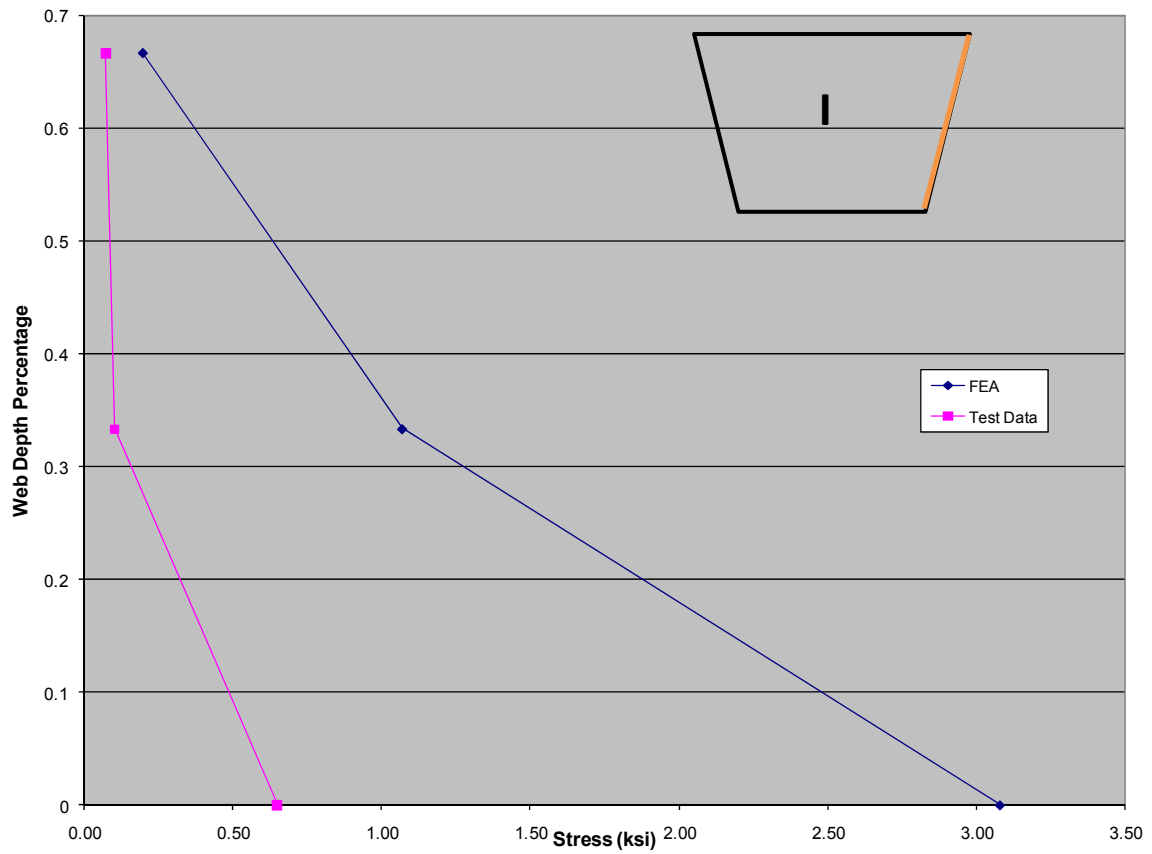
Figure 4-54 Field & FEA Results for Live Load Position 3 (ksi) Section A

**(FEA Results in Boldface)**



**Figure 4-55 Field & FEA Results for Live Load Position 3 (ksi) Section B**

As previously done, stress patterns were graphed and analyzed to ensure expected behavior was exhibited. Figure 4-56 shows the stress distribution patterns for the exterior web of the interior girder after the first position of the live load testing. From the graph, it can be seen that the FEA results are nearly double the field results, and not as accurate as the deck comparisons. However, it can be seen that both results present a slight variation from a typical linear stress distribution. Upon further review, all stress distributions for the exterior web of the interior girder during live load testing have the “bend” in distribution. The most logical explanation for this occurrence is the presence of an imperfection in the web plate element combined with the lateral load from the overhang brackets. Initial imperfections were measured before the concrete deck was cast, however, measurements were also taken after the deck was cast, and again after the form brackets were finally removed. The results from the web measurements are discussed in Chapter 5.



**Figure 4-56 Stress Distribution of Live Load Position 1 - Outer Web of Interior Girder**

## **CHAPTER 5**

### **Measurements of Plate Imperfections and Deformations**

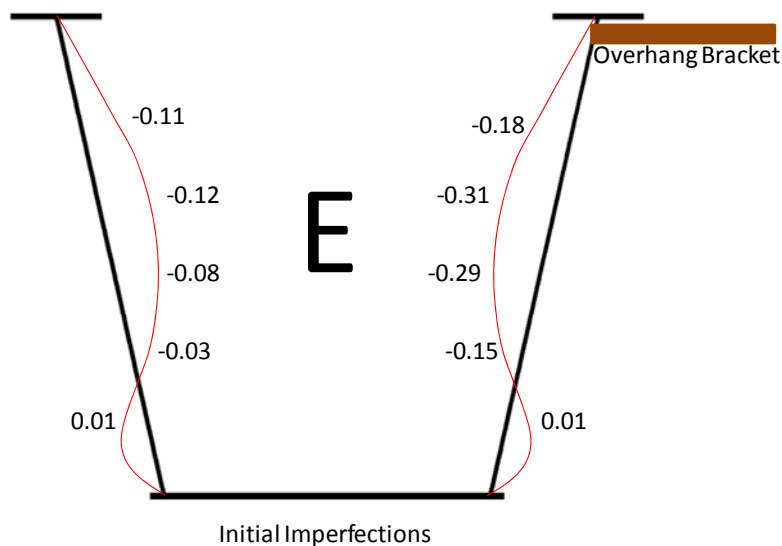
#### **5.1 Introduction**

An overview of the Linear Potentiometer Displacement Gage (LPDG) used to measure the out of flatness of the web and flange plates of the box girders throughout the construction process were presented in Chapter 3. All four webs and two bottom flanges of the entire bridge system were measured along the entire length of the specimens. Results measured were taken before any component of the concrete deck (including forms) was erected to obtain initial imperfections in the girders due to fabrication, transportation, and erection. Once the concrete deck and rails were cast, another set of measurements were taken and recorded. Finally, once the form brackets were removed from the exterior webs, a final set of measurements were taken on the external webs only. All locations shown in Figure 3-23 were measured, however only the locations instrumented with strain and temperature reading devices will be discussed in this chapter. Data results regarding all locations along the length of the girders are presented in Appendix D.

#### **5.2 Deformation of Plate Elements**

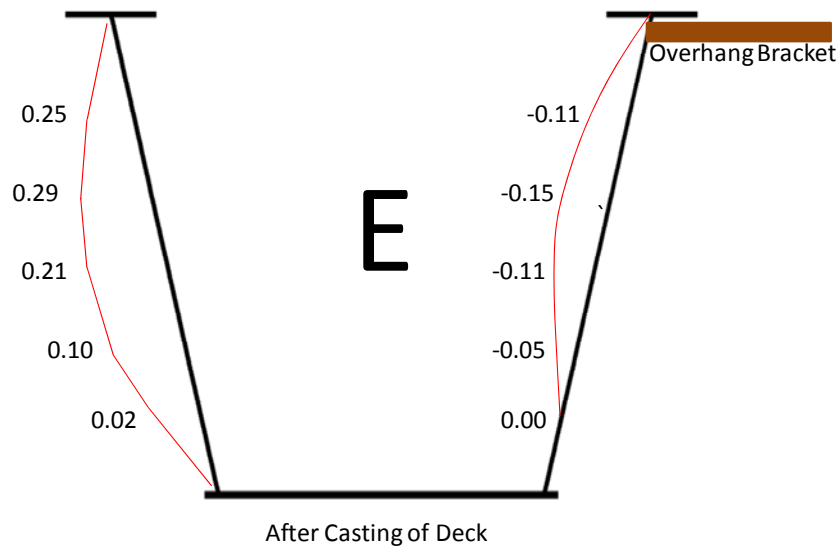
Because of their slenderness and relatively large initial imperfection, the webs of both girders were expected to experience deformations due to all aspects of the construction process. The goal of this section is to evaluate the imperfections created by various construction processes. Figure 5-1, Figure 5-2, and Figure 5-3 present the

deformations at Section A of the exterior girder. Imperfections before the casting of the deck, after the casting of the deck, and after the form bracket removal are presented. The units of all out of flatness measurements are given in inches. All readings were taken on the inside plate surfaces of the box girders. Therefore positive magnitudes signify concave curvature outward (from the box) from a perfectly flat plane, while negative magnitudes represent concave curvature inward from the plane. The imperfection curves are not drawn to scale but are instead provided as an indicator of the direction of plate bending. The magnitudes of the deformations from the five different linear potentiometers are shown next to the corresponding position on the plate. The cross-sections shown are from a south-end viewpoint, meaning for the exterior girder, the right webs are the exterior webs, and for the interior girder, the left webs are the exterior webs.

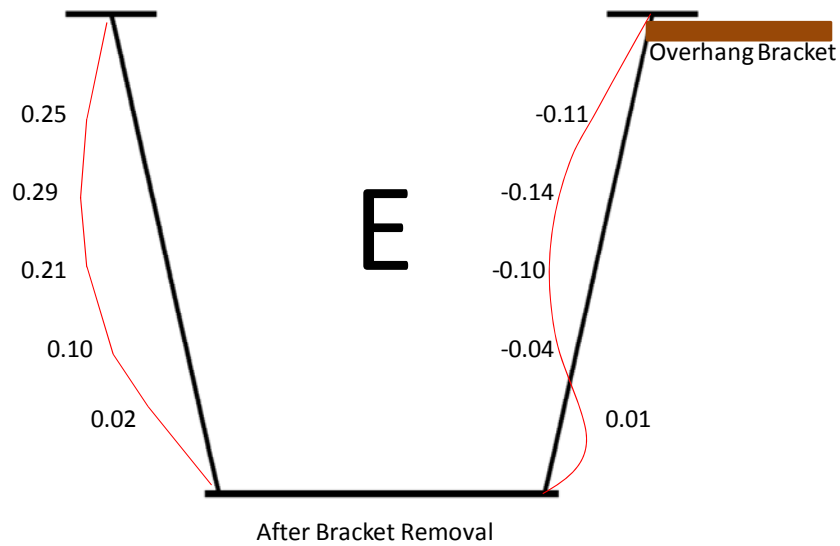


**Figure 5-1 Ext. Girder Web Initial Imperfections**





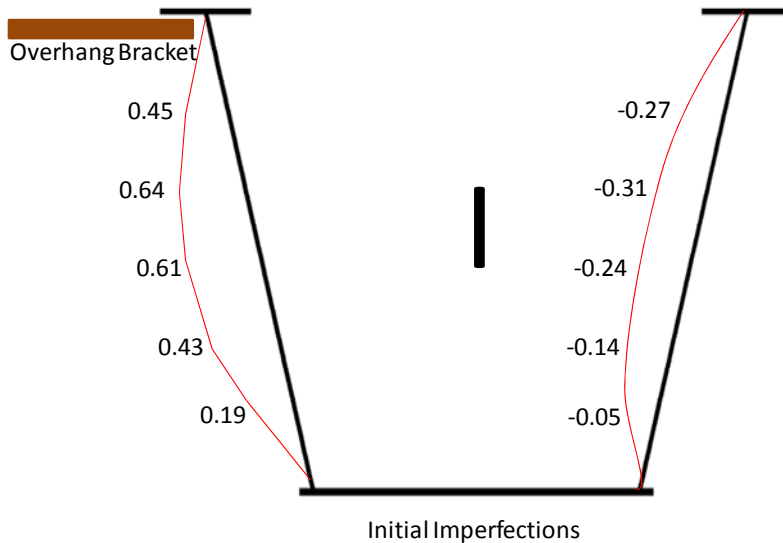
**Figure 5-2 Ext. Girder Web Deformations due to Deck Casting**



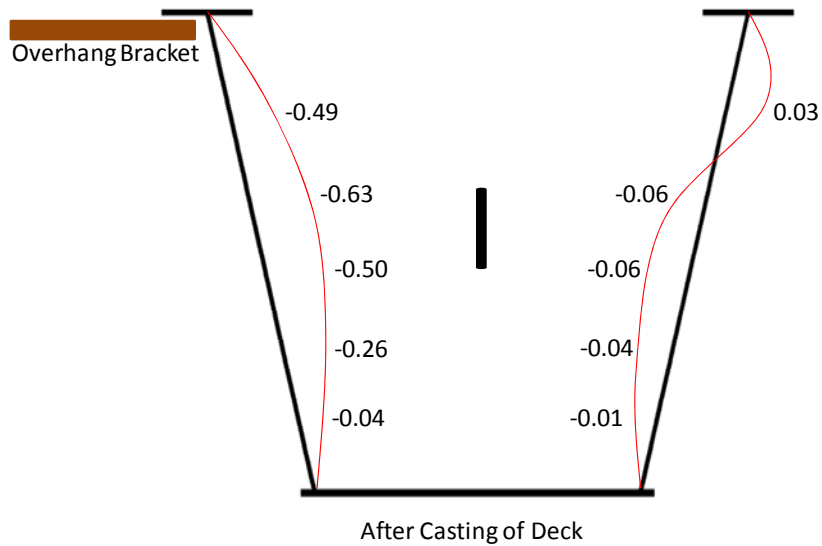
**Figure 5-3 Ext. Girder Web Deformations due to Bracket Removal**

From the figures it can be seen that both webs of the exterior girder had some initial imperfections. The majority of these imperfections were negative, meaning the web panel was buckled towards the interior of the girder. The casting of the deck was expected to increase these imperfections, especially in the interior web since no form

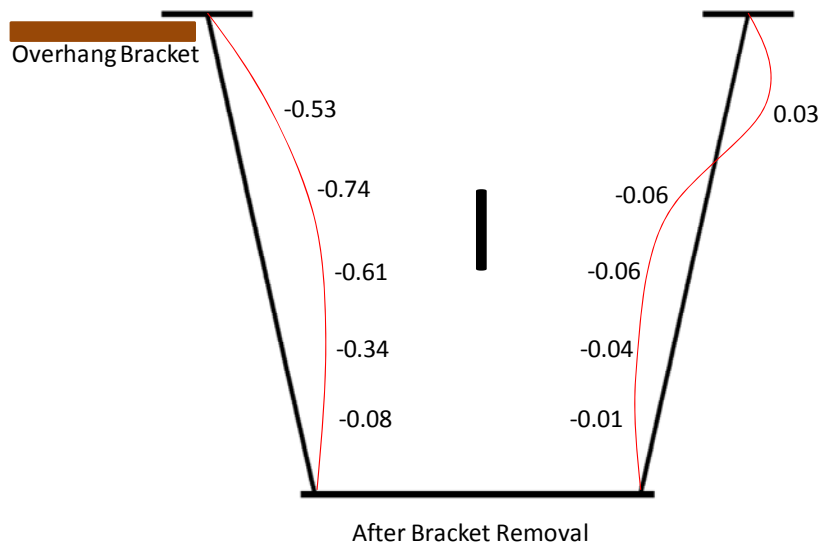
bracket was present. From the results, the interior web showed an increase in imperfection due to the casting of the deck, not only in magnitude, but in bending direction. All regions along the depth of the panel are shown to have bent outward away from the center of the girder. The exterior web was shown to bend inward, which was expected. The presence of the form brackets, and their additional forces and support pushing inward against the web is the main reason for the inward buckling. Figure 5-4, Figure 5-5, and Figure 5-6 presents the deformations at the Section A of the interior girder.



**Figure 5-4 Int. Girder Web Initial Imperfections**



**Figure 5-5 Int. Girder Web Deformations due to Deck Casting**

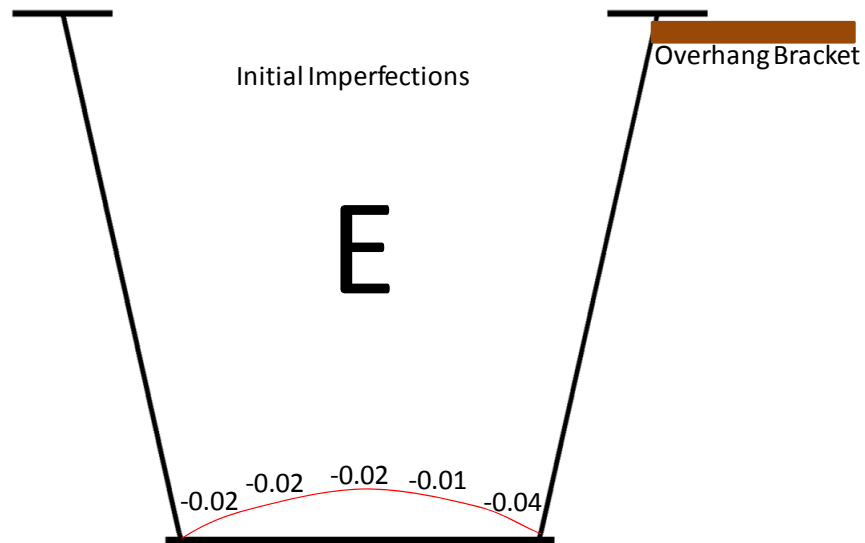


**Figure 5-6 Int. Girder Web Deformations due to Bracket Removal**

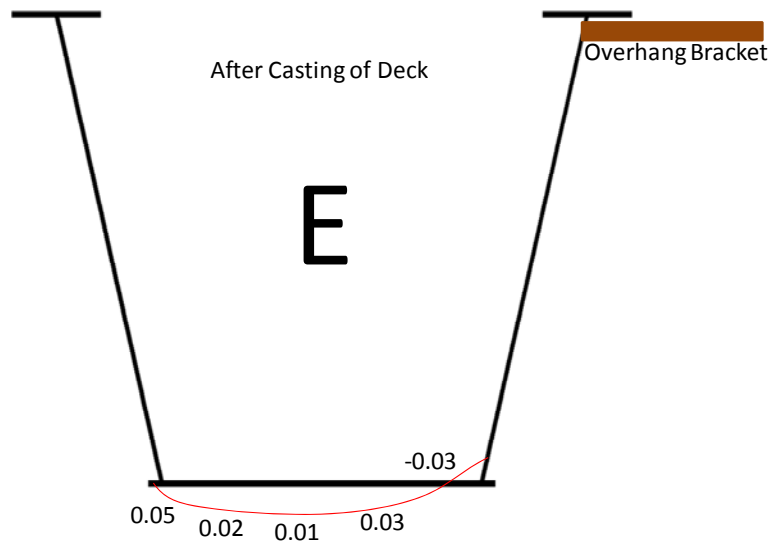
In the interior girder, the results were slightly different than the exterior girder. The interior webs of the interior girder bent outward as expected from their original inward shape, however, the magnitudes were slightly less than those of the exterior

girder. The exterior webs of the interior girder showed a different behavior than those of the exterior girder's exterior webs. It can be seen that initially the imperfections of the exterior web of the interior girder were bent in an outward shape. After the forms were attached and the concrete deck was cast, the imperfections were substantially noticeable. Most of the locations showed an inch of inward deformation from their initial imperfection. Once the form brackets were removed the web continued to bend more inwards. This behavior shows the effects of initial imperfections on the webs before any construction processes are performed. For both girders, the interior webs started with initial inward deformations. After being loaded, both webs deformed in an outward manner. However, this constant behavior was not seen in the exterior webs. The exterior girder's exterior web had an initial inward curvature. Once the load was applied, the web plate deformed outward slightly. However, the interior girder's exterior web had an initial outward curvature. Once the load was applied, the web plate deformed inward significantly. The behavior of the interior girder is more favored because of the nature of the form brackets. It would seem obvious that the forces exerted from the form brackets would cause the exterior webs to bend inward, as shown in the interior girder. However, this was not the case in the exterior girder. The reasoning for this behavior is most likely due to the bracket spacing. Brackets were positioned by contractors as best fit. Even though curvature was minimal in both girders, the exterior girder had a curvature higher in magnitude. Thus, the bracket positions would not be exact on both girders. Field distance measurements were taken for exact locations of the form brackets for use in the FEA modeling. On the interior girder, there was a bracket located directly at the main instrumented cross-section. However, on the exterior girder, the nearest bracket to the main instrumented section was 2 feet in both north and south directions.

The bottom flanges of both girders were expected to act differently than the webs because of their difference in slenderness. The webs had higher slenderness ratios due to their thinner thicknesses and longer lengths, averaging ratios of 118 to the bottom flange's 60. The flanges were roughly 10 inches shorter in length and thicker in thickness, which would provide for fewer effects of imperfections. Figure 5-7 and Figure 5-9 present the imperfections of the bottom flange of the exterior girder before and after the casting of the concrete deck. It can be seen that initially, the flange was curved slightly inward. Upon pouring and curing of the deck and rails, the flange eventually deformed outward. However, as shown the magnitudes of deformation were still almost negligible.



**Figure 5-7 Ext. Girder Bottom Flange Initial Imperfections**

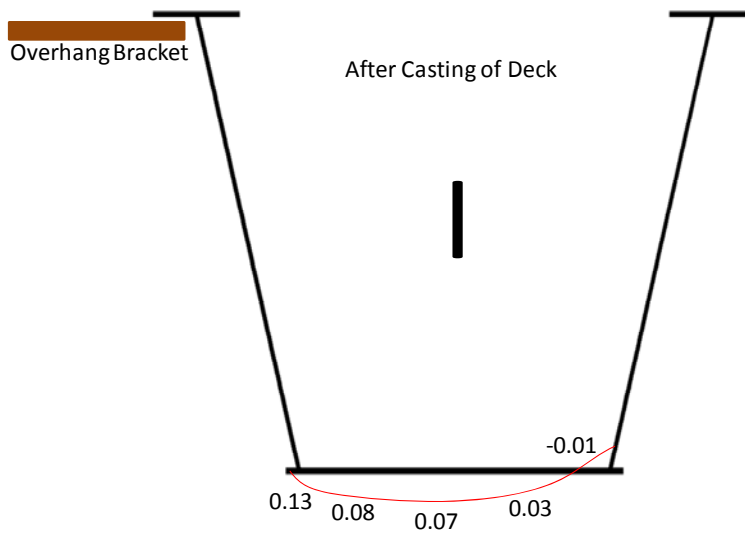


**Figure 5-8 Ext. Girder Bottom Flange Deformations due to Casting of Deck**

Figure 5-9 and Figure 5-10 present the imperfections of the bottom flange of the interior girder before and after the casting of the concrete deck. The deformation in the interior girder's bottom flange was very similar to that observed in the exterior girder. With initial imperfections that bent outward, the addition of the concrete deck further deformed the bottom flange outward. However, two points closest to the interior of the bridge system proved to deform inward slightly. In general, the bottom flange deformations were relatively small.



**Figure 5-9 Int. Girder Bottom Flange Initial Imperfections**



**Figure 5-10 Int. Girder Bottom Flange Deformations due to Casting of Deck**

### **5.3 Plate Tolerances and Public Opinion**

Plate tolerances for various specifications were discussed in Chapter 2. As shown in the results, imperfections were taken at 5 locations along the plate's depth (or width) at each location. However, when comparing the imperfection values against tolerances, only the maximum imperfection was needed. Figure 5-11 presents the maximum plate imperfections for all plate elements on both girders. Each girder consisted of 10 segments, each with 2 web panels and 1 bottom flange. True bottom flange dimension measurements were taken for the entire girder system. However, measuring web dimensions was not possible. Because the girder segments were already constructed together as one long girder piece, web thicknesses at segments other than the girder ends, were not able to be measured. Actual web depths were only measured at the ends of each girder, while the remaining interior segment dimensions were based on plan dimensions provided. Therefore, the web depths and thicknesses at all interior segments were based on plan dimensions for tolerance calculations. This proved to be efficient since actual measured values were within 1% of plan dimensions.

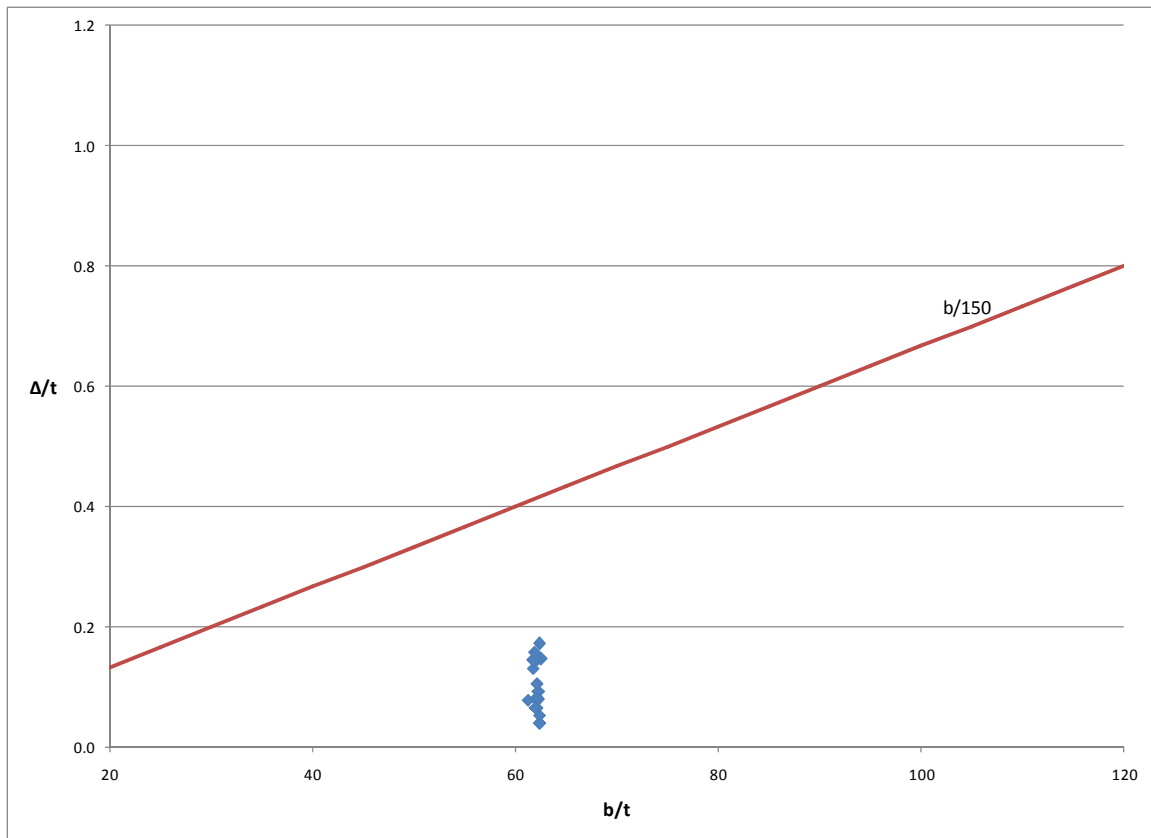


		Plate Location and Dimensions										Maximum Plate Imperfections										
Girder (from South)	Segment	Bottom Flange (BF)					Ext. Webs					Int. Webs					BF $\Delta$ (in.)	Ext. Web $\Delta$ (in.)	Int. Web $\Delta$ (in.)	BF $\Delta/t$	Ext. Web $\Delta/t$	Int. Web $\Delta/t$
		t (in.)	b (in.)	b/t	t (in.)	t (in.)	b (in.)	b/t	t (in.)	t (in.)	b (in.)	b/t	t (in.)	b (in.)	b/t							
East	1	0.751	46.938	62.501	0.498	58.938	118.348	0.498	58.813	118.097	0.11	-0.14	-0.04	0.146	0.281	0.080						
East	2	0.755	47.063	62.335	0.500	58.754	117.508	0.500	58.754	117.508	-0.03	-0.48	-0.13	0.040	0.960	0.260						
East	3	0.754	47.000	62.334	0.500	58.754	117.508	0.500	58.754	117.508	0.04	-0.59	0.31	0.053	1.180	0.620						
East	4	0.755	47.000	62.252	0.500	58.754	117.508	0.500	58.754	117.508	0.07	-0.92	-0.49	0.093	1.840	0.980						
East	5	0.757	46.967	62.044	0.500	58.754	117.508	0.500	58.754	117.508	0.05	-0.14	0.59	0.066	0.280	1.180						
East	6	0.758	47.000	62.005	0.500	58.754	117.508	0.500	58.754	117.508	0.06	-0.77	0.38	0.079	1.540	0.760						
East	7	0.756	47.000	62.169	0.500	58.754	117.508	0.500	58.754	117.508	0.06	-0.53	0.47	0.079	1.060	0.940						
East	8	0.757	47.002	62.090	0.500	58.754	117.508	0.500	58.754	117.508	0.11	-0.54	0.38	0.145	1.080	0.760						
East	9	0.758	47.000	62.005	0.500	58.754	117.508	0.500	58.754	117.508	0.05	-0.41	0.48	0.066	0.820	0.960						
East	10	0.761	46.938	61.679	0.521	59.094	113.424	0.515	58.906	114.381	0.10	-0.15	0.42	0.131	0.288	0.816						
West	1	0.756	46.938	62.087	0.496	58.938	118.826	0.497	57.750	116.197	-0.08	0.49	-0.22	0.106	0.988	0.443						
West	2	0.754	47.000	62.334	0.500	58.754	117.508	0.500	58.754	117.508	0.03	-0.46	-0.43	0.040	0.920	0.860						
West	3	0.755	47.063	62.335	0.500	58.754	117.508	0.500	58.754	117.508	0.03	-0.43	0.19	0.040	0.860	0.380						
West	4	0.756	47.000	62.169	0.500	58.754	117.508	0.500	58.754	117.508	0.06	0.65	-0.44	0.079	1.300	0.880						
West	5	0.755	47.063	62.335	0.500	58.754	117.508	0.500	58.754	117.508	0.13	-0.74	-0.49	0.172	1.480	0.980						
West	6	0.757	47.000	62.087	0.500	58.754	117.508	0.500	58.754	117.508	0.08	0.57	-0.65	0.106	1.140	1.300						
West	7	0.761	47.000	61.761	0.500	58.754	117.508	0.500	58.754	117.508	-0.11	0.25	-0.78	0.145	0.500	1.560						
West	8	0.76	47.000	61.842	0.500	58.754	117.508	0.500	58.754	117.508	-0.12	0.32	-0.34	0.158	0.640	0.680						
West	9	0.759	47.063	62.007	0.500	58.754	117.508	0.500	58.754	117.508	-0.05	-0.23	-0.42	0.066	0.460	0.840						
West	10	0.767	46.938	61.197	0.499	58.875	117.986	0.496	57.688	116.305	-0.06	0.22	-0.15	0.078	0.441	0.302						

*\*Only web thicknesses (t) and widths (b) at end of each girder could be measured, others were based on plan dimensions*

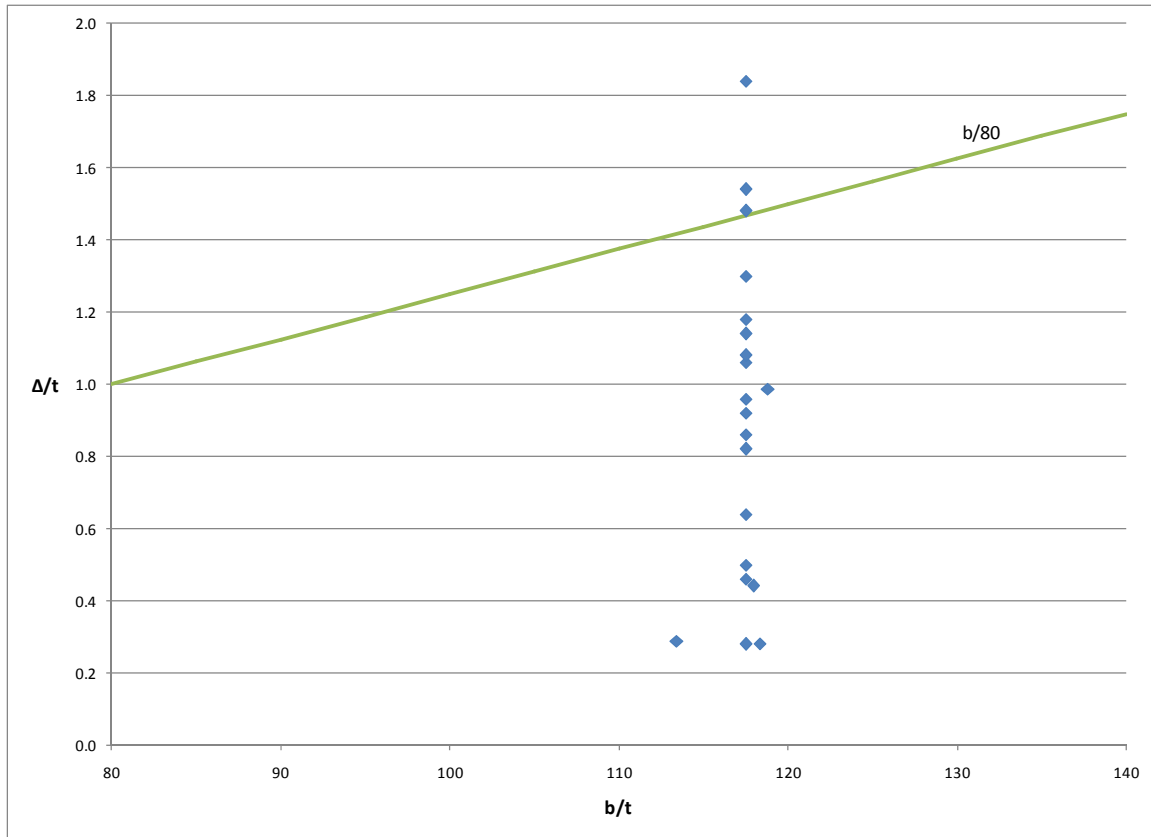
**Figure 5-11 Dimensions and Plate Imperfections of Plate Elements**

The bottom flange plate elements of 20 steel box girder segments were studied. From the results, Figure 5-12 was graphed for further analyses. The plate slenderness ratios are graphed versus the plate imperfection factor. For tolerance comparison, values from the AASHTO/AWS D1.5 2002 Bridge Welding Code were used. Although the Bridge Welding Code presents no tolerance limits on flange members, the worst case value of  $D/150$  was chosen. It can be seen from the figure that all bottom flange imperfections are well within the  $b/150$  limit. The slenderness ratios for bottom flanges throughout the girder system ranged from 60-65 and are standard in practice.



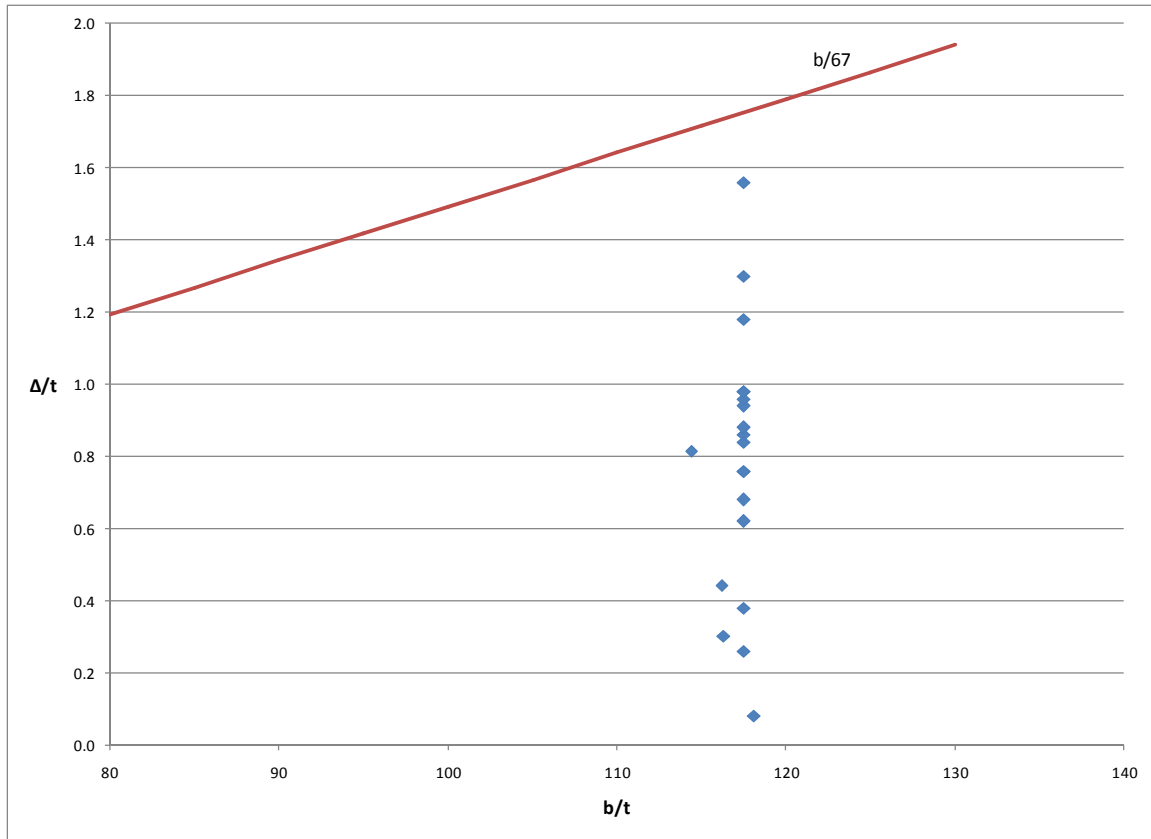
**Figure 5-12 Maximum Bottom Flange Imperfections**

Similar to the bottom flange plate elements, all web plate members were graphed and analyzed. Figure 5-13 presents the results for the exterior webs for both girders. According to the AASHTO/AWS D1.5 2002 Bridge Welding Code, tolerance limits are  $b/80$  for members where  $D/t \geq 100$ . Twenty exterior web panels were graphed and analyzed and it can be seen that all but a few were within the tolerance limits. While a few webs are shown to not be within the specification tolerance, it must be reminded that they are located on the interior segments of the bridge and therefore, thickness and height dimensions used in calculations were based on plan dimensions and not exact measurements. However, because field measurements were within 1% of plan dimensions, it is safe to say the plan dimensions are sufficient in this study. The slenderness ratios for exterior webs throughout the girder system ranged from 115-120 which are typical of those used in practice.



**Figure 5-13 Maximum Exterior Web Imperfections**

Figure 5-14 presents the results for the interior webs for both girders. According to the AASHTO/AWS D1.5 2002 Bridge Welding Code, tolerance limits are  $b/67$  for members where  $D/t \geq 100$ . The tolerance limit is not as strict as exterior girders mainly due to aesthetic effects since the fascia girder is more visible than interior girders. Twenty interior web panels were graphed and analyzed and it can be seen that all are within the tolerance limits. The slenderness ratios for interior webs throughout the girder system ranged from 115-120 which are typical of those used in practice.



**Figure 5-14 Maximum Interior Web Imperfections**

The Bridge Welding Code’s tolerance limits are an example of how public perception can affect the specification. The tolerance limits for the exterior girders are stricter than for interior girders. This is believed to be because the public eye can see imperfections and deformations of exterior exposed plate elements (or girders in some cases) compared to interior elements. As an addition to the imperfections measured throughout the bridge system a public survey was conducted. Participants were informed about the background of web imperfections and then asked to visibly examine twelve web panels that had been marked on the girders. The individual web panels were numbered for identification and participants were asked to rate the panels “flatness” on a scale of 1 to 10, 1 being straightest. A total of twelve participants were surveyed and the

results were analyzed. Prior to the survey, web imperfections were calculated and specific panels chosen containing a mixture of panels with varying levels of imperfection. To simplify results, all panels voted with a value of 1-4 were labeled as flat, and panels voted 5-10 were assumed non-flat. Table 5-1 presents the breakdown of each panel votes along with the panel's actual rating. The survey results provide some interesting issues regarding public-eye finding web imperfections. It can be seen that the public only properly identified panels 1, 5, 6, 7, and 12. Although on panels 9 and 11, the vote was split evenly and could have swayed either way. Given the results from the survey, it is evident that public perception of deformations and imperfections varies from person to person. It is also of interest that of the 8 panels officially deemed "non-flat" only 1 of these violated the plate tolerance limit set forth in the Bridge Welding Code. Further public-eye tests with larger numbers of panels and participants should be conducted if public perception is to be used as criteria for plate tolerance limits in the future.

**Table 5-1 Public-Eye Plate Tolerance Survey Results**

<b>Panel ID</b>	<b>Imperfection (inches)</b>	<b>Votes for Non-Flat</b>	<b>Votes for Flat</b>	<b>Average User Rating (1-10)</b>	<b>Actual Rating</b>
1	0.08	2	10	3.0	Flat
2	1.18	4	8	4.3	Non-flat
3	0.96	2	10	2.8	Non-flat
4	1.18	5	7	4.8	Non-flat
5	1.06	8	4	5.4	Non-flat
6	0.29	0	12	2.4	Flat
7	0.44	2	10	2.8	Flat
8	1.30	2	10	4.0	Non-flat
9	1.56	6	6	4.2	Non-flat
10	1.30	5	7	5.2	Non-flat
11	1.48	6	6	6.0	Non-flat
12	0.46	0	12	3.0	Flat

## CHAPTER 6

### Conclusions

#### 6.1 Overview

Box girder bridges have a number of advantages that make them an attractive choice for steel bridge applications. Box girders are increasing in popularity, however, with the increase in cost of steel, fabricators and engineers are looking for methods to maximize savings. The most common practice of minimizing cost is to reduce plate thicknesses; however, there are still a number of unknowns on the impact of reducing the plate thickness on the structural behavior. While reducing the plate thickness may have economic advantages with respect to material costs, the increase in slenderness may have detrimental effects on the structural performance of the girders.

Current United States specifications generally provide minimal assistance on slenderness tolerances for box girder sections. Depending on the specification, plate tolerances vary from source to source, and very little background information is provided on the background or basis for how the tolerances were derived and formulated. Most specifications available also provide limited or no guidance on measuring plate imperfections, leading to further confusion for engineers, fabricators, and inspectors. The AASHTO/AWS D1.5M/D1.5 Bridge Welding Code (2002) provides a sufficient presentation of plate tolerances dependent on boundary conditions of the plate element. The specification also properly addresses how to measure plate deformations; however while the specification is directed at I-shaped girders, no guidance is specifically given for box girders. In particular, the bottom flanges of box sections are not properly addressed. Throughout the specifications available, missing information and



inconsistency can be found, leading to a mass of confusion when analyzing plate deformations. The need to improve the organization and unity of slenderness limits within the United States for box girders was part of the impetus for the study reported in this thesis.

The material presented in this thesis is part of a larger study on plate tolerances for steel box girders. The overall project includes field measurements, laboratory studies, and computational investigations. The focus of this thesis is to provide stress patterns in box girders due to various construction and live loading phases, as well as a measure of the imperfections related to these various events. The data presented in this thesis will help assist future graduate researchers working on the computational and laboratory aspects of the overall study. The results presented will help assist researchers in understanding the structural behavior of slender plate elements, as well as their impact on the overall stability of the bridge system. Along with the structural behavior, typical magnitudes of plate deformations due to various construction and live load processes were provided to further assist researchers with general indications of what is expected in field-related applications. The data can therefore provide guidance and a strong background in the assistance of formulating accurate plate tolerances based on structural behavior that will confidently be implemented into current specifications to help provide a more unified practice.

## **6.2 Summary of Results**

The field studies were conducted on a composite trapezoidal twin-box girder bridge that was erected and constructed at the University of Texas at Austin's Ferguson Structural Engineering Laboratory. Stresses throughout the girders were measured and

monitored during construction of the concrete slab, as well during simulated live load testing. Girder stresses were compared to predictions from a finite element model. The FEA model provided an accurate representation of the box girder system and will help provide further information towards the computational studies aspect of the overall project. In addition to the monitoring of the structural behavior, plate deformations were also measured. Imperfections in all plate elements throughout the entire bridge system were measured at three different phases including prior to placement of the concrete deck or formwork, after the concrete deck and rails had cured, and following the removal of the form brackets. The following sections further describe the results of the field studies.

### **6.2.1 Stress Distributions and Changes**

Although there was a small amount of torsional warping stresses in the girders, the distribution of the stresses on the girder cross-section were primarily dominated by bending type stresses. The webs also experienced a significant amount of local plate bending that was demonstrated by the pair of gages that were provided at three locations through the depth of the web. Although the bottom flange had a small amount of local plate bending, the magnitudes were relatively small compared to those exhibited by the web gages. From a deformational perspective, the upper portions of the webs experienced the largest increase in plate deformation during casting of the bridge deck with some deformations in the web plates that averaged 1 inch deformation change in magnitude before and after the casting of the deck. As expected the large deformations occurred in the webs of the girder on which the form brackets reacted upon. While the bottom flange also had some bending deformations that occurred in the plate, the effects were relatively minimal compared to the web. The reason the deformations were smaller

is because the slenderness of the bottom flange was lower. In addition, since the bottom flange was tensile in nature, the stress change was not as detrimental to the imperfection as are compression loads.

The casting of the west and east concrete deck rails provided little stress change in the box girders. Stress changes were minimal as expected due to the lower weight of the rails when compared to the concrete deck. Stress distribution patterns were linearly consistent throughout the girder components during the construction phases.

Comparisons between the FEA model and field results varied from case to case. The FEA results had better agreement in the bottom flange stresses than those of the webs. The main reason for the inconsistency in the agreement with the web stresses between measured and predicted values is likely due to the variable web imperfection as well as the presence of the overhang brackets. Although efforts were made to mimic the web imperfection based upon measurements, based upon only a few readings of the imperfection in each panel a good deal of uncertainty exists in how accurately the FEA web imperfection matched the distribution of the actual imperfection. In addition, the effect of the frame brackets can vary dramatically depending on where these brackets react.

A live load simulation was performed on the bridge following proper curing of the concrete deck. An AASHTO HS-20 truck was simulated using AASHTO Type IV prestressed concrete beams that were available for use at the laboratory facility. The beams were placed in 3 different locations simulating 3 different loading scenarios.

There was some difficulty with the data retrieval during these tests. The data acquisition from these tests was switched from the use of data loggers to a high speed system. In addition, the gages that utilized in the tests had the wrong temperature compensation factor and had to be adjusted. This latter factor was complicated by the

fact that there were significant thermal changes from the beginning of the tests until the end. The thermal effects were not present in the construction phases since for the girder stresses were determined before and after the construction activity by considering data with the same nighttime temperature. However since each of the truck loading cases was completed within approximately 1 hour, additional assumptions were made with regard to the average temperature change that occurred during the test. Although efforts were made to correct for the improper temperature compensation as well as the thermal stresses that developed due to thermal gradients on the bridge, the results during the live load tests were inconsistent compared to FEA modeling of the tests. Position 1 of the live load testing had the best agreement between measured and FEA predictions when compared to the other two positions. This may have been due to the fact that the test was done first thing in the morning where the sunlight exposure was indirect since the test began early in the morning. Tests with Positions 2 and 3 were conducted later in the day when thermal effects were much more severe.

### **6.2.2 Plate Deformations**

The other aspect of this research project was the measuring of plate imperfections and deformations during various construction processes. Plate imperfections were measured using the Linear Potentiometer Displacement Gauge (LPDG) in conjunction with a Campbell Scientific CR5000 datalogger. The LPDG consisted of 5 linear potentiometers fixed to an aluminum channel section. The device was calibrated with respect to a reference surface. The devices were then used to measure deformations in all webs and bottom flanges of both box girders at various stations along the length of the bridge system. Overall, 72 locations along the bridge's 4 webs and 36 locations along the

bridge's 2 bottom flanges were measured. Each location had a total of 5 readings at individual locations within the specific location to obtain an indication of the deformation profile along the plate width. All individual deformations for the entire bridge are presented in Appendix D.

For the scope of this research project, only the plate deformations at the location of the main instrumented cross-section were reviewed and discussed. From the results found, it was relevant that the construction of the concrete deck had significant influence on the magnitudes of plate deformations in the webs, generally providing deformations between  $\frac{1}{2}$  and 1 inch. Perhaps the most significant conclusion reached was the correlation of imperfection and stress change. It was found that the compression portions of the webs (at the upper regions of the girders) were subjected to not only the highest stress changes, but as well as the largest deformations. The bottom flanges, even though they presented high tensile stresses, were less exposed to deformations mainly due to their lower slenderness and tensile type stresses.

Although only the deformations at the main instrumented section were analyzed, all plate deformations were compared to current tolerance values. All bottom flange maximum deformations were compared to the AASHTO/AWS D1.5 2002 Bridge Welding Code. Although the Bridge Welding Code does not have specific tolerances for bottom flange elements, the most stringent tolerance of  $D/150$  was chosen to reference. All bottom flanges are easily within the tolerance limit and had slenderness values ranging from 60 to 65. All exterior web maximum deformations were compared to the Bridge Welding Code as well. For exterior web panels (where  $D/t \geq 100$ ), the tolerance limit was  $b/80$ . All of the exterior web panels were under the tolerance limit, with the exception of 3 web panels. Due to difficulty measuring the actual web slenderness, the web slenderness values that were used was based solely on plan dimensions and on

extensive field measurements. All interior web maximum deformations were compared to the Bridge Welding Code additionally. For interior web panels (where  $D/t \geq 100$ ), the tolerance limit was  $b/67$ . All interior web panels were well within the suggest tolerance value.

### **6.3 Future Work**

Because this thesis represents work for only a single aspect of the overall TxDOT research project, further work must be performed. The results presented in this thesis along with work from other components of the study will provide a solid foundation towards the understanding of plate deformations and suitable tolerances. The data comparisons that were obtained were primarily based upon the behavior at a single cross-section location on each girder. Data from additional regions or other girder systems will represent a wider range of imperfections and girder properties.

Additional work is currently being conducted using finite element models to properly predict the structural behavior of the entire bridge system during the various construction phases. This can then be compared to the deformations throughout the entire bridge that this thesis provides to further support or negate the correlation of deformations and structural behavior. The results presented in this thesis, along with future research findings, will then be used to establish a basis future plate tolerance limits.

## APPENDIX A

### CR5000 Field Monitoring Program

In Chapter 3 of this thesis, use of the CR5000 and PC9000 software systems were discussed. The program provided in this section is a portion of the actual program used to monitor stress and temperature changes on the box girder bridge system at the Ferguson Structural Engineering Laboratory. The purpose of providing this program is to assist future researchers in developing similar programs. Depending on the project, researchers will be able to modify the program to mirror their specific needs. Other researchers using CR5000 dataloggers, AM416 multiplexers, foil resistive strain gages, rosette strain gages, and thermocouples may use this program as a reference for similar applications.

#### A.1 Complete Program

'Program name: DL-1-CR.5

'Written by: omar espinosa

'Date written: 08-2-2006

'this program was written to test half of the gages on

'the bridge girders at FSEL.

^\\ VARIABLES \\\

```
Public tref, i, initial, ini
public thermo_X(22)
public foil_H(12), bblk_H(12), foil_L(11), bblk_L(11)
public ros_C(15), bblk_C(15), ros_E(12), bblk_E(12)
public foil_S(10), bblk_S(10), foil_R(10), bblk_R(10)
public bat_V
```

```
^//////////////////// DATA TABLES //////////////////////////////////////
```

```
DataTable (strain,true,1000)
```

```
cardout(1,10000)
```

```
sample(12,foil_H(),ieee4)
```

```
sample(11,foil_L(),ieee4)
```

```
sample(15,ros_C(),ieee4)
```

```
sample(12,ros_E(),ieee4)
```

```
sample(10,foil_S(),ieee4)
```

```
sample(10,foil_R(),ieee4)
```

```
EndTable
```

```
DataTable (temps,true,1000)
```

```
cardout(1,10000)
```

```
sample(1,bat_V,ieee4)
```

```
sample(22,thermo_X(),ieee4)
```

```
EndTable
```



^\\ START PROGRAM \\

BeginProg

initial=0

Scan(30,MIN,3,0)

PanelTemp(tref,200)

battery(bat\_V)

^\\\\\\\\\\\\\\\\\\\\\\\\\\\\\\\\ thermo multiplexer X start \\\\\\\\\\\\\\\\\\\\\\\\\\\\\\\\\\\\

PortSet(1,1)

i=1

SubScan(0,sec,22)

Portset(8,1)

Delay(0,20,msec)

Portset(8,0)

TCdiff(thermo\_X(i),2,30,3,0,tref,true,200,250,1.8,32)

i=i+2

NextSubScan

PortSet(1,0)

^\\\\\\\\\\\\\\\\\\\\\\\\\\\\\\\\ thermo multiplexer X end \\\\\\\\\\\\\\\\\\\\\\\\\\\\\\\\\\\\

^\\\\\\\\\\\\\\\\\\\\\\\\\\\\\\\\ foil multiplexer H start \\\\\\\\\\\\\\\\\\\\\\\\\\\\\\\\\\\\

PortSet(2,1)

```
i=1
SubScan(0,sec,12)
  PortSet(8,1)
  Delay(0,20,msec)
  PortSet(8,0)
  BrFull(bblk_H(i), 1, mV200, 5, Vx2, 1, 5000, false, false, 1000, 250, 1, 0)
  StrainCalc(foil_H(i), 1, bblk_H(i), 0, -1, 2.13, 0)
  i=i+1
NextSubScan
PortSet(2,0)

^\\\\\\\\\\\\\\\\\\\\ foil multiplexer H end \\\\\\\\\\\\\\\\\\\\\

^\\\\\\\\\\\\\\\\\\\\ foil multiplexer L start \\\\\\\\\\\\\\\\\\\\\

PortSet(3,1)
  i=1
  SubScan(0,sec,11)
    PortSet(8,1)
    Delay(0,20,msec)
    PortSet(8,0)
    BrFull(bblk_L(i), 1, mV200, 8, Vx2, 1, 5000, false, false, 1000, 250, 1, 0)
    StrainCalc(foil_L(i), 1, bblk_L(i), 0, -1, 2.13, 0)
    i=i+1
NextSubScan
```

PortSet(3,0)

^\^^^^^^^^^\ foil multiplexer L end ^^^^^^^^^^^^^^^^^^

^\^^^^^^^^^\ rosette multiplexer C start ^^^^^^^^^^^^^^^^^^

PortSet(4,1)

i=1

SubScan(0,sec,15)

PortSet(8,1)

Delay(0,20,msec)

PortSet(8,0)

BrFull(bblk\_C(i), 1, mV200, 6, Vx3, 1, 5000, false, false, 1000, 250, 1, 0)

StrainCalc(ros\_C(i), 1, bblk\_C(i), 0, -1, 2.10, 0)

i=i+1

NextSubScan

PortSet(4,0)

^\^^^^^^^^^\ rosette multiplexer C end ^^^^^^^^^^^^^^^^^^

^\^^^^^^^^^\ rosette multiplexer E start ^^^^^^^^^^^^^^^^^^

PortSet(5,1)

i=1

SubScan(0,sec,12)

PortSet(8,1)



^\^^^^^^^^^\ foil multiplexer R start ^^^^^^^^^^^^^^^^^^

PortSet(7,1)

i=1

SubScan(0,sec,10)

PortSet(8,1)

Delay(0,20,msec)

PortSet(8,0)

BrFull(bblk\_R(i), 1, mV200, 10, Vx4, 1, 5000, false, false, 1000, 250, 1, 0)

StrainCalc(foil\_R(i), 1, bblk\_R(i), 0, -1, 2.13, 0)

i=i+1

Next SubScan

PortSet(7,0)

^\^^^^^^^^^\ foil multiplexer R end ^^^^^^^^^^^^^^^^^^

CallTable strain

CallTable temps

NextScan

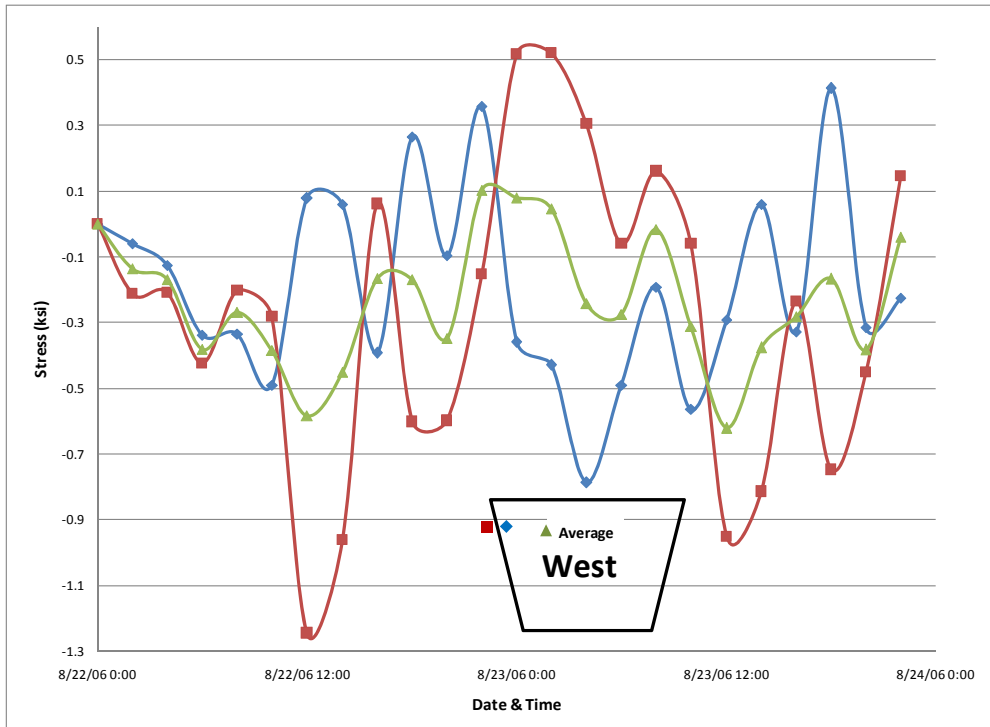
EndProg

## **APPENDIX B**

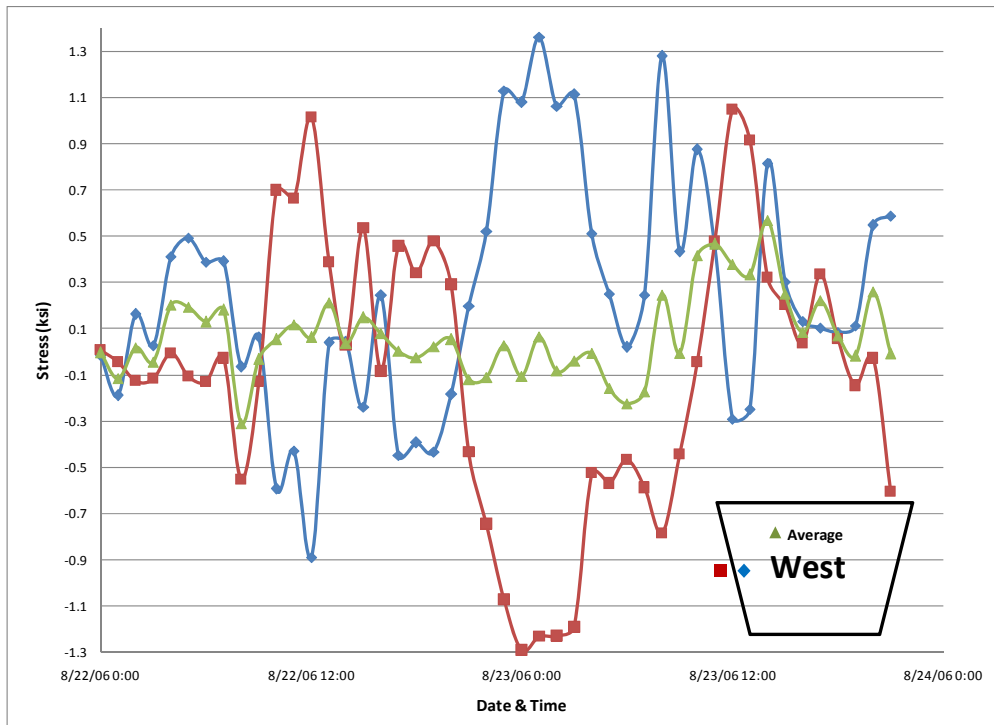
### **Stress Distribution during Construction and Live Loading**

#### **B.1 Stress versus Time – Casting of Rails**

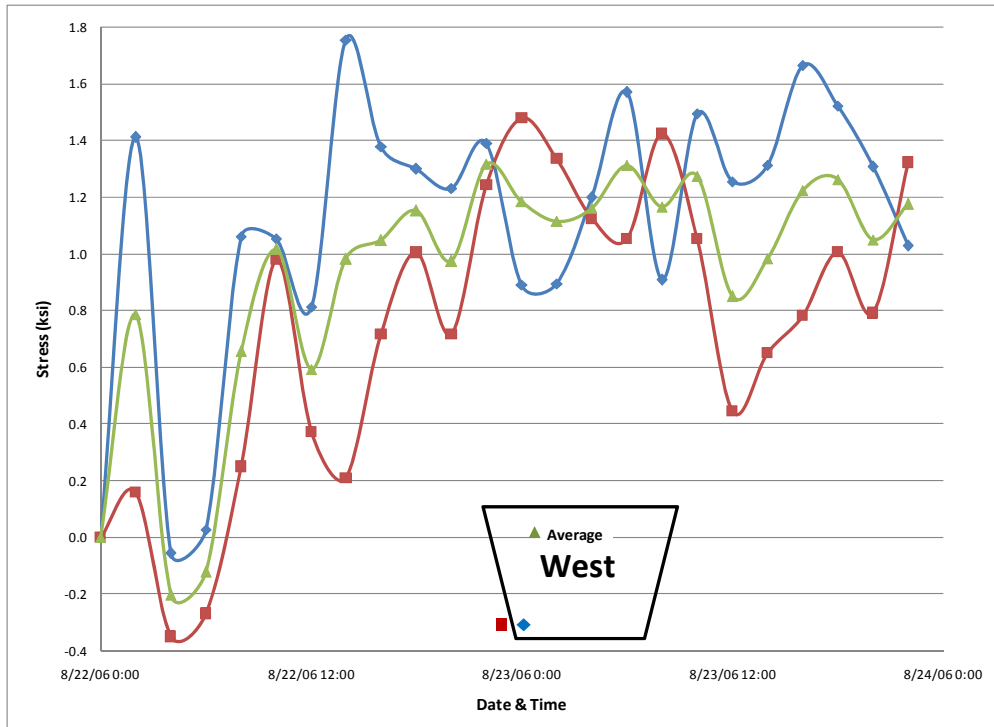
Chapter 4 of the thesis provided specific graphs depicting stress values as a function of time. The figures were provided as a basis for tracking changes in girder strains over a period of time. The graphs also clearly presented the effects of plate bending in the specimens. The chapter only presented these results due to the casting of the concrete deck. This section will present the results due to the casting of the west and east rails. Due to the light weight of the rails compared to the weight of the concrete deck, relatively small changes in stress were expected. Figures B-1 through B-3 show the gage readings along the outer web during casting of the West Rail. The corresponding graphs during casting of the East Rail are shown in Figure B-4 through B-6.



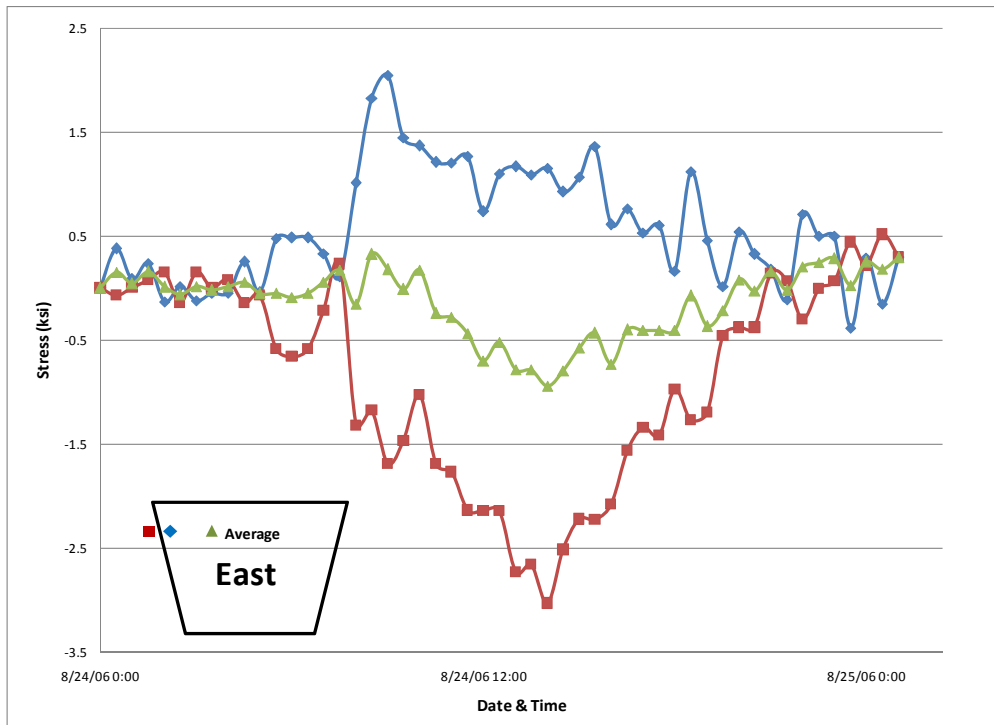
**Figure B-1 Stress Development of West Rail Casting – Top of Web**



**Figure B-2 Stress Development of West Rail Casting – Middle of Web**

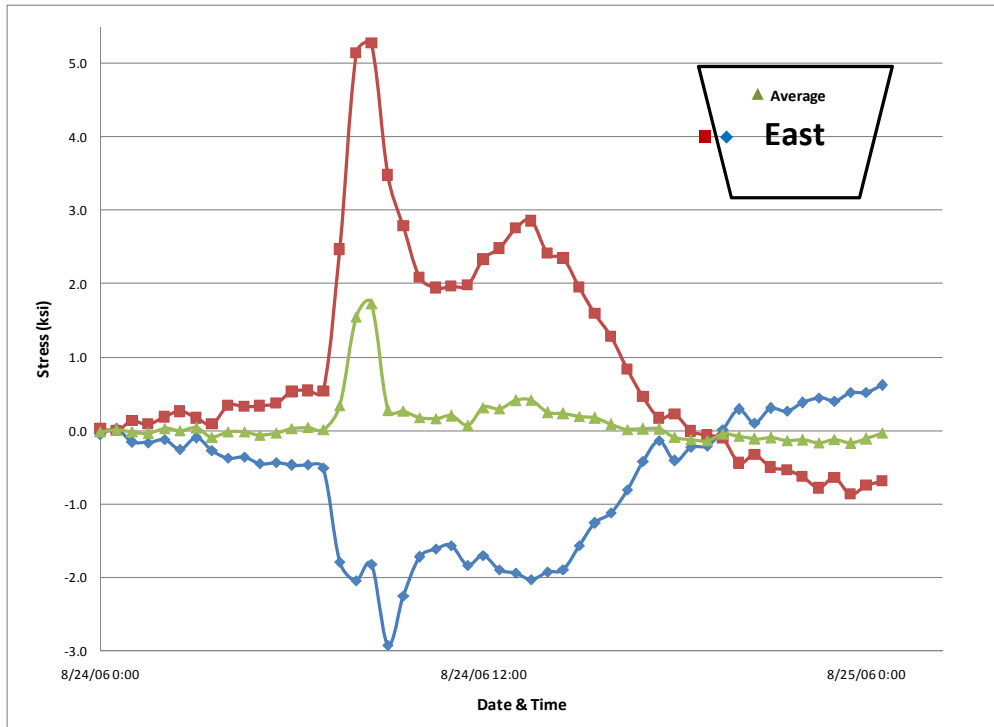


**Figure B-3 Stress Development of West Rail Casting – Bottom of Web**

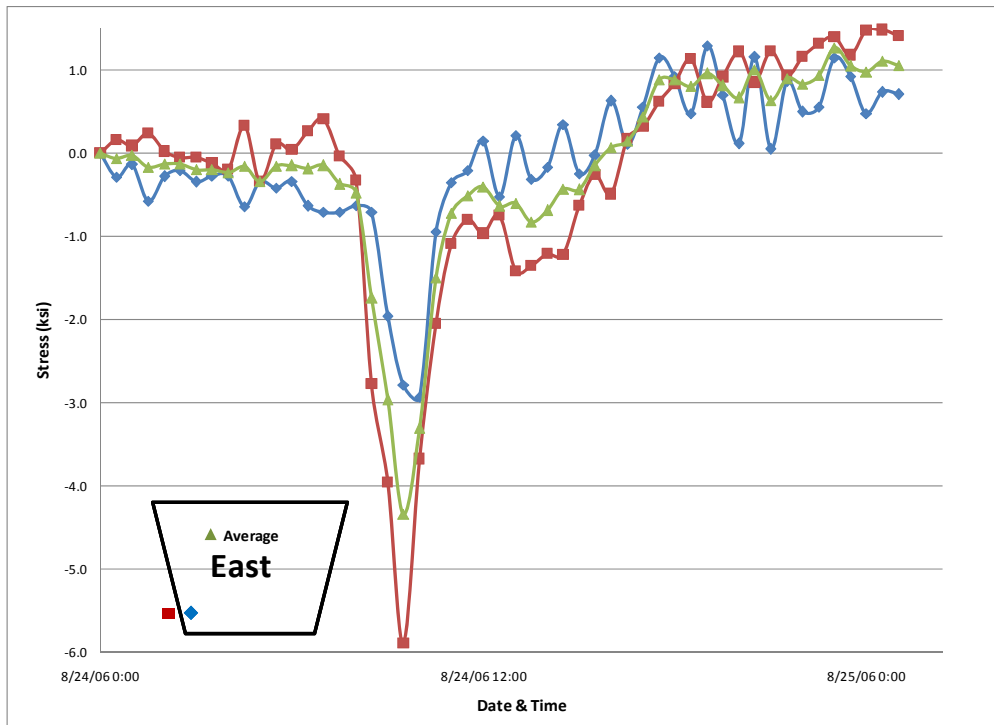


**Figure B-4 Stress Development of East Rail Casting – Top of Web**





**Figure B-5 Stress Development of East Rail Casting – Middle of Web**



**Figure B-6 Stress Development of East Rail Casting - Bottom of Web**

## B.2 Stress versus Time – Live Load Testing

Chapter 4 also presented stress versus time graphs in relation to all live loading positions. The graphs presented in the chapter only depicted results for top flange locations. This section will provide graphs for the remainder of the web sections during all live load positions. The data errors and inconsistencies mentioned in Chapter 4 relate to the data presented in this section as well.

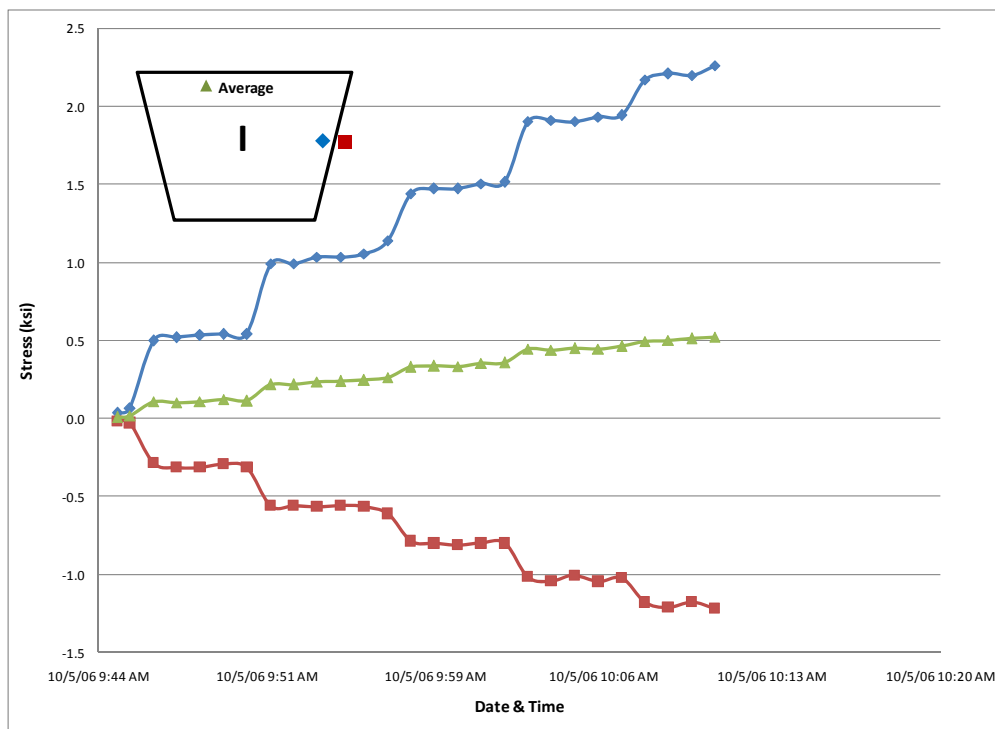
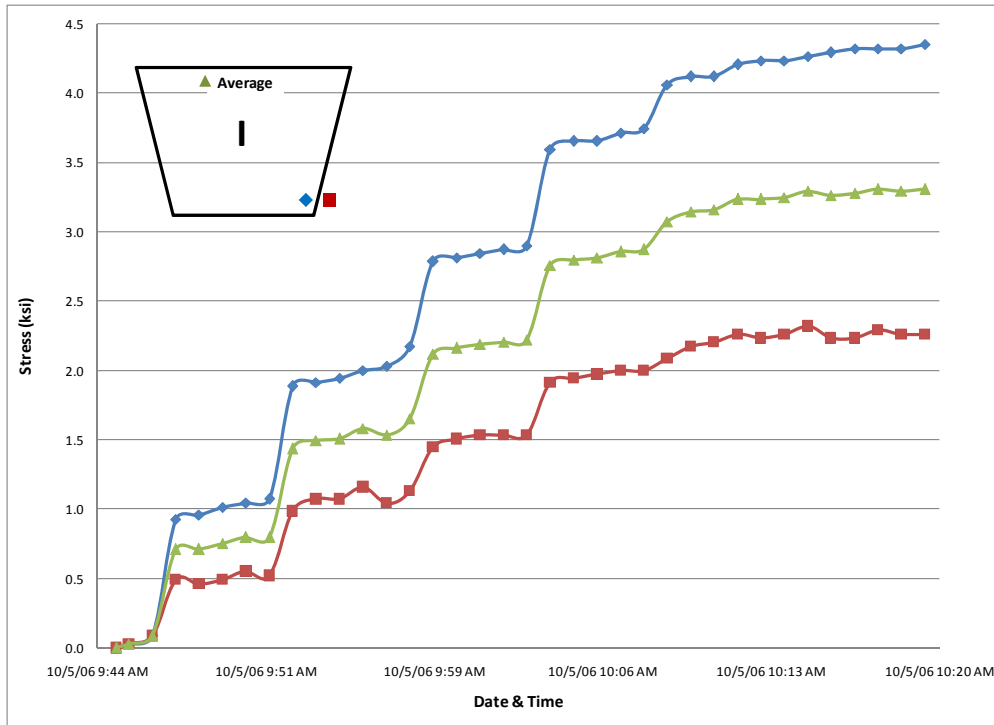
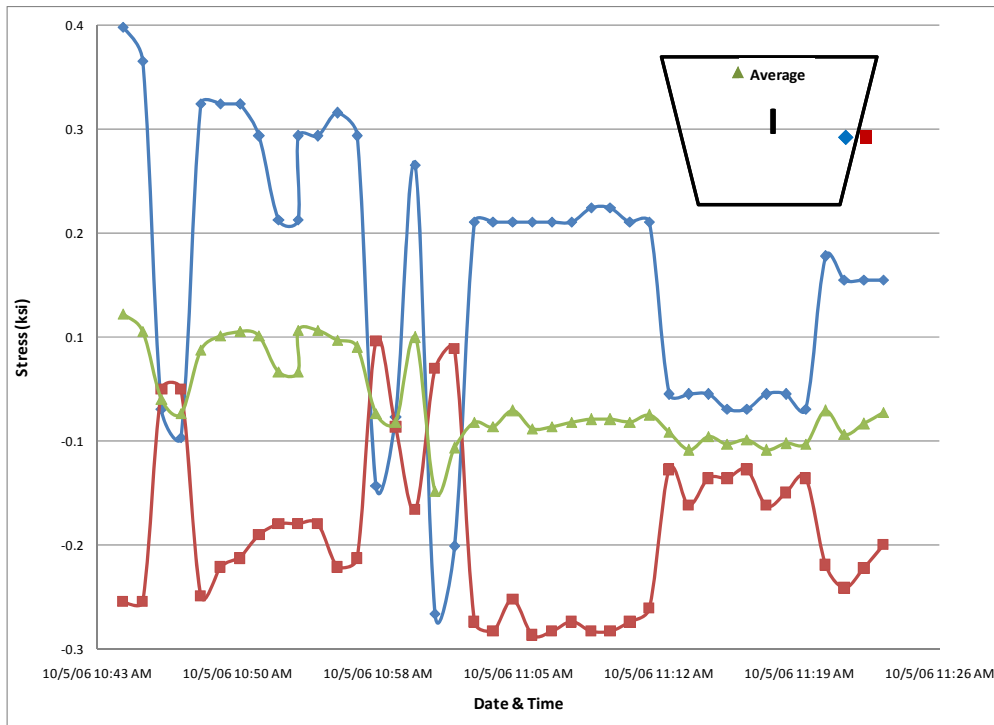


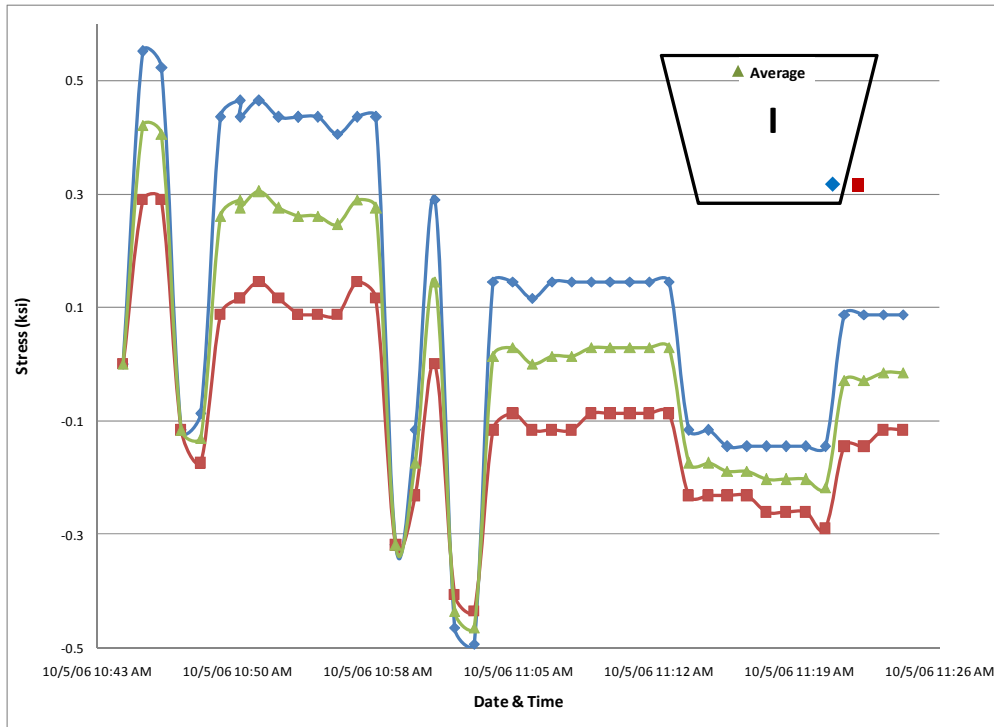
Figure B-7 Stress Development of Live Load Position 1 – Middle of Web



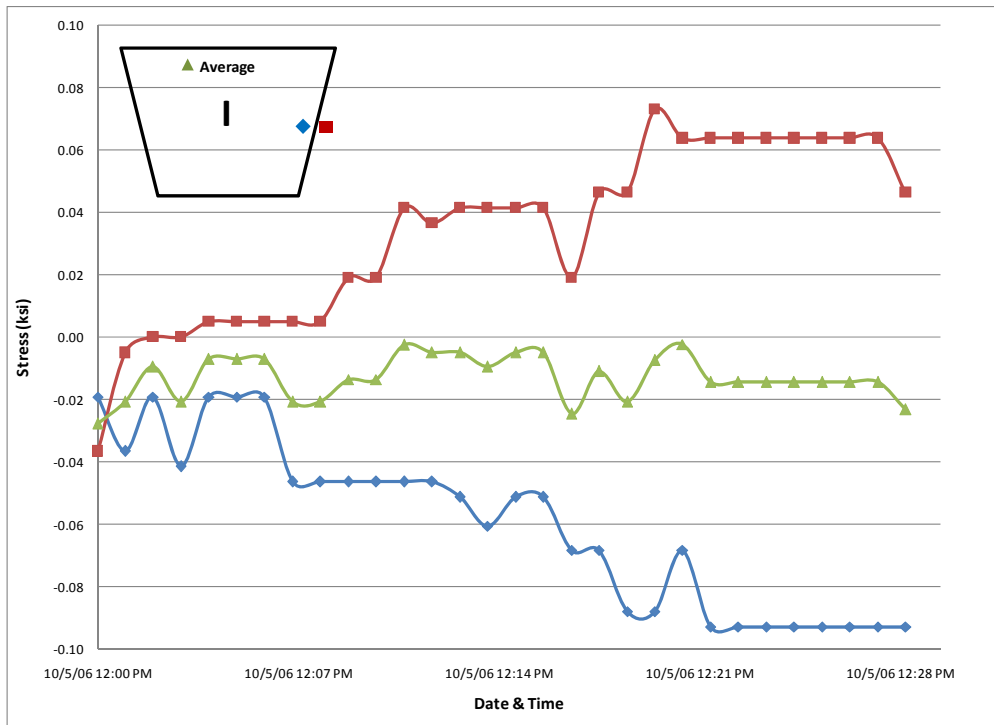
**Figure B-8 Stress Development of Live Load Position 1 – Bottom of Web**



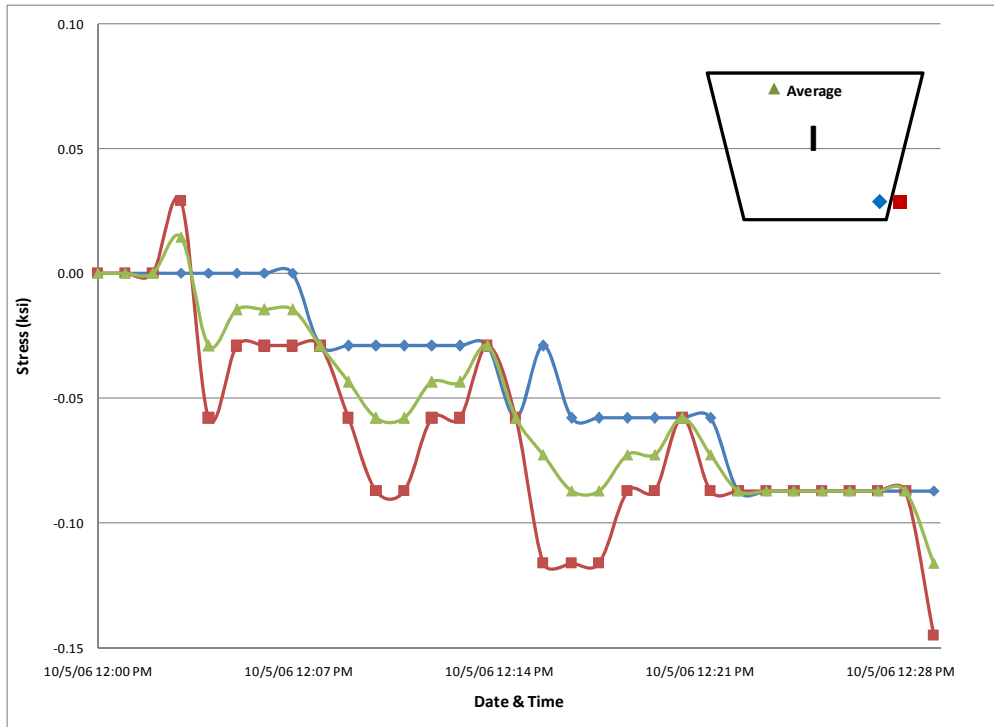
**Figure B-9 Stress Development of Live Load Position 2 – Middle of Web**



**Figure B-10 Stress Development of Live Load Position 2 – Bottom of Web**



**Figure B-11 Stress Development of Live Load Position 3 - Middle of Web**



**Figure B-12 Stress Development of Live Load Position 3 - Bottom of Web**

## APPENDIX C

### Strain Corrections due to Thermal Effects

Chapter 4 presented the subject of correcting the strain readings during the simulated live load testing. Because the testing was completed during the day, the thermal effects on the readings must be observed and accounted for. In addition, the use of the incorrect type of strain reading device must also be accounted for. The following example will explain how to account for both corrections.

#### C.1 Correction Example

The following example depicts the correction method for a single resistive foil strain gage located on the bridge girders during the first position of the simulated live load testing. Table C-1 presents field results that will be corrected. Temperatures for each strain reading were based on a thermocouple that was located near the strain gage being corrected.

**Table C-1 Example Given Data**

	<b>Date &amp; Time</b>	<b>Strain (<math>\epsilon</math>)</b>	<b>Temp. (<math>^{\circ}</math>F)</b>	<b><math>\Delta T</math></b>
Start Loading	10/5/2006 9:45 am	0.000157	96.9018	0
End Loading	10/5/2006 10:20 am	0.000137	99.0913	2.1895
Fully Unloaded	10/5/2006 10:40 am	0.000123	99.163	2.2612

To calculate the correction factor, the coefficient of thermal expansion for both the mild steel and stainless steel strain gages will be needed. The basis of this calculation is to find the difference between the values, and then convert the value to degrees Fahrenheit since the data presented in this thesis is based in degrees Fahrenheit. The last step of this correction will be to apply the correction to the original strain.

$$\text{Stainless Coeff.} - \text{Mild Coeff.} = 11.8 - 16.2 = -4.4 \frac{\text{microstrain}}{^{\circ}\text{C}} \quad (\text{C. 1})$$

$$-4.4 \frac{\text{microstrain}}{^{\circ}\text{C}} = -2.44 \frac{\text{microstrain}}{^{\circ}\text{F}} \quad (\text{C. 2})$$

$$\text{Correction Factor} = -2.44 \frac{\text{microstrain}}{^{\circ}\text{F}} \times \Delta^{\circ}\text{F} \quad (\text{C. 3})$$

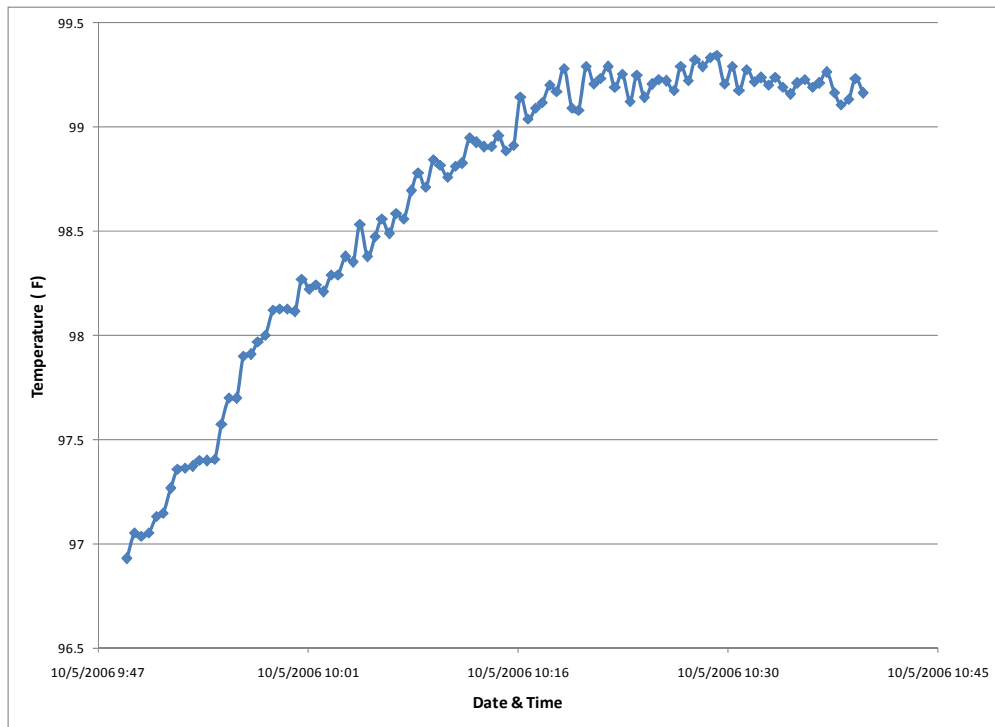
$$\text{Corrected Strain} = \text{Original Strain} + \text{Correction Factor} \quad (\text{C. 4})$$

Table C-2 presents the application of the correction factor to the original strains. Equation (C.3) is used to produce each individual correction factor based on the temperature difference. Equation (C.4) is then used to calculate the corrected strain value.

**Table C-2 Example Calculations**

<b>Original Strain (ε)</b>	<b>Temp. (°F)</b>	<b>ΔT</b>	<b>Correction</b>	<b>Corrected Strain (ε)</b>
0.000157	96.9018	0	0	0.000157
0.000138	99.0913	2.1895	-0.0000053	0.000133
0.000123	99.163	2.2612	-0.0000055	0.000117

Once the strains are corrected for the incorrect type of strain gage, they must now be corrected to account for the temperature change that occurred during the simulated live loading procedure. Figure C-1 presents a graph of temperature versus time during the duration of the first live loading position. As shown on the figure, the temperature curve is non-linear and represents more of a parabolic curve.



**Figure C-1 Temperature versus Time**

Because the temperature curve is non-linear a percentage method was used to calculate the amount of strain present due to thermal changes alone. A ratio of the change in temperature at the end of loading towards the total temperature change is first calculated. The temperature correction is then calculated by using the ratio and specific strains. A final corrected strain and stress are then calculated.



$$\text{Ratio} = \frac{(\text{End Temp.} - \text{Start Temp.})}{(\text{Unload Temp.} - \text{Start Temp.})} = \frac{(99.0913 - 96.9018)}{(99.163 - 96.9018)} = 0.97 \quad (\text{C. 5})$$

$$\text{Temp. Effect} = \text{Ratio} \times (\varepsilon_{\text{unload}} - \varepsilon_{\text{start load}}) = -0.000038 \quad (\text{C. 6})$$

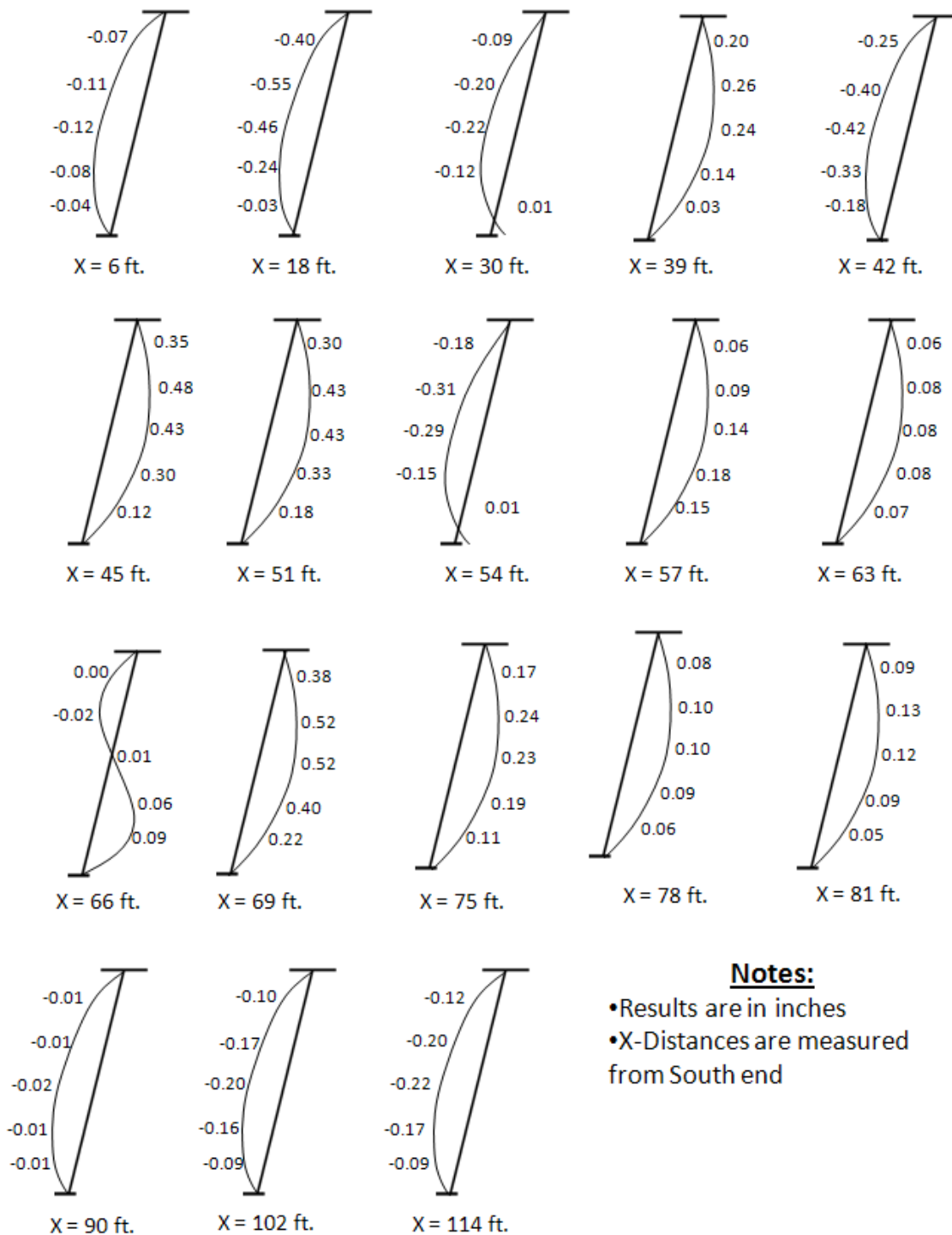
$$\varepsilon_{\text{correct}} = (\varepsilon_{\text{end load}} - \varepsilon_{\text{start load}}) - \text{Temp. Effect} = 0.000014 \quad (\text{C. 7})$$

$$\sigma_{\text{correct}} = \frac{\varepsilon_{\text{correct}} \times 29000 \times 10^3}{1000} = 0.404 \text{ ksi} \quad (\text{C. 8})$$

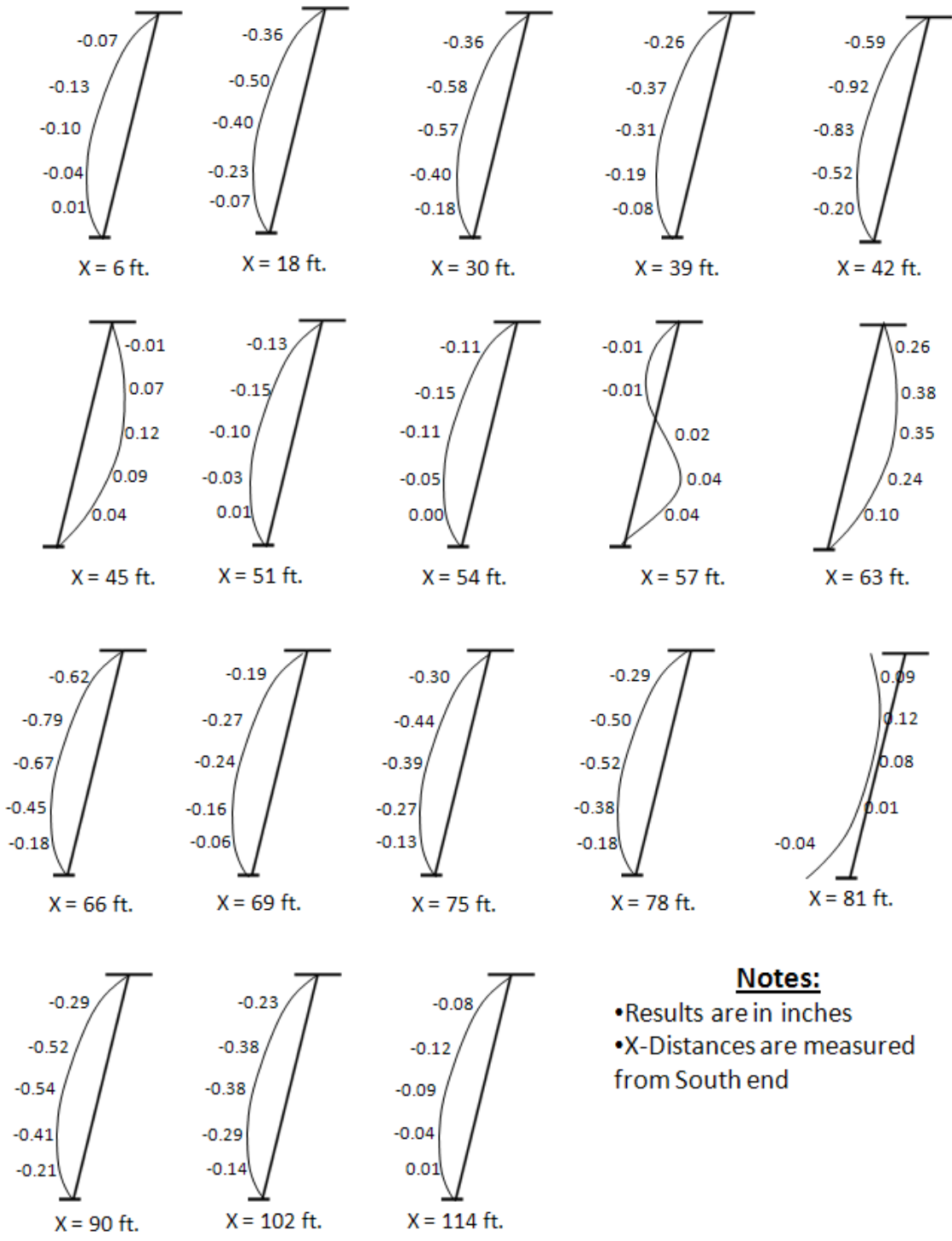
## **APPENDIX D**

### **Plate Deformations**

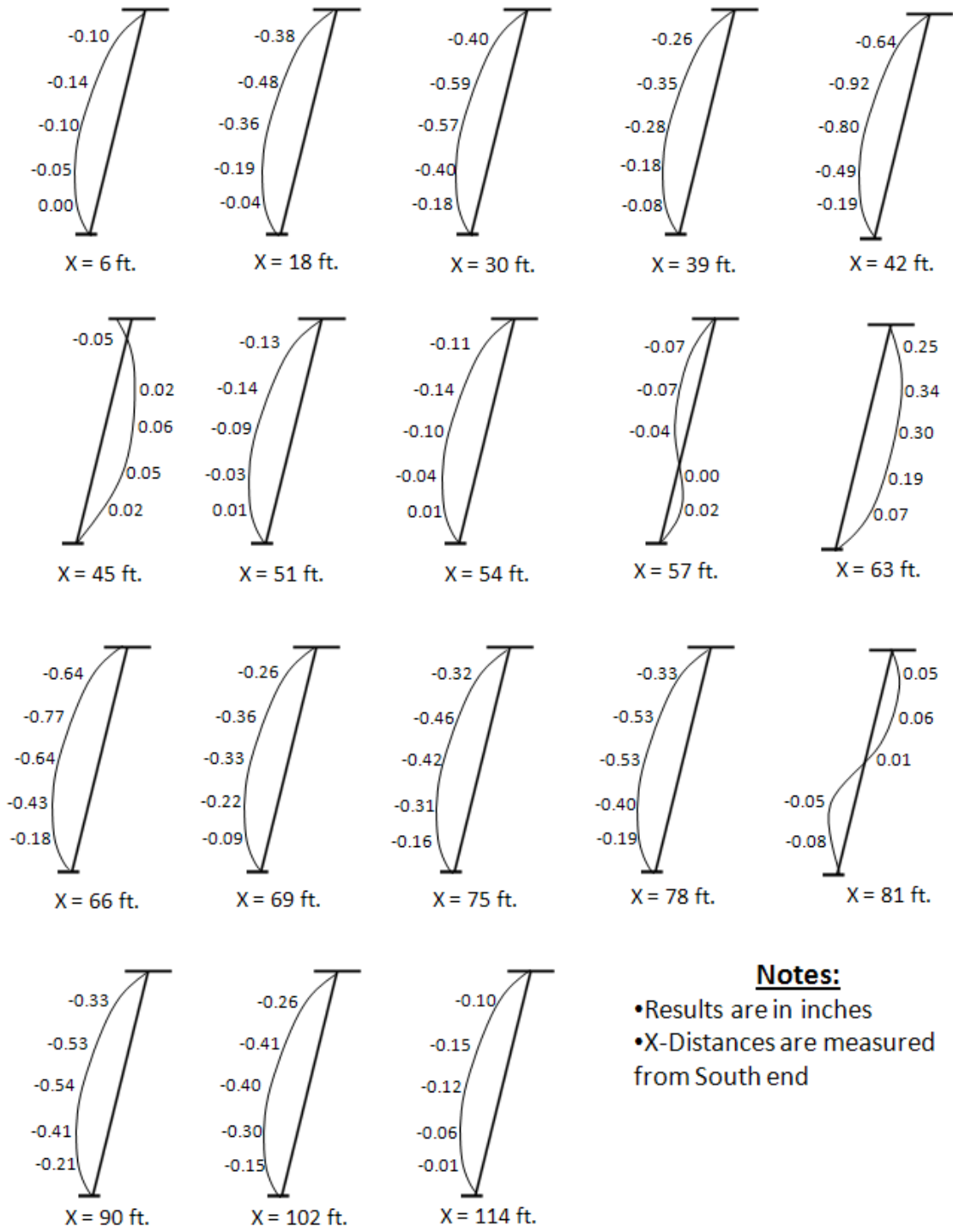
Chapter 5 presented data results for measured plate imperfections. The plate deformations presented were only those located at the main cross-section of the bridge girders that were instrumented with strain and temperature reading devices. This research project is part of a larger overall project sponsored by TxDOT and emphasizes on plate deformations due to various construction phases. Therefore, plate deformations throughout the entire bridge system were measured. Initial imperfections were measured on all webs and bottom flanges before any overhang brackets or formwork for the concrete deck was constructed. Deformations were then measured after the concrete deck had been cast. Finally, the deformations on the outside webs were measured after the form brackets had been removed. All results for all locations on the box girder bridge system are presented in this section.



**Figure D-1 Exterior Girder Outer Web - Initial Imperfections**

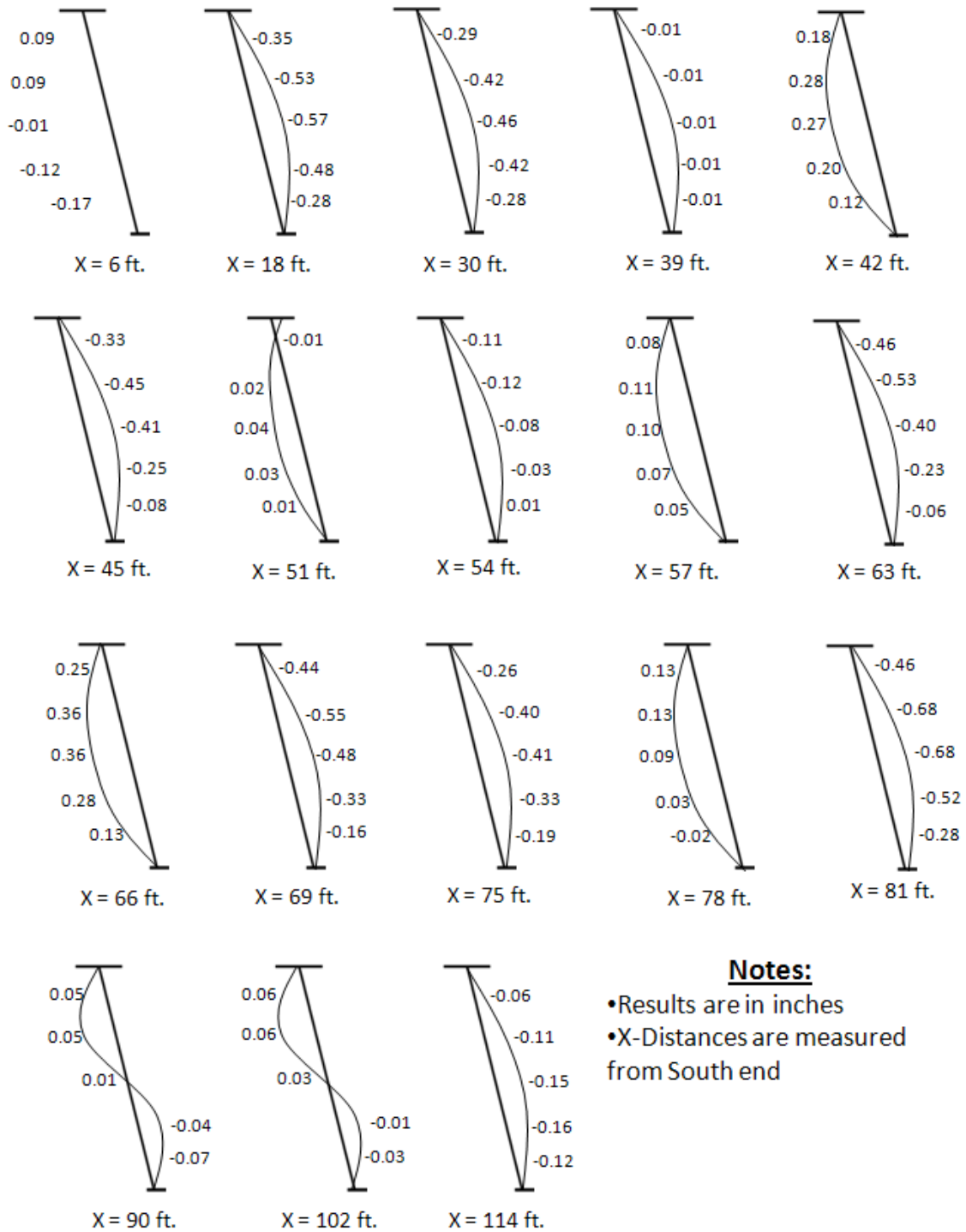


**Figure D-2 Exterior Girder Outer Web - After Casting of Deck**



**Notes:**  
 •Results are in inches  
 •X-Distances are measured from South end

**Figure D-3 Exterior Girder Outer Web - After Bracket Removal**



**Figure D-4 Exterior Girder Inner Web - Initial Imperfections**

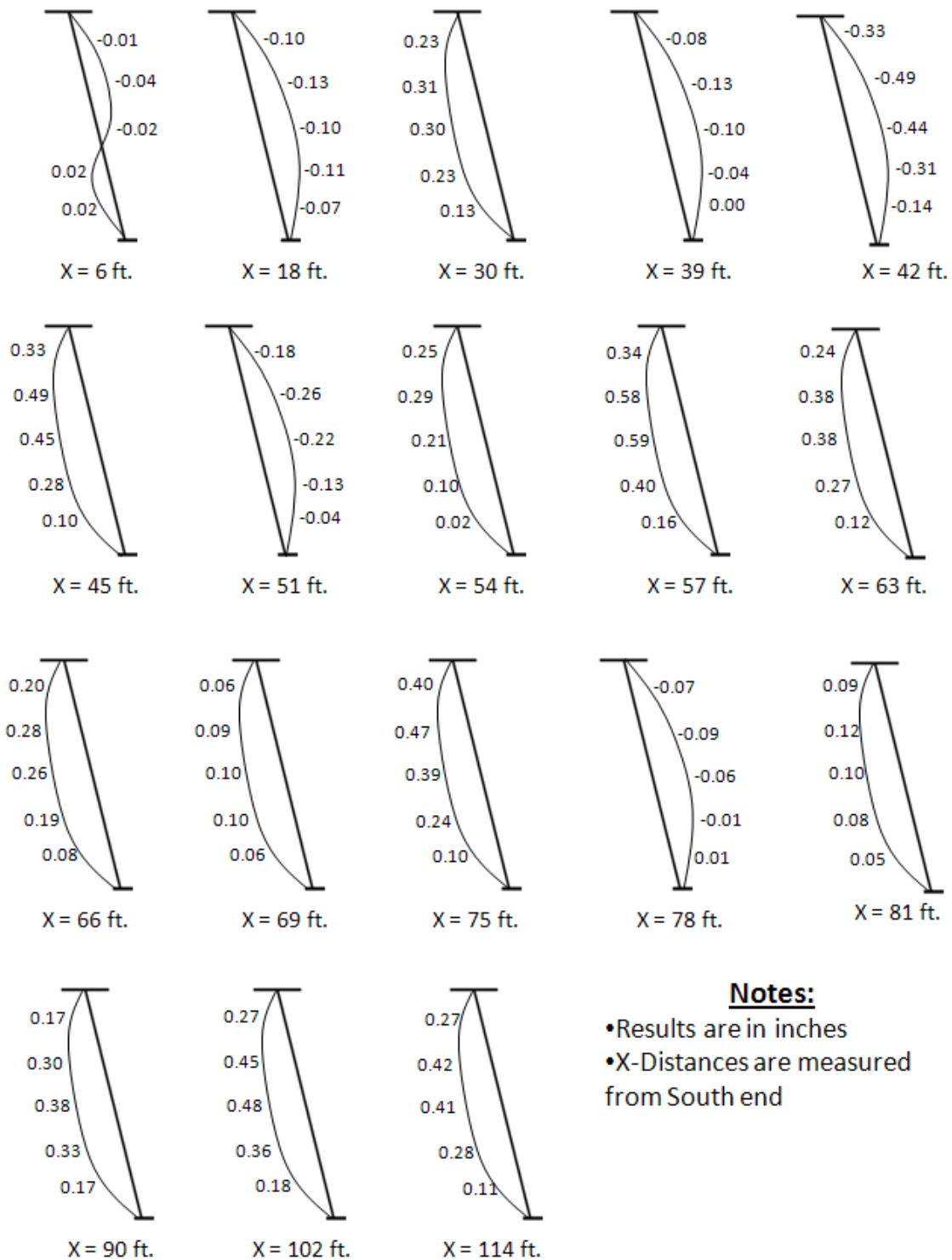
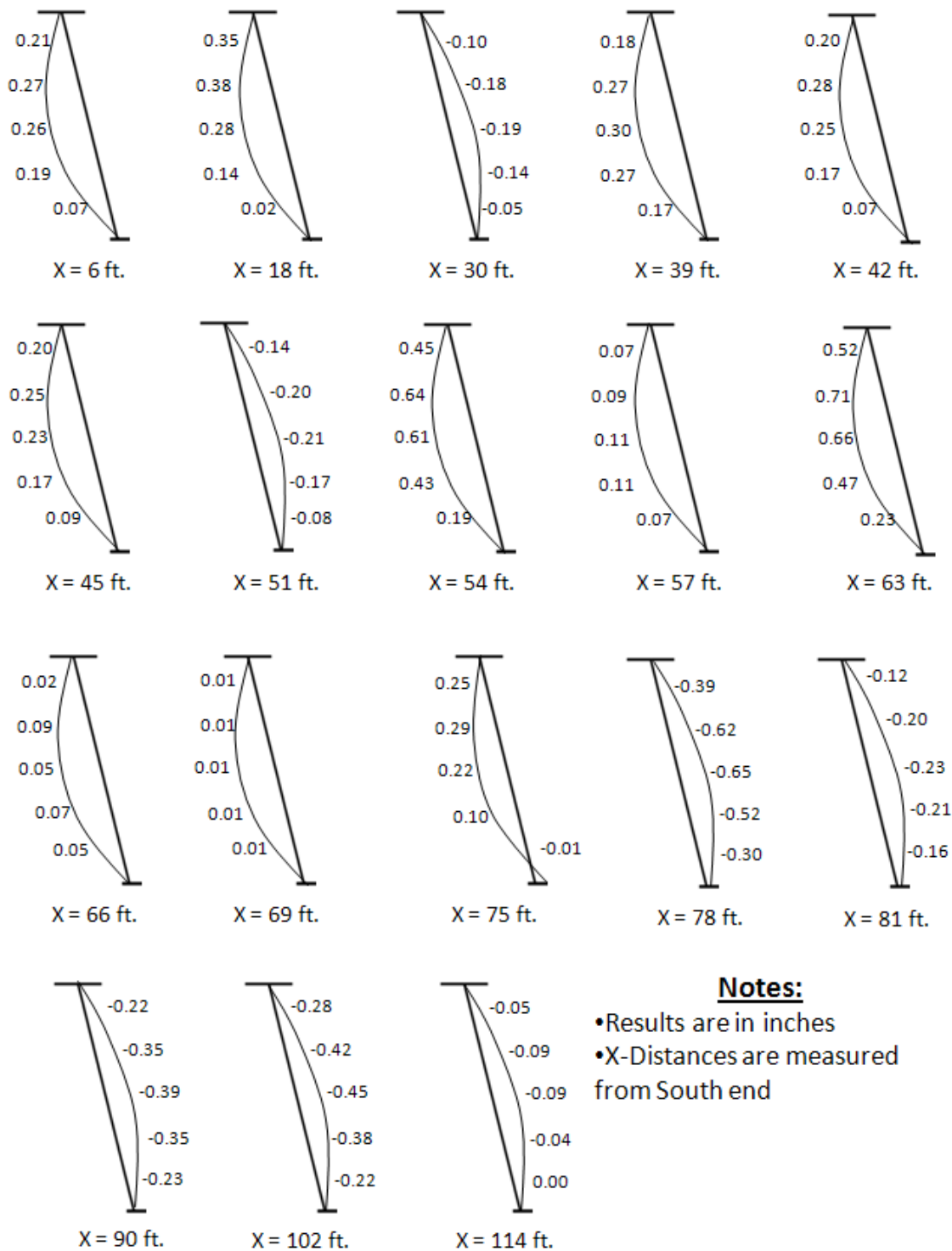
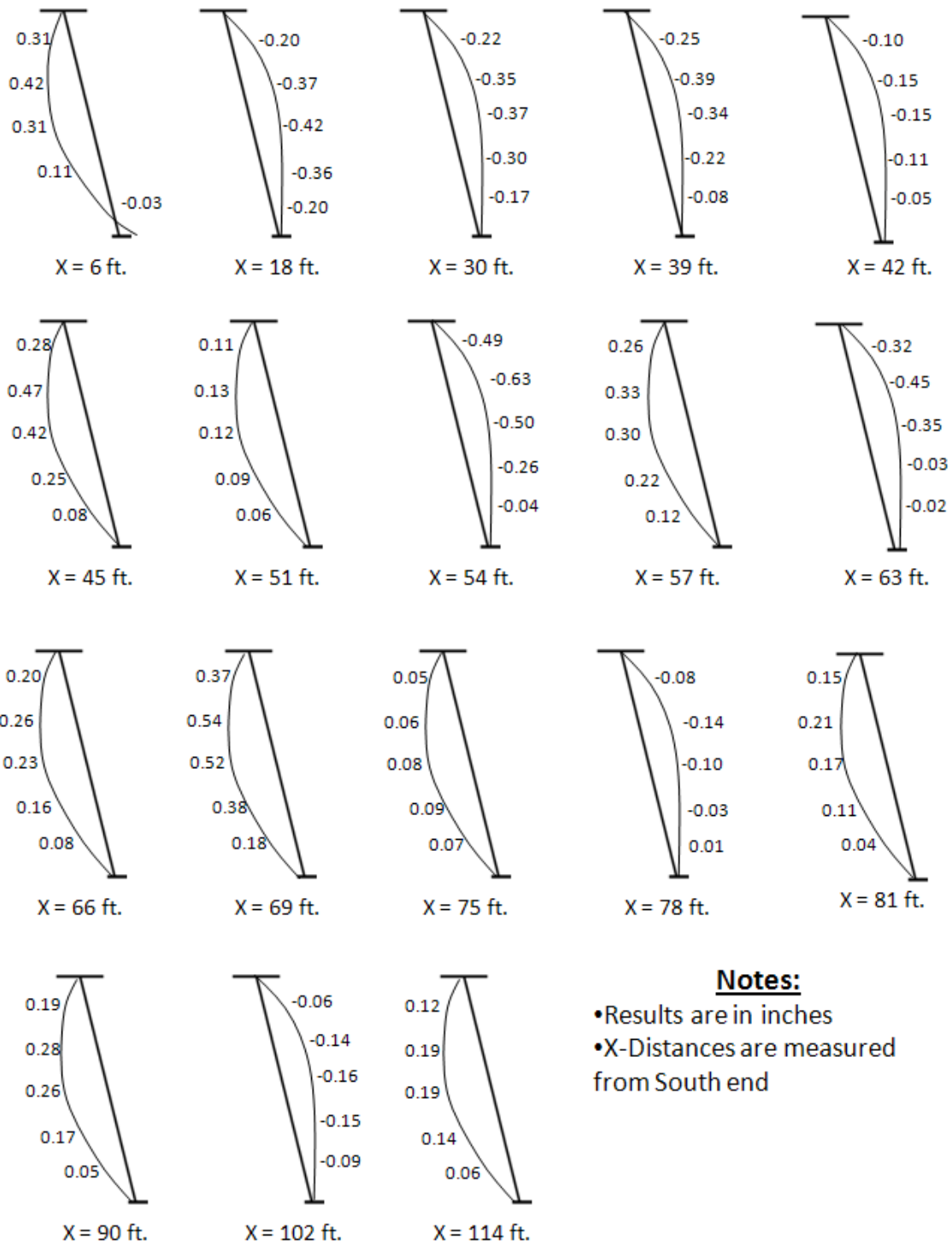


Figure D-5 Exterior Girder Inner Web - After Casting of Deck

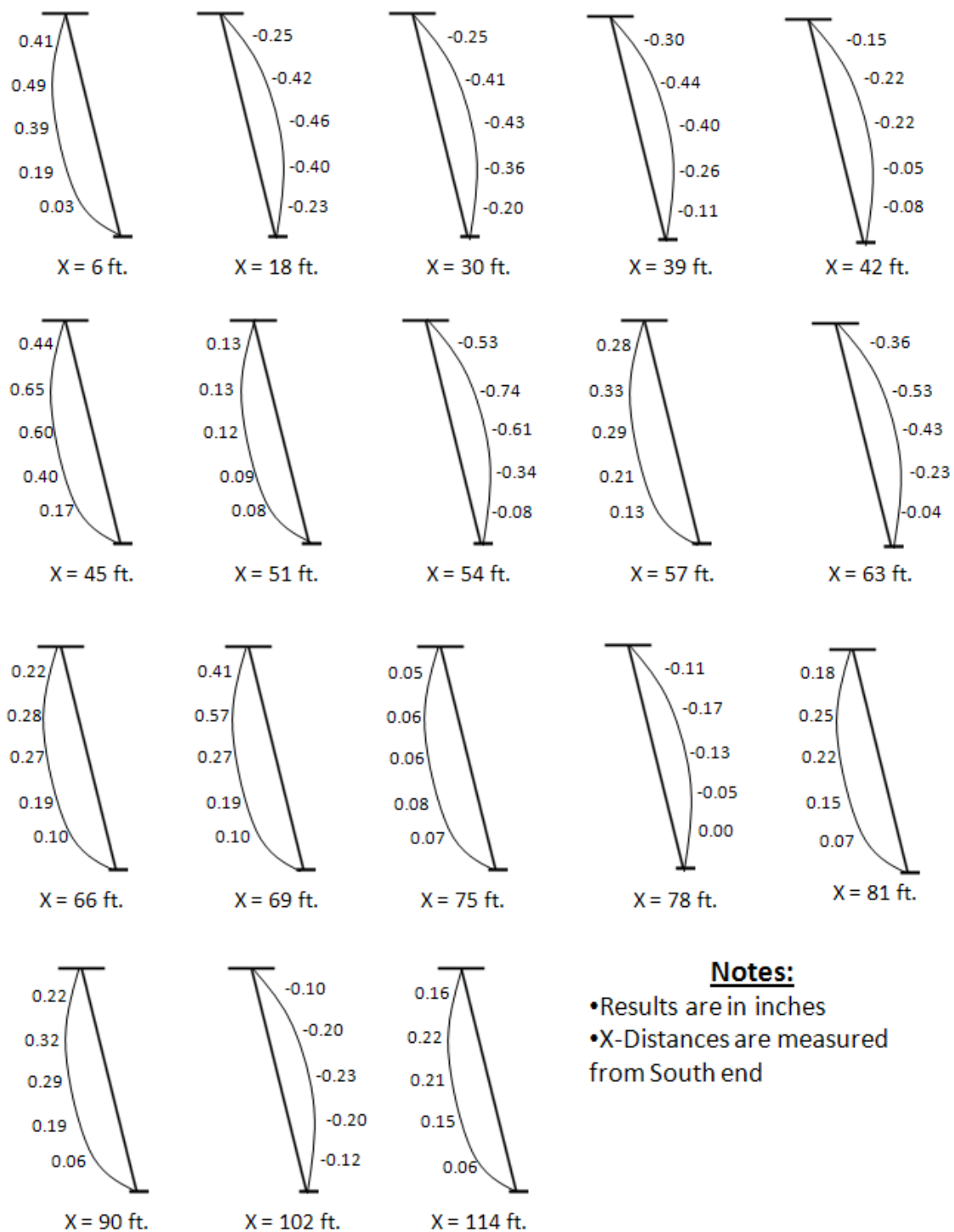


**Figure D-6 Interior Girder Outer Web - Initial Imperfections**

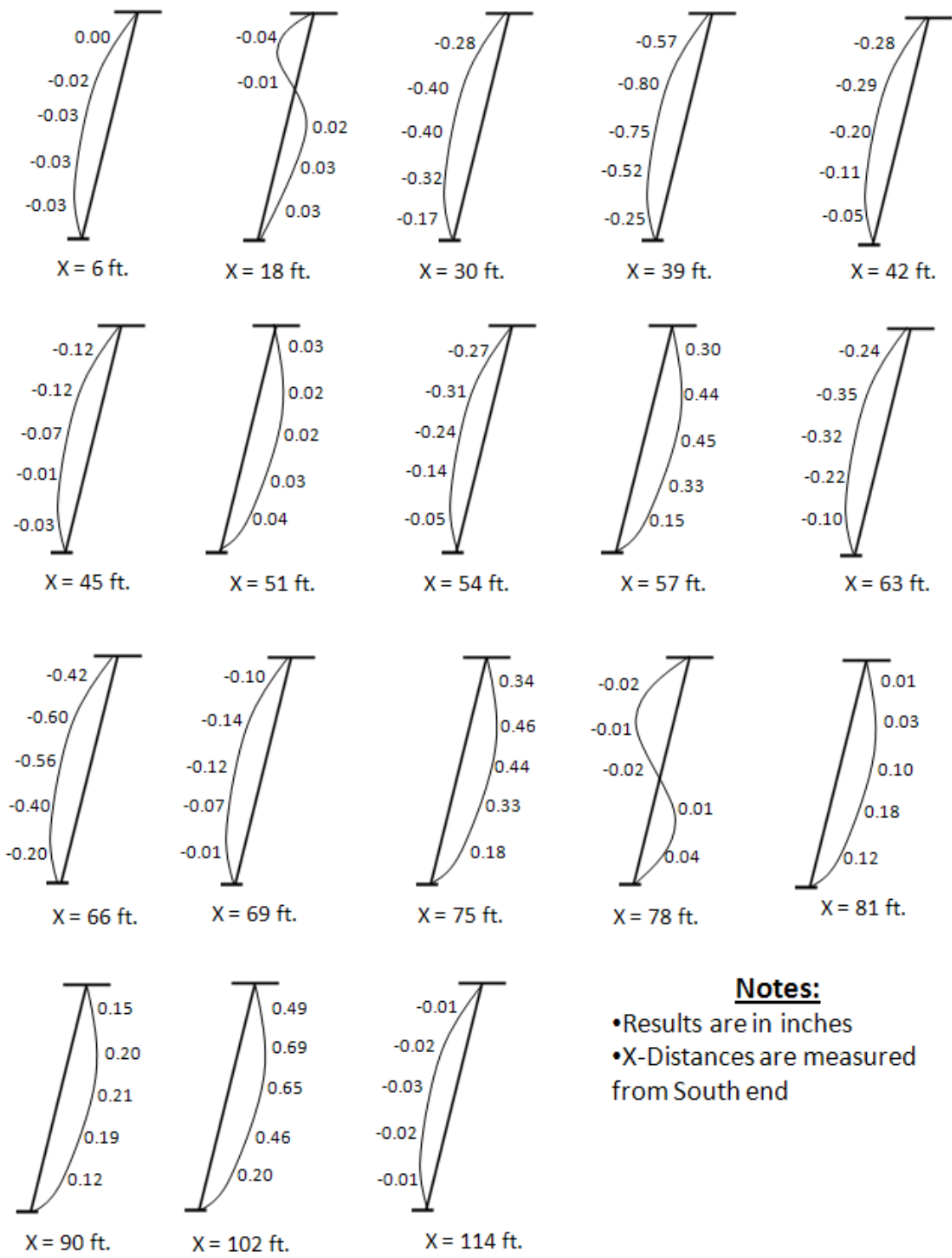




**Figure D-7 Interior Girder Outer Web - After Casting of Deck**

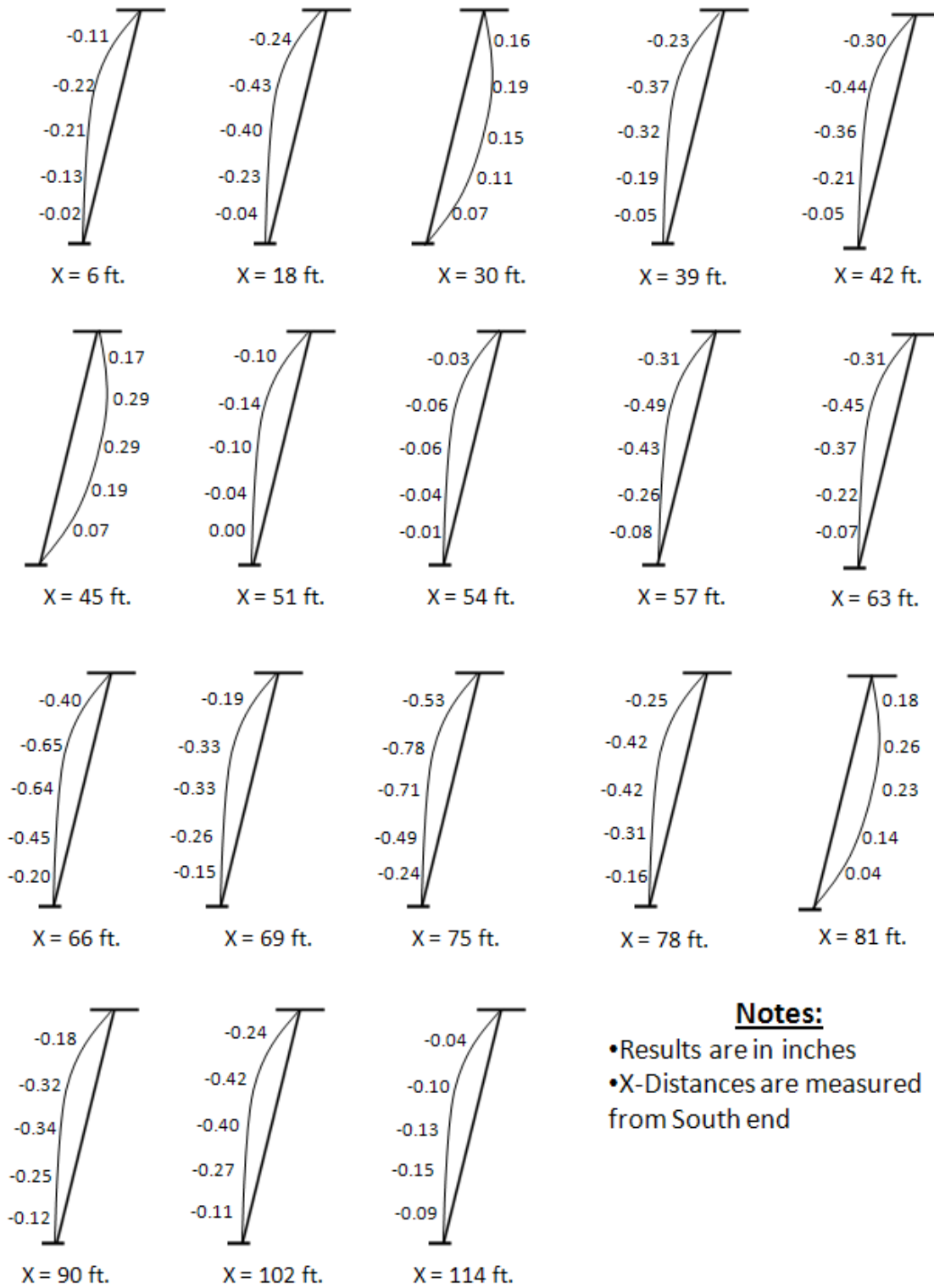


**Figure D-8 Interior Girder Outer Web - After Bracket Removal**

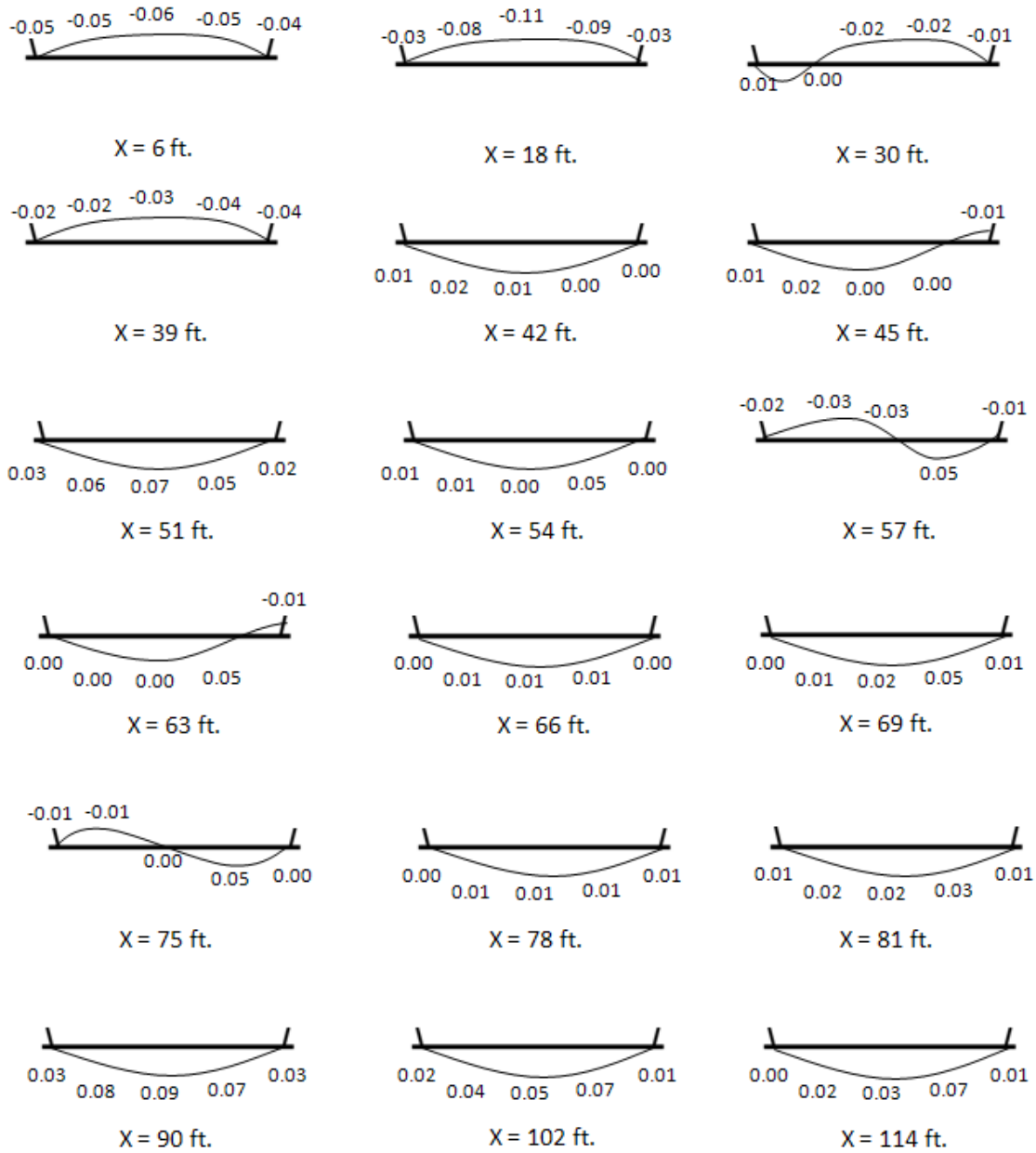


- Notes:**
- Results are in inches
  - X-Distances are measured from South end

**Figure D-9 Interior Girder Inner Web - Initial Imperfections**



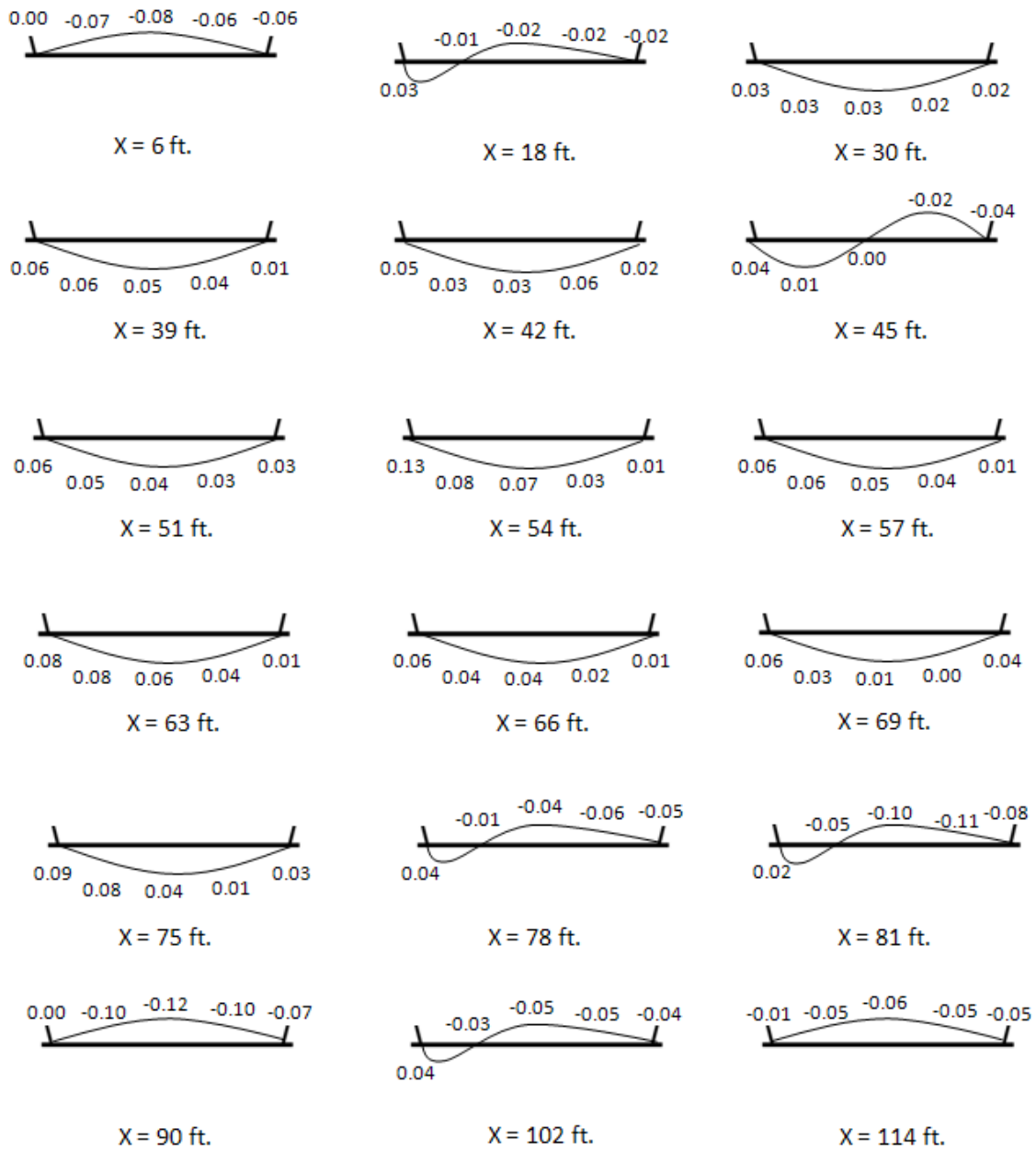
**Figure D-10 Interior Girder Inner Web - After Casting of Deck**



**Notes:**

- Results are in inches
- X-Distances are measured from South end

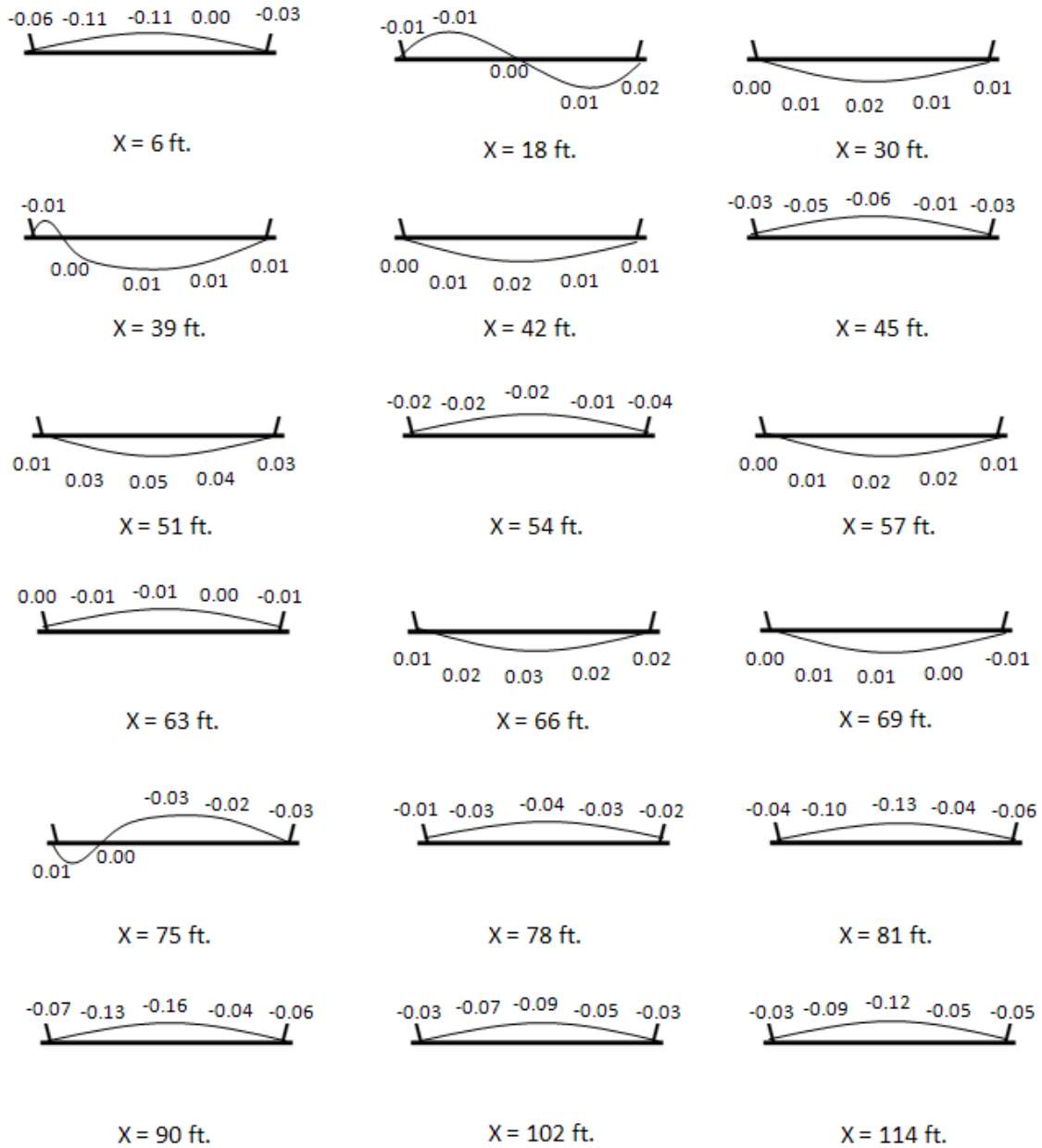
**Figure D-11 Interior Girder Bottom Flange - Initial Imperfections**



**Notes:**

- Results are in inches
- X-Distances are measured from South end

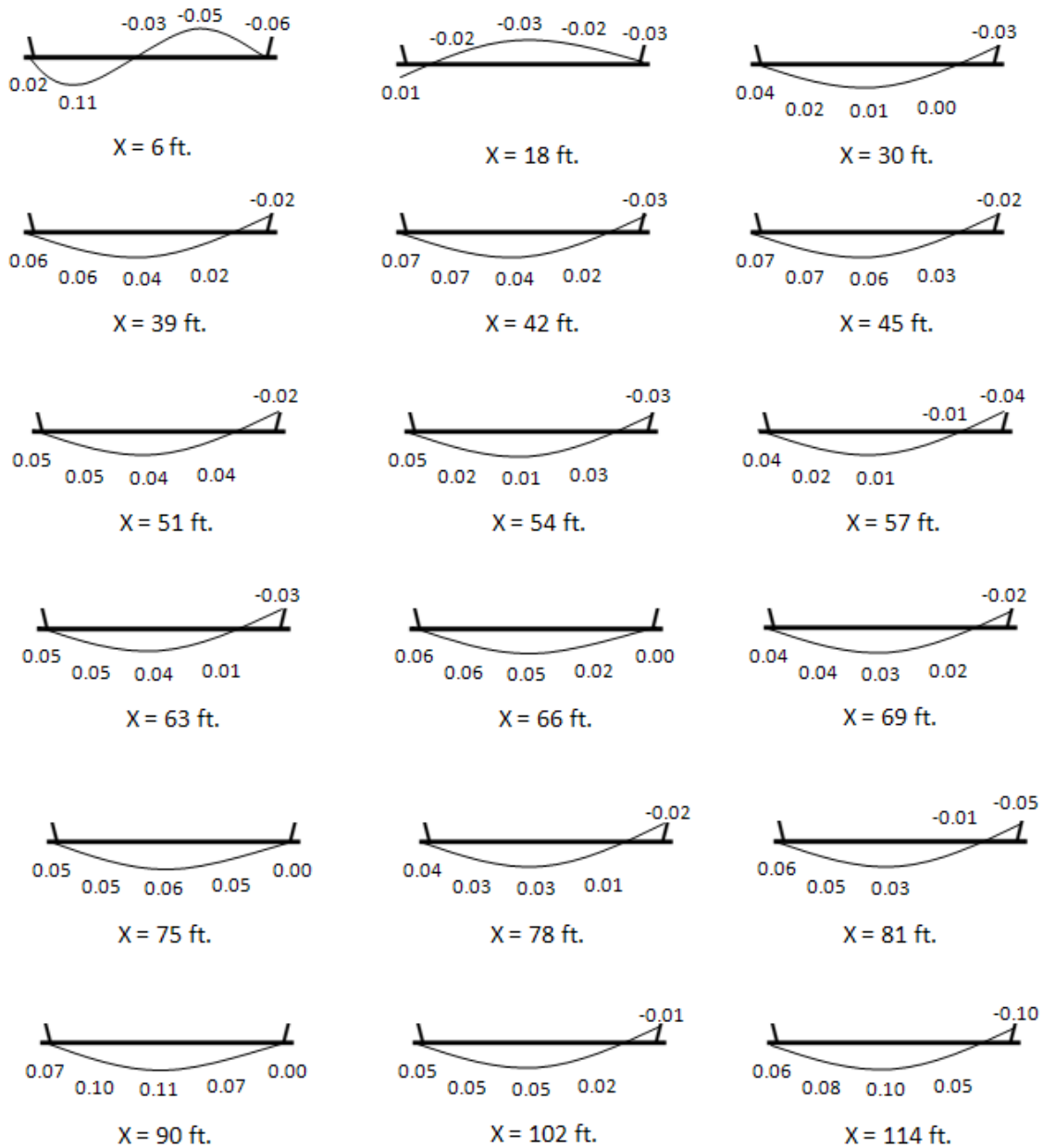
**Figure D-12 Interior Girder Bottom Flange - After Casting of Deck**



**Notes:**

- Results are in inches
- Distances are measured from South end

**Figure D-13 Exterior Girder Bottom Flange - Initial Imperfections**



**Notes:**

- Results are in inches
- Distances are measured from South end

**Figure D-14 Exterior Girder Bottom Flange - After Casting of Deck**



## References

- AASHTO Guide Specifications for Horizontally Curved Steel Girder Highway Bridges.* (2003). Washington, DC: American Association of State Highway and Transportation Officials.
- AASHTO Standard Specifications for Highway Bridges* (17th ed.). (2002). Washington, DC: American Association of State Highway and Transportation Officials.
- AASHTO/AWS D1.5M/D1.5 Bridge Welding Code.* (2002). Miami, FL: American Welding Society.
- Allen, H. (1980). *Background to Buckling.* Great Britain: McGraw-Hill Book Company (UK) Limited.
- American Institute of Steel Construction, Inc. (2001). *Manual of Steel Construction: Load and Resistance Factor Design* (3rd ed.). AISC.
- Arakan, Y. (2005). *Field Monitoring of Thermal Effects in Steel Box Girder Bridges.* Thesis, University of Houston.
- ASTM A6/A 6M-06 Standard Specification for General Requirements for Rolled Structural Steel Bars, Plates, Shapes, and Sheet Piling.* (2006). American Society for Testing and Materials.
- BS5400 Part 6: Steel, Concrete and Composite Bridges - Specification for Materials and Workmanship, Steel.* (1970). London: British Standards Institution.
- Campbell Scientific Inc. (2006). *Vibrating Wire Interface Model AVW100.* Retrieved May 1, 2006, from [http://www.campbellsci.com/documents/lit/b\\_avw100.pdf](http://www.campbellsci.com/documents/lit/b_avw100.pdf)
- Campbell Scientific, Inc. (2001). *CR5000 Measurement and Control System Operator's Manual, Revision 8/01.* Logan, UT.
- Campbell Scientific, Inc. (1996). *Instruction Manual, 4WFB120, 4WFB350, 4WFB1k 4 Wire Full Bridge Terminal Input Modules.* Logan, UT.
- Campbell Scientific, Inc. (1996). *Instruction Manual, AM416 Relay Multiplexer, Revision 2/96.* Retrieved May 1, 2006, from <http://www.campbellsci.com/documents/manuals/am416.pdf>

Campbell Scientific, Inc. (1992). *Instruction Manual, Use of the AVW1 and AVW4 with Geokon Model 4500 Vibrating Wire Piezometers and Pressure Transducers, Revision 1/92*. Logan, UT.

De Miranda, F., & Mele, M. (1973). Some Basic Design Principles for Steel Box Girder Bridges. In P. Cartledge (Ed.), *Proceedings of the International Conference Organized by the Institution of Civil Engineers in London, Steel Box Girder Bridges* (pp. 21-31). Great Britain: Thomas Telford Limited.

*Eurocode 3 Design of Steel Structures, Part 1.5 Plated Structural Elements, Final Draft*. (2003). European Committee for Standardization.

Galambos, T. (1988). *Guide to Stability Design Criteria for Metal Structures*. New York: John Wiley & Sons, Inc.

Geokon, Inc. (2005). *Instruction Manual, Model 4000 Vibrating Wire Strain Gage, Revision 6/05*. Lebanon, NH.

Grzebieta, R. (2007). Retrieved April 11, 2007, from <http://www.law.monash.edu.au/iifs/raph-grzebieta.pdf>

Hall, D. H. (1997). Why Steel Box Girders? *Modern Steel Construction* , 37 (4), pp. 13-16.

Helwig, T., & Fan, Z. (2000). *Field and Computational Studies of Steel Trapezoidal Box Girder Bridges*. TxDOT Research Report 1395-3, University of Houston.

Herman, R. (2001). *Behavior of Stiffened Compression Flanges of Trapezoidal Box Girder Bridges*. PhD dissertation, University of Texas, Austin.

ISE, Inc. (2007). *ITS-90 Table for Type T Thermocouple*. Retrieved February 1, 2007, from <http://instrumentation-central.com/TechNotes/TypeTTableC.pdf>

Kerensky, O. (1973). Conception. In P. Cartledge (Ed.), *Proceedings of the International Conference Organized by the Institution of Civil Engineers in London, Steel Box Girder Bridges* (pp. 7-10). Great Britain: Thomas Telford Limited.

Korol, R. M., & Thimmhardy, E. G. (1987). An Experimental Investigation of the Effects of Imperfections on the Strength of Steel Box Girders. *Canadian Journal of Civil Engineers* , 15 (3), pp. 443-449.

- Korol, R. M., & Thimmhardy, E. G. (1984). Field Investigations of Out-of-Plane Deviations from Steel Box Girder Bridges. *Canadian Journal of Civil Engineering*, 11 (3), pp. 377-386.
- Korol, R. M., & Thimmhardy, E. G. (1987). Geometric Imperfections and Tolerances for Steel Box Girder Bridges. *Canadian Journal of Civil Engineering*, 15 (3), pp. 437-442.
- Leonhardt, F., & Hommel, D. (1973). The Necessity of Quantifying Imperfections of all Structural Members for Stability of Box Girders. In P. Cartledge (Ed.), *Proceedings of the International Conference Organized by the Institution of Civil Engineers in London, Steel Box Girder Bridges* (pp. 11-19). Great Britain: Thomas Telford Limited.
- Maquoi, R. (1995). Ultimate States of Plate and Box Girders. In M. Ivanyi, & M. Skaloud (Ed.), *CISM Courses and Lectures No. 358: Steel Plates Structures* (pp. 247-320). New York: Wein.
- Mercan, B. (2005). *Field Measurements of Plate Imperfections in Steel Box Girders*. Thesis, University of Houston.
- Microsoft. (2007). *Microsoft Windows Live Search*. Retrieved January 2007, from <http://maps.live.com>
- National Instruments. (2007). *Measuring Strain with Strain Gages*. Retrieved January 31, 2007, from <http://zone.ni.com/devzone/cda/tut/p/id/3642>
- Omega Engineering. (2007). *The Strain Gage*. Retrieved January 31, 2007, from <http://www.omega.com/literature/transactions/volume3/strain.html>
- Pico Technology. (2007). *Thermocouple Application Note*. Retrieved February 1, 2007, from <http://www.picotech.com/applications/thermocouple.html>
- Segui, W. T. (2003). *LRFD Steel Design* (3rd ed.). Pacific Grove, California: Brooks-Cole.
- Specifications for Highway Bridges, Part II Steel Bridges*. (1973). Japan Road Association.
- Timoshenko, S. (1961). *Theory of Elastic Stability* (2nd ed.). New York: McGraw-Hill Book Company.
- Vishay Micro-Measurements. (2005). *Strain Gage Rosettes*. Retrieved January 31, 2007, from [http://www.vishay.com/docs/11065/\\_ymr-tc0.pdf](http://www.vishay.com/docs/11065/_ymr-tc0.pdf)

Watlow Electric Manufacturing. (2007). *Thermocouple Types*. Retrieved February 1, 2007, from <http://www.watlow.com/reference/refdata/0310.cfm>

Watlow Electric Manufacturing. (2007). *Thermocouple Types*. Retrieved February 1, 2007, from <http://www.watlow.com/reference/refdata/0310.cfm>

Wikipedia. (2007). *Strain Gauge*. Retrieved January 31, 2007, from [http://en.wikipedia.org/wiki/Strain\\_gage](http://en.wikipedia.org/wiki/Strain_gage)

## **Vita**

Omar Rene Espinoza was born in Corpus Christi, Texas on April 20, 1983, to Hector and Estella G. Espinoza. He graduated from Mary Carroll High School, Corpus Christi, Texas, in 2001, and entered Florida State University in Tallahassee, Florida in the fall of the same year. He graduated with the degree of Bachelor of Science from Florida State University in May 2005. In August 2005, he entered The Graduate School at The University of Texas at Austin.

Permanent address: 11160 Jollyville Road # 808  
Austin, Texas 78759

This thesis was typed by the author.